

**MANUFACTURING OF POROUS SURFACES WITH MICRO-SCALE  
FEATURES FOR ADVANCED HEAT TRANSFER**

by

**Peng Chen**

A dissertation submitted in partial fulfillment  
of the requirements for the degree of  
Doctor of Philosophy  
(Mechanical Engineering)  
in The University of Michigan  
2008

Doctoral Committee:

Professor Jun Ni, Chair  
Professor Elijah Kannatey-Asibu Jr.  
Professor John Halloran  
Assistant Professor Gap-Yong Kim

© Peng Chen  
All rights reserved  
2008

..... to the memory of my dear uncle Mr. Ximing Tang who gave me the first and best lessons of scientific thinking and introduced me to the world of engineering when I was young. His encouragement until the last moment of his life, and his memories ever since, have been the best source of motivation for completion of this work. To the memory of a great teacher and man whose thoughts were always ahead of his time.....

## **ACKNOWLEDGEMENTS**

It is Professor Jun Ni whom I wish to thank for his guidance and financial support through the course of my graduate studies. Particularly, I appreciate the faith he put in me and my knowledge that made me work enthusiastically hard, if not only, to prove that he did not believe in me in vain. It was through intellectual interactions with him that, now I realize how much, I grew up as an engineer, researcher and a person.

Especially, I would like to express my appreciation to Professor Gap-Yong Kim for standing by me in all my attempts in completing my graduate studies and being my perfect role model.

I would like to thank my mother Mrs. Youwen Tang and my father Mr. Jinfa Chen for their undivided love. Without their encouragement I could not have succeeded. I am grateful to my uncle Mr. Shuyu Tang and my aunt Mrs. Hong Zhang for their support. My sincere thanks to my sister Xueling Chen and her husband for not only being supportive family members but being my best friends with whom I always enjoyed spending time and sharing my experiences.

I would like to thank my dissertation committee members for their useful comments and guidance. My special thanks to Steven Emanuel for his technical support.

Last but not least, I would like to thank my dearest Wei Zhao for her love, understanding and encouragement.

## TABLE OF CONTENTS

<b>DEDICATION.....</b>	<b>ii</b>
<b>ACKNOWLEDGEMENTS .....</b>	<b>iii</b>
<b>LIST OF FIGURES .....</b>	<b>vii</b>
<b>LIST OF TABLES .....</b>	<b>xi</b>
<b>CHAPTER 1 .....</b>	<b>1</b>
<b>INTRODUCTION.....</b>	<b>1</b>
1.1 Motivation.....	1
1.2 Research Framework and Objectives.....	8
1.2.1 Forming of Porous Micro-features using Cold Compaction and Incomplete Sintering Method .....	8
1.2.2 Forming of Porous Micro-features and Particle/Substrate Bonding using Hot Compaction.....	9
1.2.3 Discrete Element Modeling of the Pressure Assisted Sintering Process .....	10
1.3 Dissertation Organization .....	11
<b>CHAPTER 2.....</b>	<b>12</b>
<b>FORMING OF POROUS MICRO-FEATURES USING COLD COMPACTION AND INCOMPLETE SINTERING METHOD.....</b>	<b>12</b>
2.1 Introduction.....	12
2.2 Literature Review.....	13
2.2.1 Deformation Behavior of Powders in Cold Compaction.....	14
2.2.2 Sintering Process.....	17
2.2.3 Computational Modeling of Cold Powder Compaction .....	19
2.3 Experimental Investigation .....	30
2.3.1 Experimental Set-up and Procedures.....	31
2.3.2 Experimental Results and Discussion.....	36
2.4 Cold Compaction Simulation.....	45
2.4.1 Material Modeling for Compaction Simulation.....	46

2.4.2 FEA Validation: a Case Study on Compaction of Zirconia Powder .....	48
2.4.3 FEA Modeling: Compaction of Copper Powder into Micro-features .....	52
2.5 Conclusions.....	55
<b>CHAPTER 3.....</b>	<b>57</b>
<b>FORMING OF POROUS MICRO-FEATURES AND PARTICLES/SUBSTRATE BONDING USING HOT COMPACTION.....</b>	<b>57</b>
3.1 Introduction.....	57
3.2 Literature Review.....	58
3.2.1 Uni-axial/uni-directional hot pressing (hot die compaction).....	60
3.2.2 Powder forging (P/F, P/M forging, P/M hot forming).....	61
3.3 Forming of Porous Micro-features Using Hot Compaction .....	62
3.3.1 Experimental Setup and Procedures .....	63
3.3.2 Experimental Results and Discussions .....	69
3.4 Thermal Analysis of the Hot Compaction System .....	78
3.4.1 Finite Element Modeling of the Heat Transfer Process.....	79
3.4.2 Results and Discussions.....	81
3.5 Particle/substrate bonding produced by hot compaction .....	84
3.5.1 Experimental Setup and Procedures .....	84
3.5.2 Experimental Results and Discussions .....	86
3.6 Conclusions.....	90
<b>CHAPTER 4.....</b>	<b>93</b>
<b>DISCRETE ELEMENT MODELING OF THE PRESSURE ASSISTED SINTERING PROCESS.....</b>	<b>93</b>
4.1 Introduction.....	93
4.2 Literature Review.....	94
4.2.1 Computational Modeling of Sintering Processes.....	94
4.2.2 Summary of Computational Modeling Techniques for Sintering.....	101
4.3 Numerical Modeling of Hot Compaction (Network Model).....	102
4.3.1 Formulation of the Numerical Model .....	102
4.3.2 Modeling of Unit Problem and Validation .....	104
4.3.3 Modeling of Multi-particle Problem with Boundary Conditions .....	107
4.4 Conclusions.....	118
<b>CHAPTER 5.....</b>	<b>120</b>
<b>SUMMARY AND CONTRIBUTIONS.....</b>	<b>120</b>
5.1 Summary.....	120
5.1.1 Forming of Porous Micro-features using Cold Compaction and Incomplete Sintering Method .....	120

5.1.2 Forming of Porous Micro-features and Particle/Substrate Bonding using Hot Compaction .....	121
5.1.3 Discrete Element Modeling of the Pressure Assisted Sintering Process .....	121
5.2 Contributions.....	121
5.3 Recommendations for the Future Work.....	123
<b>APPENDIX.....</b>	<b>125</b>
APPENDIX: Matlab Source Code for Discrete Element Model Simulation .....	126
<b>BIBLIOGRAPHY .....</b>	<b>142</b>

## LIST OF FIGURES

Figure 1-1 The potential of various surface modifications to enhance pool boiling (Liter and Kaviany 2001).....	2
Figure 1-2 Overview of the various production methods for porous metallic materials (Liu and Liang 20001; Davies and Zhen 1983; Banhart 2001; Banhart 2000) ..	5
Figure 1-3 Proposed fabrication method: powder pressing and powder rolling (cold/hot)	6
Figure 1-4 Illustration of the entire fabrication process.....	7
Figure 2-1 Basic powder forming process steps.....	14
Figure 2-2 Deformation behavior of powders in cold compaction (Cocks 2001) .....	16
Figure 2-3 The evolution of microstructure during sintering (German 1994).....	18
Figure 2-4 Two categories of transport (German 1994) .....	19
Figure 2-5 Continuum models (Zavaliangos 2002).....	21
Figure 2-6 Micromechanical models (Zavaliangos 2002).....	22
Figure 2-7 Representation of powder yielding surfaces of continuum model (PM Modnet Computer Modeling Group 1999) .....	23
Figure 2-8 2D sketch of the contact geometry between two spherical particles (Cundall and Strack 1979) .....	26
Figure 2-9 Simplified calculation scheme of DEM (Cundall and Strack 1979).....	27
Figure 2-10 Experimental set-up and punch/die set (Kim et al. 2007).....	32
Figure 2-11 Microchannel dimensions and measured data (courtesy of Gap-yong Kim)	33
Figure 2-12 Laser measurement system (BIM) .....	34
Figure 2-13 Copper powder .....	34
Figure 2-14 Punch load curve during die pressing .....	35



Figure 2-15 Powder compact with micro-protrusion made from the experiment .....	37
Figure 2-16 Magnified side view of successfully formed micro-protrusions.....	37
Figure 2-17 Magnified side view of unsuccessfully formed micro-protrusions.....	38
Figure 2-18 SEM of the compact surface .....	38
Figure 2-19 Pore size distribution at different cold compaction force .....	39
Figure 2-20 Hardness of the cold compacted part compressed using different force.....	40
Figure 2-21 Hardness of part sintered at different temperatures .....	41
Figure 2-22 Porosity of formed micro-features with various aspect ratios .....	43
Figure 2-23 Hardness of formed micro-features with different aspect ratios .....	44
Figure 2-24 Porosity of formed micro-features sintered at different temperatures .....	45
Figure 2-25 Cross-sectional views of the bump1 before and after sintering .....	45
Figure 2-26 The DPC model (PM Modnet Computer Modelling Group 1999).....	46
Figure 2-27 Densification behavior of the zirconia powder (Kim et al. 2000).....	49
Figure 2-28 Illustration of the FEA model.....	50
Figure 2-29 Die compaction process .....	51
Figure 2-30 Simulation validation (relative density distribution).....	52
Figure 2-31 Geometry and dimension of the die (symmetric view).....	53
Figure 2-32 Material properties used in ABAQUS (Martin et al. 2002; Park et al. 1999; Vyal and Laptev 2002).....	53
Figure 2-33 Compaction simulation validation .....	54
Figure 2-34 Shape and density of the powder compact before and after compaction.....	55
Figure 3-1 Schematic of four conventional hot consolidation processes (German 1996)	59
Figure 3-2 Forging modes and stress conditions on pores for: a) re-pressing; b) upsetting (James 1994).....	62
Figure 3-3 Experimental setup: a) compaction assembly (front view); b) compaction assembly (top view); c) compaction assembly (section view); d) whole setup	66

Figure 3-4 Die insert #1 and profile measurement of the micro-channels at different cross sections.....	67
Figure 3-5 Die insert #2 .....	68
Figure 3-6 Die insert #3 .....	68
Figure 3-7 Hot compacted part: a) successfully formed micro-features; b) magnified cross-sectional view (insert #1) .....	70
Figure 3-8 Interconnected porous structure of the formed micro-features (insert #1) .....	71
Figure 3-9 Effects of design factors on the hardness: a) response surface; b) main effect plot .....	73
Figure 3-10 Effects of design factors on the porosity: a) response surface; b) main effect plot .....	74
Figure 3-11 Magnified cross-sectional view (insert #2) .....	76
Figure 3-12 Interconnected porous structure of the formed micro-features (insert #2) ...	77
Figure 3-13 Successfully formed micro-protrusions with different taper angles (insert #3) .....	78
Figure 3-14 FEA model: a) cross-sectional view; b) boundary conditions .....	80
Figure 3-15 Heat flux input for different target temperatures: a) 400 °C; b) 450 °C; c) 500 °C .....	82
Figure 3-16 Validation of the simulation with experiment .....	83
Figure 3-17 Temperature distribution of the powder: a) 400 °C; b) 450 °C; c) 500 °C ...	85
Figure 3-18 Copper substrate with scratched surface .....	86
Figure 3-19 Particle/substrate bonding made by hot pressing .....	87
Figure 3-20 Microscopic pictures of the bonding interface.....	87
Figure 3-21 Reference for the tape test (ASTM D3359) .....	88
Figure 3-22 Specimen cutting for tape test: a) Compression cutting; b) Specimen made; c) Cutting block.....	89
Figure 3-23 Three-point bending test .....	90
Figure 4-1 Model for the neck growth problem (Hwang and German 1984).....	98

Figure 4-2 2D representation of a 2 particles model.....	99
Figure 4-3 Comparison of modeling techniques for powder sintering process .....	102
Figure 4-4 Illustration of the 2-particle pressure assisted sintering model.....	105
Figure 4-5 Comparison between simulation and experiment results.....	106
Figure 4-6 Effects of temperature and force on $r/R$ .....	107
Figure 4-7 Illustration of the 10-particle model.....	108
Figure 4-8 Frame analysis of the ten-particle system .....	110
Figure 4-9 Calculation scheme for multi-particle pressure assisted sintering problem...	111
Figure 4-10 Neck radius during pressure assisted sintering (350 °C, 10N).....	114
Figure 4-11 Relative center approaching (350 °C, 10N).....	114
Figure 4-12 Neck radius during pressure assisted sintering (384 °C, 10N).....	116
Figure 4-13 Neck radius during pressure assisted sintering (422 °C, 10N).....	116
Figure 4-14 Relative center approaching (384 °C, 10N) .....	117
Figure 4-15 Relative center approaching (422 °C, 10N) .....	117

## LIST OF TABLES

Table 2-1 F-test to determine the effect of the sintering temperatures on the hardness ...	42
Table 2-2 Material properties of zirconia powder (Kim et al. 2000).....	48
Table 3-1 Tool materials properties (CES Selector).....	64
Table 3-2 Experimental design and results .....	72
Table 3-3 Material properties used in simulation .....	81
Table 4-1 Constant n and m in Equation 5-4 (Hwang and German 1984).....	97
Table 4-2 Material property of copper (Swinkels and Ashby 1981).....	103
Table 4-3 Axial interaction force between particles .....	109

## **CHAPTER 1**

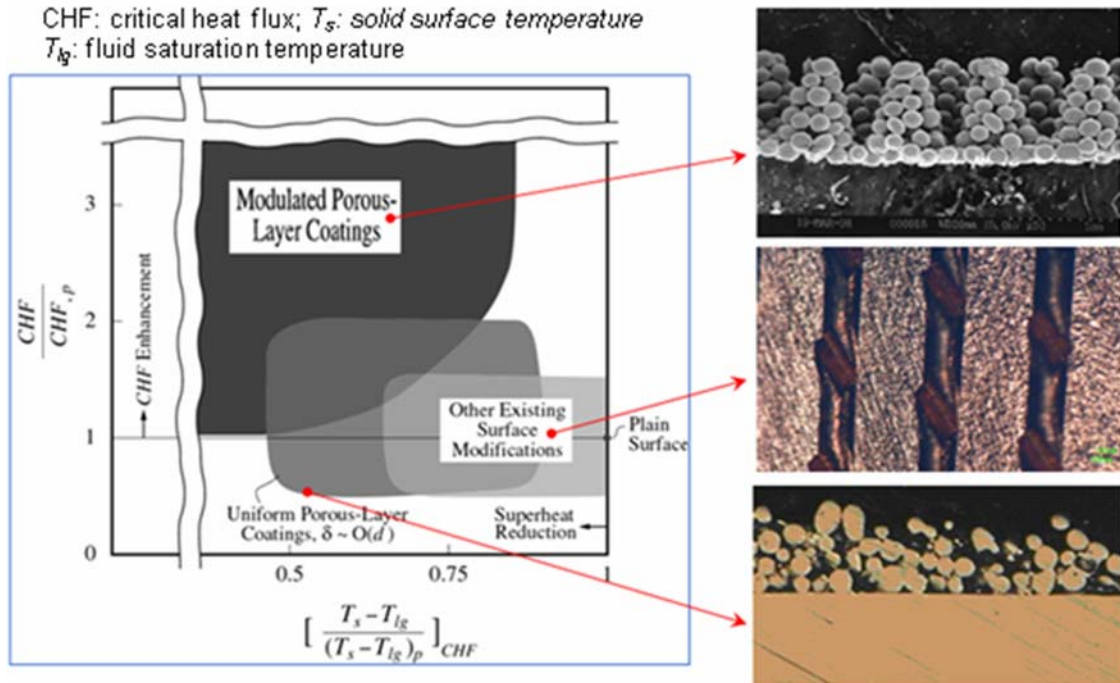
### **INTRODUCTION**

#### **1.1 Motivation**

Nowadays, the manufacturing industry has been challenged to further reduce the size of their products, due to government regulations and consumer demands for lightweight, power-efficient and portable devices. However, the performance of highly integrated devices and systems experiencing high heat loads is often limited by the internal heat generation and the associated undesirable elevated temperature levels. Examples of such circumstances can be found in electronic systems, automotive, residential and industrial equipment, which all require cooling units to sustain certain low level temperatures to ensure the expected efficiency and performance. Furthermore, the trend of increasing integrated, compact and miniaturized devices leads to even higher heat loads and compel interdisciplinary research efforts to develop advanced heat exchangers that are compact, small, efficient and inexpensive (Chen et al. 2006).

Advanced heat transfer technology in recent years has been highly dependent upon the improvement of two phase heat transfer in tubes, where phase transformation from liquid to vapor phase significantly increases the level of thermal energy transfer when compared to the single phase fluid case. For example, nucleate pool boiling is a

well-recognized and long studied method for passively removing high heat loads from a device while maintaining relatively low material temperatures. Methods to improve two phase heat transfer can be grouped as active and passive techniques. Active techniques include mechanical aids, surface vibration, fluid vibration, and the addition of electrostatic fields. Passive techniques include surface treatments, roughening and modification of the surface, surfaces extension, displaced enhancement, swirl flow techniques, alteration of surface tension, and the inclusion of additives to the coolant.



**Figure 1-1 The potential of various surface modifications to enhance pool boiling (Liter and Kaviany 2001)**

Several recent heat transfer studies indicated that porous surfaces with nano/micro-scale features lead to heat transfer efficiency improvements up to 180-300% (Kunugi et al. 2004; Liter and Kaviany 2001). Figure 1-1 presents a map of the potential

enhancement of surface modifications as collected from the published experimental data (Litter and Kaviani 2001), which indicates that porous-layer coating could further enhance the boiling heat transfer when compared to conventional surface modifications (roughening). Especially, modulated porous surface features (micro-protrusions with varying height or thickness) are experimentally shown to enhance the pool-boiling critical heat flux (*CHF*: the upper limit of the nucleate-boiling heat flux) nearly three times over that of a plain surface, and to reduce the surface superheat ( $T_s - T_{lg}$ : the area-averaged solid surface temperature ( $T_s$ ) beneath the porous-layer coating minus the fluid saturation temperature ( $T_{lg}$ )) in the meantime (Litter and Kaviani 2001).

However, the in-mold sintering fabrication method employed by Litter and Kaviani was both time consuming and costly for mass fabrication. Mass production of such surfaces requires employment of novel manufacturing processes that are robust (controlled variation), highly productive and cost-effective. Besides, for rapid implementation of such findings into consumer products, it is advantageous to make use of the existing production facilities and processes (embossing and rolling) in the heat exchanger (HVAC) industry.

Thus, the aim of this study is to develop a novel manufacturing process that will result in porous surfaces with micro-scale features on a solid thin sheet substrate in an efficient and cost-effective way. Furthermore, the author wishes to provide a deeper understanding of the basic mechanisms during this manufacturing process.

Four important aspects of the desired advanced heat transfer surface in this study are:

1. Micro-scale features (i.e., modulated protrusions) with high aspect ratio

(height/width),

2. Interconnected pores,
3. Minimized spacing between neighboring micro-feature,
4. Strong and near-zero thermal-resistant bonding with a thin substrate.

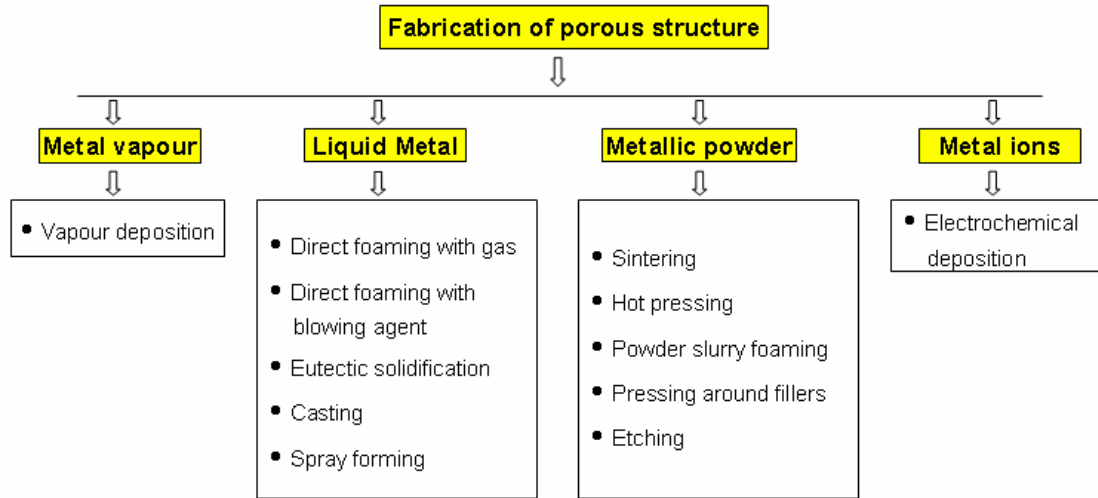
In addition to the above specifications, there are four other requirements for the desired manufacturing process so that it can be implemented rapidly into the industrial application:

1. Low fabrication cost,
2. High productivity,
3. Robustness (minimized variation),
4. Utilization of the existing production facilities and processes (embossing and rolling) in the heat exchanger industry.

From a theoretical point of view, there are many ways to fabricate metallic porous structures. Davies, Banhart and Liu provided very comprehensive reviews on the manufacturing of porous metallic materials (Liu and Liang 2001; Davies and Zhen 1983; Banhart 2001; Banhart 2000), which almost covered all the existing porous metal fabrication methods. In addition to that, Kunugi et al. employed a novel method to make a porous metallic surface or coating by chemical etching with nanoparticles (Kunugi et al. 2004). Figure 1-2 presents a classification and summary of the known methods explained in the literature (Liu and Liang 2001; Davies and Zhen 1983; Banhart 2001; Banhart 2000). These methods were classified according to the state of



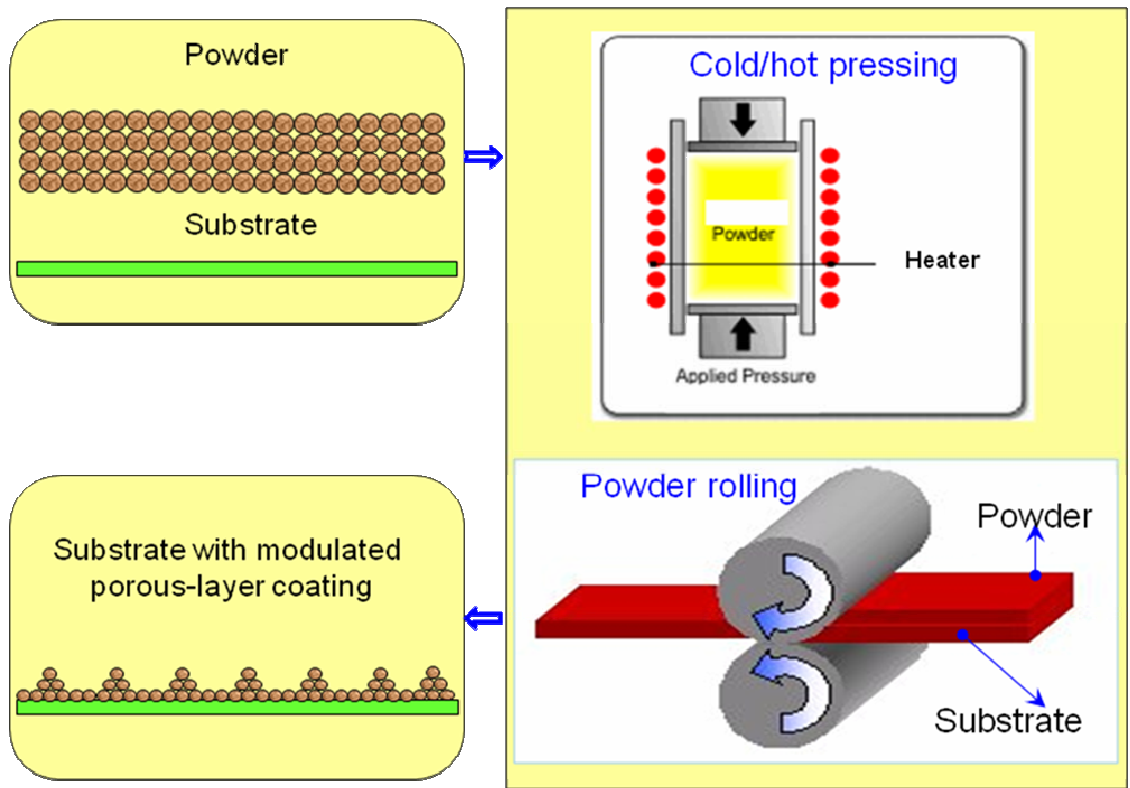
the material during processing, which defines four categories of processes as follows: 1) metal vapor, 2) metallic liquid, 3) metallic powder, 4) metal ions.



**Figure 1-2 Overview of the various production methods for porous metallic materials (Liu and Liang 20001; Davies and Zhen 1983; Banhart 2001; Banhart 2000)**

However, only a few of the above methods are likely candidates to fabricate porous surfaces under the mass production requirements. Generally speaking, three major techniques are available to fabricate porous micro-features as described in the literature (Janowski 1978; O'Neill et al. 1971; Nishikawa et al. 1979; Dahl and Erb 1976; Milton 1968; Kartsounes 1975; Fujii et al. 1979), which are: 1) powder sintering in a graphite mold with micro-cavities; 2) metal spraying onto a substrate with micro-features, such as plasma spray and flame powder spray; and 3) electroplating (electro-deposition) onto a polymeric foam with micro-features. However, all the above three methods suffer from manufacturing difficulties. For example: 1) to achieve a good product strength, a fairly high temperature (close to the material's melting temperature) is usually required for the

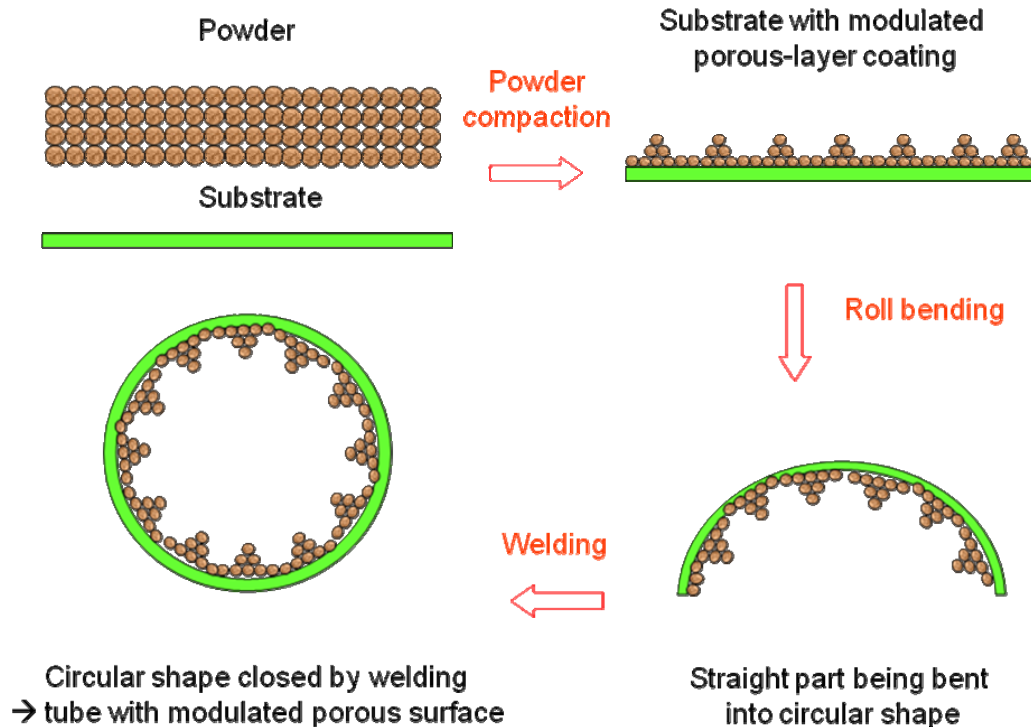
conventional sintering, which is not only difficult to perform but can also result in serious degradation of the mechanical properties of the base materials; 2) metal spraying methods lack the capability of producing micro-features with high aspect ratio; 3) the fabrication of porous micro-features with electroplating requires polymeric foam with micro-features, which is very expensive.



**Figure 1-3 Proposed fabrication method: powder pressing and powder rolling (cold/hot)**

Considering the discussions above, it is thought that mass production of porous surfaces with micro-scale features (protrusions) is reasonably feasible with adoption and improvement of metal forming processes, particularly if the metallic alloys are of interest and cost is a concern due to application requirements. Powder metallurgy combined with

metal forming processes stand out to be a practical and feasible candidate. Existing manufacturing processes such as rolling and embossing are likely candidates with further improvements and optimization to fabricate this kind of surfaces and products as they have been used in the heat exchanger industry for years, and a significant infrastructure (equipment, material supply, know-how, assembly, recycling, etc.) exists in place. Figure 1-3 illustrates the proposed fabrication method: powder pressing and rolling compaction processes. Figure 1-4 is a schematic illustration of the entire process and steps for the making of industrial tubes. The last two steps, tube rolling and welding, will not be addressed in this study. But subsequent requirements imposed by tube rolling on the previous process steps will be considered, which are mechanical strength of the porous surface and the powder-substrate bonding strength.



**Figure 1-4 Illustration of the entire fabrication process**

## **1.2 Research Framework and Objectives**

In this study, the fabrication of parts with porous micro-features for application in heat transfer has been investigated. Potentials of powder metallurgy combined with forming technology for the production of porous micro-features are assessed. Considering the design and manufacturing requirements, two potential candidate processes, cold compaction/incomplete sintering and hot pressing, have been investigated for producing micro-features.

### **1.2.1 Forming of Porous Micro-features using Cold Compaction and Incomplete Sintering Method**

In-mold sintering technique employed by Liter et al. requires high temperature (close to melting temperature), long sintering time (4 hours) and expensive graphite mold (Liter and Kaviani 2001). In addition to that, the mechanical strength of their product is poor. To overcome these limitations, this study investigates the feasibility of cold die compaction and incomplete free sintering technique for the fabrication of porous micro-features.

The major concern of the desired process is to produce part with sound mechanical strength. This study proposes to conduct a relatively high pressure cold compaction before sintering, which will not only ensure a good particle bonding strength, but also eliminate the use of graphite mold in sintering since the part after compaction can maintain its shape. To realize mass production, one of the major challenges is to reduce sintering time and temperatures. In this study, an incomplete sintering procedure is used to address these issues.

A cold compaction system has been developed and an oven is used for free sintering to study the effects of compaction force, sintering temperature and aspect ratio on feature formation process. Parts with porous micro-feature have been produced, and analyzed with hardness measurement system and image processing softwares for feature formation quality. Simulation studies have also been performed to provide a better understanding of the effect of pressure on the density distribution after cold compaction.

### **1.2.2 Forming of Porous Micro-features and Particle/Substrate Bonding using Hot Compaction**

The biggest disadvantage of the cold compaction and incomplete sintering method is that the achievable aspect ratio is low, which is caused by the low bonding strength during shaping stage (cold compaction). During cold compaction, the amount of atomic diffusion is very low, and the bonding strength of the compact is mostly obtained by the interlocking of the particles. On the other hand, hot compaction technique enhances both heat induced diffusion and pressure induced diffusion, which results in a much higher particle bonding strength.

Therefore, for applications where high aspect ratio micro-features are required, we propose to use hot pressing technique. Previous studies on the hot compaction are mostly focused on achieving fully densified product. Very few literatures could be found on the forming of porous features using hot compaction process.

A hot compaction experimental setup has been designed and fabricated that is capable of performing high temperature operation (700 °C), quick heat-up, and avoiding oxidation to study the effects of compression force and temperature on the part quality in terms of powder consolidation strength and porosity (the ratio of the volume of all the

pores in a material to the volume of the whole). In addition, the achievable aspect ratio and taper angle has been studied. 3D thermal simulation of the experimental setup has been conducted to investigate the internal temperature distribution, which is used as a reference for the experiment.

In addition to the high aspect ratio micro-features, another important requirement on the desired product is that the porous layer needs to be bonded onto a solid substrate. For the heat transfer application, the thermal resistance of the bonding interface should be minimized, which could be well achieved using hot compaction technique. During hot compaction, the substrate and particles diffuse into each other, which results in a crystallized connection area without any interface layer. On the other hand, the bonding strength is critical since the product will be subject to mechanical loadings in function. Especially for the tube application, the product will be deformed significantly. Hot pressing experiments have been conducted in this study to bond particles with a substrate. The bonding strength was tested using tape test and three-point bending.

### **1.2.3 Discrete Element Modeling of the Pressure Assisted Sintering Process**

In the forming of porous micro-features using hot compaction process, it is costly and time-consuming to determine a proper experiment setting (force, temperature and time) by trial and error. Product qualities, such as mechanical strength and porosity, are significantly affected by the setting of those process variables.

Existing models are not appropriate for our problem. Therefore, in order to virtually study the effect of the force and temperature on the particle bonding strength and porosity, a discrete element model for pressure assisted sintering has been developed for the forming of porous micro-features. The model was first validated with

experimental results for a unit problem (two particles). And then it was expanded for a 10-particle channel hot pressing problem. With this model, we could conveniently assess the effects of force and temperature on the particle bonding strength and shrinkage, which then give us insight on deciding a proper process setting before the actual operations.

### **1.3 Dissertation Organization**

The remainder of the dissertation is divided into four chapters. Discussed in chapters 2 and 3 are two manufacturing technologies that may be capable of producing porous micro-features. Chapter 2 investigates potentials of the cold compaction and incomplete sintering technique for porous micro-feature forming. Experiments were performed to understand the effects of process parameters, and the potentials of the technology are discussed. A finite element model for the cold compaction process was also developed. In chapter 3, a hot compaction system was developed and used for the forming of high aspect ratio porous micro-features. Bonding experiment between particles and substrate was conducted and the bonding strength was tested. In chapter 4, a computational model for the pressure assisted sintering process was developed and was used to study the effect of the process variables on the product quality. Dissertation summary and contributions of the study are presented in chapter 5.

**CHAPTER 2**

**FORMING OF POROUS MICRO-FEATURES USING COLD COMPACTION  
AND INCOMPLETE SINTERING METHOD**

**2.1 Introduction**

Recently, the potentials of the powder metallurgy (P/M) in the field of manufacturing micro/meso-scale part have been recognized. Regarding micro-manufacturing, this potential arises from the fact that it is a consolidation process of tiny particles. With a mold, such as die used in metal forming, it could mass produce complex parts with good mechanical properties and precision. Most importantly, porous metallic structure could be easily obtained using this technique.

However, since the application of porous micro-features is relatively new, very few existing studies touched upon this area. Researchers who attempted to make such product are usually from other research fields other than manufacturing science and engineering. Therefore, the techniques they employed are not designed for mass production environment and costly, and the samples they make are not durable. For example, Liter and Kaviany used in-mold sintering technique to create porous micro-features (Liter and Kaviany 2001), which requires a long sintering time (4 hrs), high sintering temperature (over 1000 °C), costly machining of micro-cavities on the graphite



mold. In addition, the particle bonding strength made by this technique is poor. The micro-features could be easily crushed by fingers (Chen et al. 2006).

Therefore, in this part of our study, we employed cold compaction and incomplete free sintering technique for the fabrication of porous micro-features. With the help of cold compaction for obtaining the shape of the micro-features, no mold is required for sintering, and the required free sintering time and temperature are significantly reduced. Meanwhile, the product strength is enhanced.

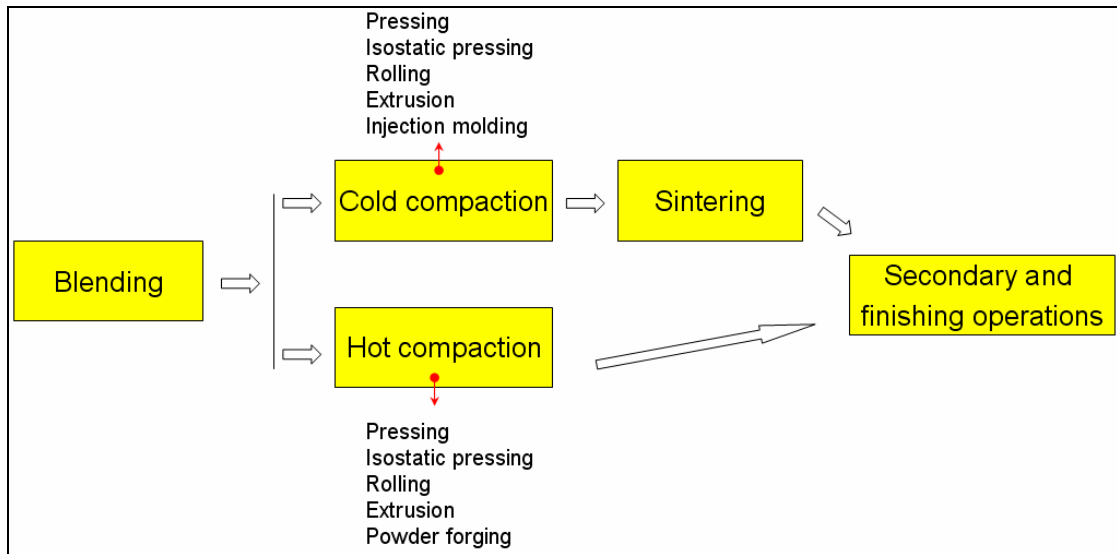
## **2.2 Literature Review**

Powder metallurgy (P/M) was practiced long before ancient artisans learned to melt and cast iron. Egyptians made iron tools using P/M techniques from at least 3000 B.C. Ancient Inca Indians made jewelry and artifacts from precious metal powders. The first modern P/M product was the tungsten filament for electric light bulbs developed in the early 1900s. This was followed by tungsten carbide cutting tool materials in the 1930s, automobile parts in the '60s and '70s, aircraft turbine engine parts in the '80s and parts made by powder forging (P/F), metal injection molding and warm compacting in the '90s.

Powder compaction is a process in which a granular, agglomerated or powdery material is consolidated into a single body by the application of a compressive force through the boundary walls of its container. In manufacturing applications, compaction is employed to form machine parts from metal powder precursors. In civil engineering application, it is used in site evaluation prior to construction. It also found use in the food industry manufacturing applications, for example, cereal compacts and cheeses. Similarly, for energy production application, it can be seen in the manufacturing of coal logs and briquettes for burning. Finally, compaction is also the key stage in the

pharmaceutical manufacturing.

As shown in Figure 2-1, the consolidation of metal powders into useful products generally follows a three-step process: (1) powder blend and transfer into a container or die, (2) powder compaction: the metal powder is compacted by placing it in a closed metal cavity (die) under pressure, and (3) sintering: compacted material is placed in an oven and sintered in a controlled atmosphere at high temperatures, and the metal powders coalesce to form a solid. Particular processes combine two of these steps into one. For example, hot compaction combines steps (2) and (3) through the simultaneous application of pressure and temperature. Proper design of compaction processes requires an adequate description of the mechanical and thermo-mechanical behavior of the powder.



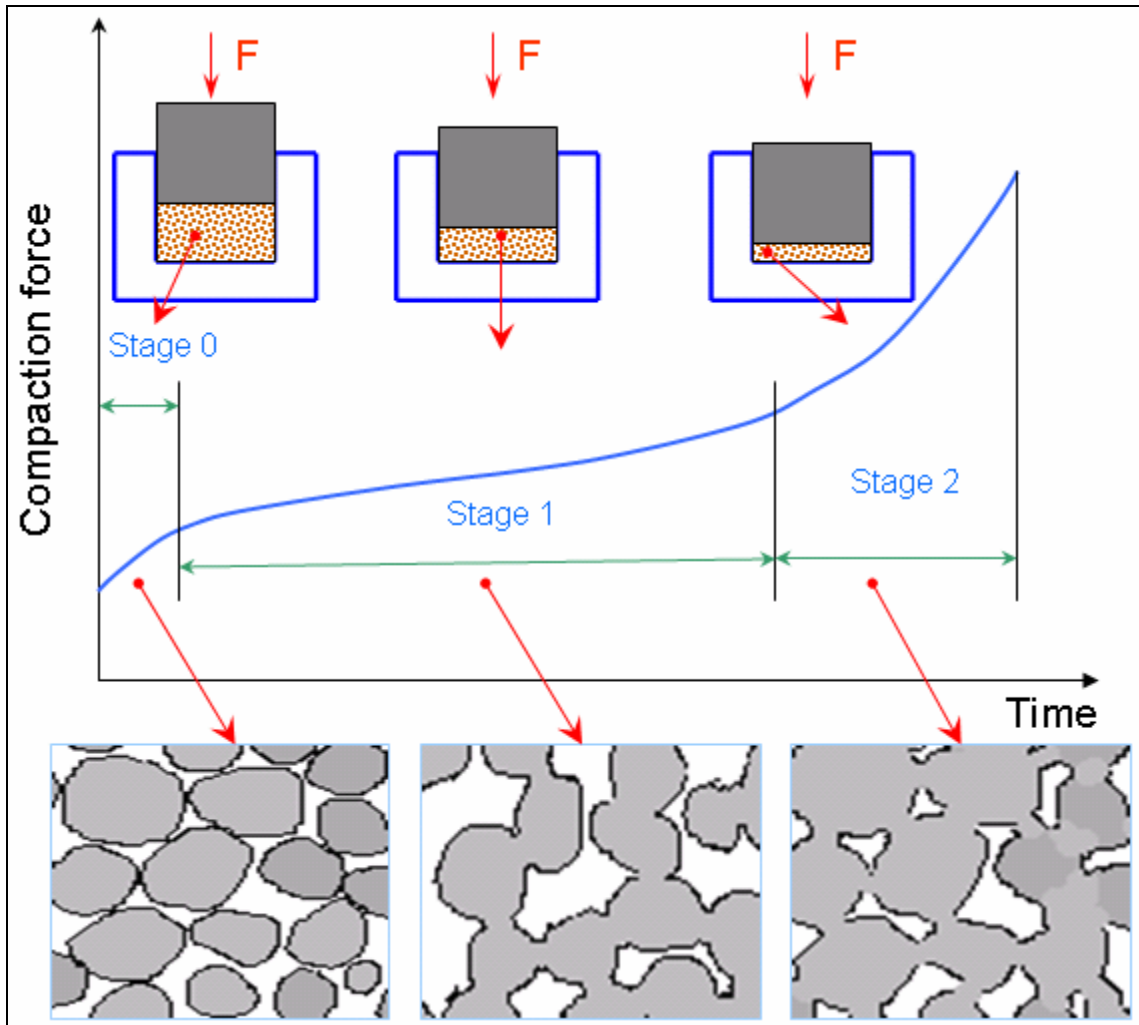
**Figure 2-1 Basic powder forming process steps**

### **2.2.1 Deformation Behavior of Powders in Cold Compaction**

It is necessary to recognize the major physical phenomena that occur during the

compaction as powders are deformed, and to determine how the macroscopic behavior and properties are influenced by them. When the powder is initially poured into a die or mold cavity, the particles are arranged randomly such that particles are only in point contact with each other. As shown in Figure 2-2, the compaction process can be divided into three main distinctive stages (Cocks 2001). Initially, the packing of particles is loose and in the early stages of compaction particles are rearranged (we will refer to this as stage 0 compaction). As further compaction force is exerted onto the powders, the relative density ( $RD$ , which is defined as the ratio of the density of the compact to the full density of the material) increases, and further compaction is accommodated by plastic deformation of the particles. During the initial stages of plastic deformation, the porosity is quite open, and deformation is localized in the vicinity of the necks which form and grow between the contacting particles (stage 1 compaction). At higher relative densities (as a result of increasing compaction force), the networks of interconnected channels deform and will be closed to form a distribution of isolated pores (stage 2 compaction). The internal structure (i.e., porosity and density) changes significantly during this stage. In our case, stage 2 compaction should be avoided to ensure that the pores are interconnected.

Throughout these process sequences, because of the initial random configuration of powders, the porosity is also randomly distributed throughout the material, particularly during stage 1 compaction. If, particularly, the specimen in the die cavity is much larger than the mean particle size, no preferred orientations or distributions of pores, and the overall structure can be assumed to be macroscopically isotropic.



**Figure 2-2 Deformation behavior of powders in cold compaction (Cocks 2001)**

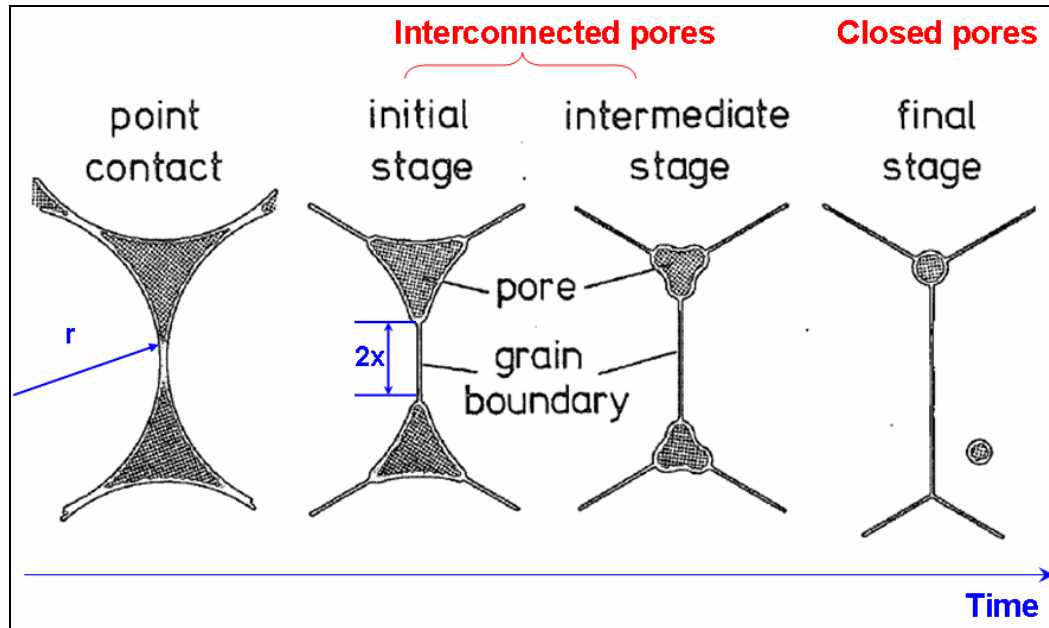
The inter-particle bonds that form due to compaction provide the green strength. These solid interfaces are created by deformation at the initial point contacts between particles. A high initial packing density aids the formation of inter-particle bonds. Due to the effect of the particle surface film, a clean powder surface is required to achieve a stronger bond. Usually, when the compaction force is sufficiently high, shear forces will act to disrupt surface films. The attractive forces between particles are weak. It is only after sintering that substantial strength increase is observed. Forces that bond particles together are mechanical interlocking, inter-atomic force and electrostatic force across the

interface (German 1994; Arakawa and Yasuda 1977). Inter-atomic force and electrostatic force are stronger with smooth, clean surfaces. However, mechanical interlocking makes the major contribution to green strength and it is enhanced by an irregular particle shape (German 1994).

### **2.2.2 Sintering Process**

Sintering is usually evident at temperature in excess of approximately one-half of the absolute melting temperatures. However, since materials melt over a wide range of temperatures, sintering is also performed over a corresponding wide range of conditions (German 1996). During sintering, particles are bonded together by atomic transport events. The driving force for sintering is a reduction in the system free energy, which is achieved by reduction of surface curvatures and elimination of surface areas (German 1994). Initially, a grain boundary is formed at the contact between neighboring particles. Atoms travel along this boundary and along the particle free surface to the neck regions. In classic sintering theory (German 1994), five distinct mechanisms are thought to contribute to the sintering of metallic particles of conventional sizes: (1) surface diffusion, (2) lattice (volume) diffusion, (3) grain boundary diffusion, (4) evaporation-condensation and (5) plastic flow. According to the evolution of the microstructure as shown in Figure 2-3, sintering process could be divided into three stages (German 1994): (1) during initial stage, the neck radius and particle radius ratio ( $x/r$ ) is usually less than 0.3. The driving force is the sharp curvature gradients at the neck, which guides the mass flow. The pore structure is open and fully interconnected; (2) in the intermediate stage, the pores have a smoother cylindrical structure and are still interconnected. The driving force is the interfacial energy (surface and grain boundary energy); and (3) at the end of the

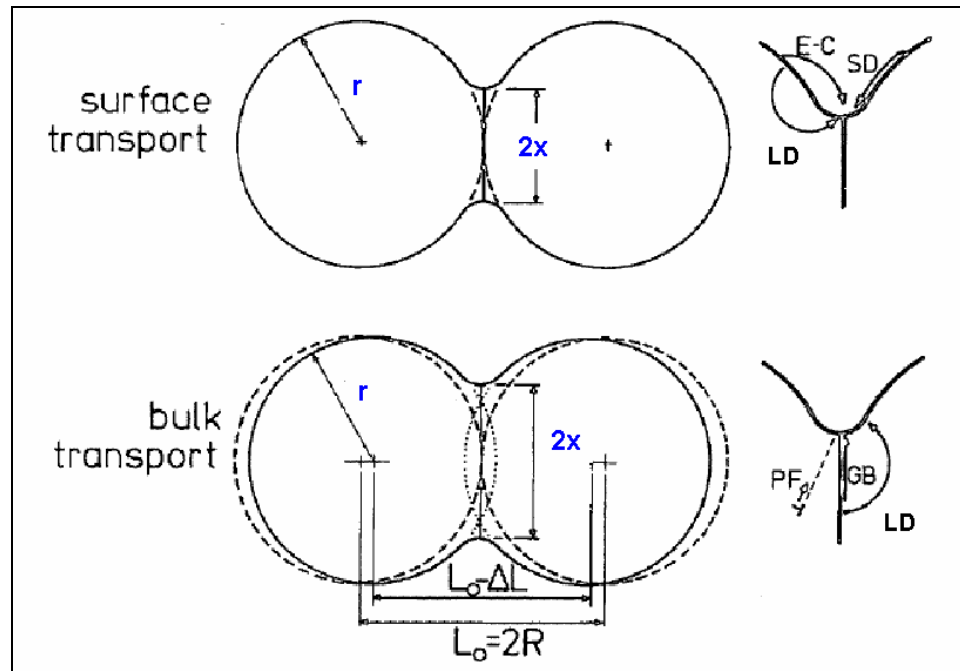
intermediate stage, the grain growth and pore shrinkage occur, and finally the pores become isolated, which signals the beginning of the final stage of sintering. The driving force is the elimination of the pore-solid interfacial area. Densification usually occurs in this stage.



**Figure 2-3 The evolution of microstructure during sintering (German 1994)**

In a response to the driving force, the mass flows via different transport mechanisms. As shown in Figure 2-4, there are two transport mechanism categories (German 1994): (1) *surface transport*, which involves neck growth without a change in particle spacing (no densification). Surface diffusion and evaporation-condensation are the two most important contributors, while lattice diffusion from surface sources is also possible but not often observed; and (2) *bulk transport* involve lattice diffusion, grain boundary diffusion and plastic flow. Plastic flow is not significant unless an external force is applied (pressure assisted sintering). Since the bulk transport processes provide

atoms for neck growth using internal mass sources, densification (shrinkage) will occur as a result.



**Figure 2-4 Two categories of transport (German 1994)**

### 2.2.3 Computational Modeling of Cold Powder Compaction

In the context of modeling the powder compaction process, a constitutive model requires the mathematical description of the behavior of the powder compact in response to external loads. On the basis of length scales, modeling methodologies for powder compaction can be classified into three categories (Zavaliangos 2002): (1) continuum models; (2) multi-particle models (discrete element models & particle dynamics models); and (3) atomistic/molecular dynamics models. We will present these three modeling approaches in the following sections.

### 2.2.3.1 Continuum Models for Powder Compaction

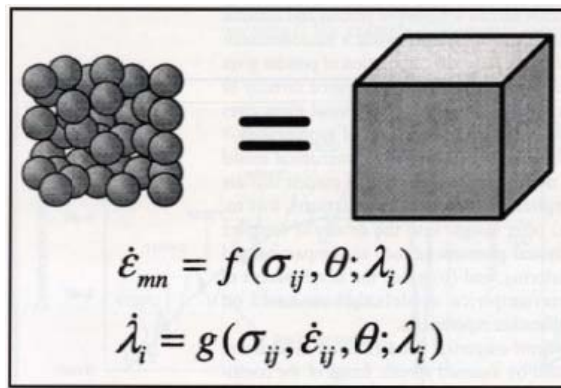
Continuum models address the geometric scales of the order of the product dimensions. Thus, they are attractive in practical applications. The evolution of external variables such as stress is expressed on the basis of fundamental balance equations and constitutive laws. The constitutive laws are expressed in terms of specific material properties. If necessary, material properties can be considered as functions of a few representative variables that describe the microstructure (internal variables). The practical application of these models requires an implementation procedure to existing finite element software. Such continuum models consist of the stress-strain ( $\sigma$ - $\varepsilon$ ) relation that also reflects its dependence on temperature ( $\theta$ ) and internal structure as shown in Figure 2-5. Microstructural characteristics are introduced via a small number of internal variables ( $\lambda$ ) that evolve during the process. For example, one variable that is usually considered in powder compaction is the relative density ( $RD$ ), which represents the local porosity state during compaction. All aspects of the constitutive model depend on this variable. The elastic constants and the yield locus that determines the level of stress required to change the shape of the compact permanently depend on the level of porosity. The flow rule that dictates the mode of deformation, in response to the external stresses during plastic flow, is also a function of porosity.

The dependence of each part of the constitutive model on external parameters (stress and temperature) and internal variables ( $RD$ ) is expressed through functional forms. For example, the yield locus in compaction can be written as (Green 1972; Shima and Oyane 1976):



$$A(RD)\sigma^2 + B(RD)p^2 = 1 \quad (2-1)$$

where  $p$  indicates the hydrostatic pressure. The specific parameters ( $A$  and  $B$  in Equation 2-1) can be determined using: (a) *micromechanical models* or (b) *empirical (phenomenological) models* that are calibrated via experiments. These constitutive laws can be conveniently applied into available FEA softwares, and the computation speed is relatively fast. Therefore, continuum models are very popular in the industrial applications of powder forming for complicated geometries.

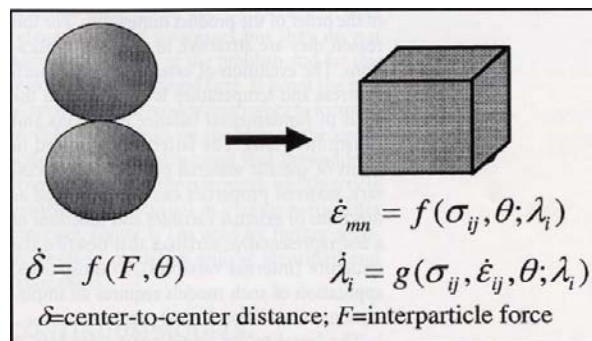


**Figure 2-5 Continuum models (Zavaliangos 2002)**

*Micromechanical models* provide a way to derive macroscopic model parameters from information on a smaller length scale (particle level), as shown in Figure 2-6. The micro-to-macro transition is performed usually by homogenization techniques. For example, macroscopic compaction models can be derived by considering the interaction of two spheres under a central force. Examples of micromechanical models are Gurson model for porous plasticity (Gurson 1977) and Arzt's model (Arzt 1982).

Micromechanical methods offer a systematic and usually a rigorous approach to describe the behavior of porous materials, but their predictive capability can be limited by

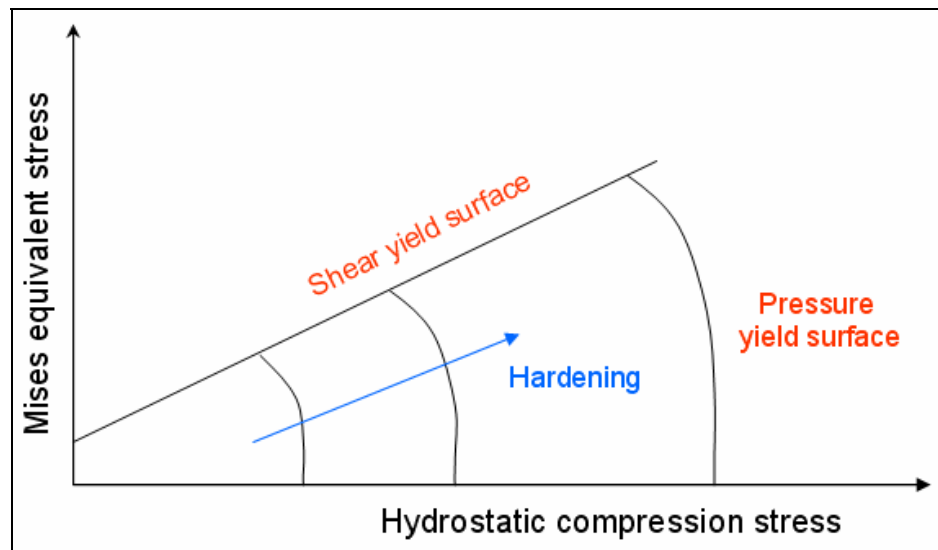
the accuracy of the unit problem solution, and the homogenization technique. Moreover, micromechanical models describe only some of the existing physical phenomena. For example, in compaction, only plastic deformation is taken into account while other phenomena such as rearrangement and fragmentation of the particles are usually ignored. As a result, the predictive capability of micromechanical model is restricted to situations that are consistent with the underlying assumptions and within narrow windows of process and material variables.



**Figure 2-6 Micromechanical models (Zavaliangos 2002)**

*Empirical models* are based on assumed specific forms of the constitutive laws. They are formulated using several ‘material’ functions that are needed to describe the response of a specific porous material to stress. Their functions must be calibrated by suitable experiments so that they can simulate the exact stress condition. Empirical models for compaction have their origin in the early 1970s (Green 1972; Shima and Oyane 1976), and represent a natural evolution from the earlier empirical approach of pressure-density equations. In these early compaction models, the role of the three dimensional stress states was recognized, and the idea of a yield locus as a symmetric ellipse in the hydrostatic press-equivalent stress space was put forward. The axes of the

ellipse are to be calibrated by simple die compression experiments. This approach is straightforward and attractive. The resulting models guarantee predictive capability under the experimental conditions used for the material calibration. Even different models give similar predictions when deviation from the calibration conditions is small (PM Modnet Computer Modeling Group 1999). Empirical models are based on the yielding behaviors of the powder under loading. The powder volume must yield under pressure or local shear stresses as a consequence of powder particles sliding over each other. The analysis of this aspect of compaction has been borrowed from the principles that have been developed for soil consolidation in civil engineering studies (Lewis and Schreffler 1987).



**Figure 2-7 Representation of powder yielding surfaces of continuum model (PM Modnet Computer Modeling Group 1999)**

The compression and shear yielding of the powder is usually represented in terms of hydrostatic pressure stress and Mises equivalent stress as shown in Figure 2-7 (PM Modnet Computer Modeling Group 1999). For powders, the position of the pressure yield surface depends on the density and generally achieves a higher level as densification of

the powder takes place. This is referred to as hardening since the powder becomes harder to yield as it becomes denser. When the stress level is within the region enclosed by the two surfaces, the powder behaves as an elastic system. When the stress level reaches the boundary, then yielding by appropriate mechanism (shear yielding or pressure yielding) takes place. This is generally dominated by failure as a result of pressure. There are a number of yield models that include the features as described above, such as Cam Clay (Roscoe and Burland 1968) and Drucker-Prager/Cap (Drucker et al. 1957). According to Zavaliangos, the CPU time of running a continuum model simulation with 100x100 2D elements or 20x20x20 3D elements on a 1Ghz/256M PC is 1-2 hours (Zavaliangos 2002).

### **2.2.3.2 Multi-particle models for powder compaction**

Each particle of an assembly is modeled separately by this method. This approach involves the numerical simulation of individual particles that interact, based on a set of prescribed contact conditions. Comparing to the continuum modeling method, particle-level simulation of powder compaction has the following advantages: (1) it can mimic the particle movement and rearrangement behaviors, which in turn increases the accuracy of the calculation results. For example, it can simulate the powder transfer behavior; (2) the evolution of the microstructure such as pore size could be directly obtained; (3) multi-particle models eliminate the need to establish bulk powder properties, it simply requires the properties of the stock material, and these are easier to find experimentally; (4) furthermore, when there are very small features (close to the particle diameter) on the part in the compaction simulation, multi-particle models are preferred since the deformation behavior at the small feature locations is largely depending on the particle movement. For instance, Cameron and Gethin employed the multi-particle technique to

investigate the effect of the surface roughness on the powder compaction performance.

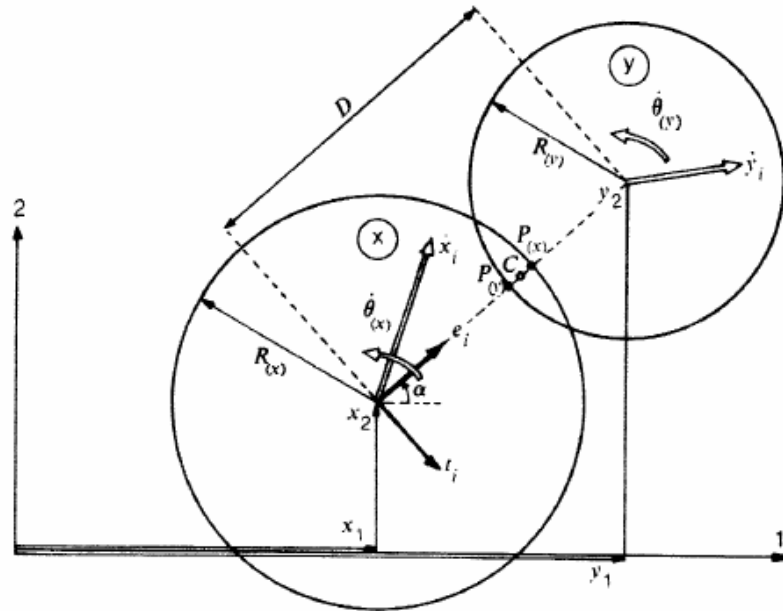
The initial step of all the available multi-particle models is the generation of the random packing of particles. The use of computer simulation in the study of random packing of particles was first introduced in the 1970s, and many models have been developed. These models can be classified into two classes: (1) *sequential generation method* (Matheson 1974; Lu and Shi 1994). By this method, only one particle is generated each time and added to the surface of the existing particle based on some criteria. The process is repeated to form a cluster of many particles; (2) *collective-relocation method* (Jodrey and Tory 1985; Nolan and Kavanagh 1992). In contrast to the first method, many particles are initially placed randomly in a confined space. Overlaps between neighboring particles occur as a result of random packing. The particles are first relocated according to an algorithm to minimize the existing overlaps; then, particles are shrunk or deleted to eliminate the remaining overlaps. The final overlap-free packing will be obtained by repeating these two steps a few times.

Based on the difference in the modeling of particle interaction forces, the available particle-level compaction models (second step of multi-particle modeling) could be further divided into two categories: (1) *discrete element method*; (2) *particle dynamics*. The first method will be described in details as follows.

#### Discrete/distinct element method (DEM)

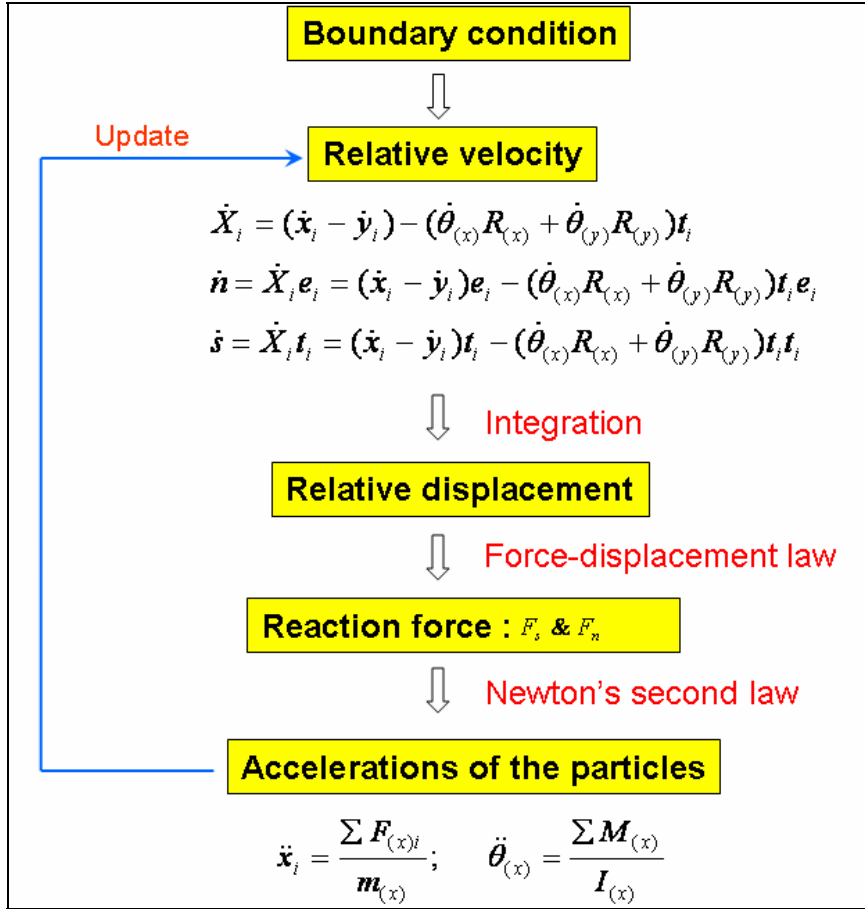
The DEM stems from the studies in soil mechanics area (Cundall and Strack 1979), which can provide significant information on particle motion, contact forces, and several macroscopic quantities in an assembly of particles subjected to external loads, or

displacements. DEM has already been widely applied to the modeling of powder compaction (Lian and Shima 1994; Gethin et al. 2001).



**Figure 2-8 2D sketch of the contact geometry between two spherical particles (Cundall and Strack 1979)**

In a 2-dimensional case, the particles are modeled as spheres as shown in Figure 2-8. It is assumed that particles in the compact displace independently from one another and interact only at contact points. The interactions of the spherical particles are accounted for by modeling the evolution of the packing as a dynamic process. Simply speaking, the calculation scheme of DEM can be depicted by Figure 2-9. The dynamic behavior of each particle is governed by the Newton's second law as if it is a rigid body. The deformations at the contact points are described by a given force-displacement law.



**Figure 2-9 Simplified calculation scheme of DEM (Cundall and Strack 1979)**

Different researchers have developed different constitutive equations for the force-displacement law of DEM (Cundall and Strack 1979; Storåkers et al. 1997; Shima et al. 1995). Among them, the one used by Shima et al. showed a very good agreement with the experiment (Shima et al. 1995). As shown in Equation 2-2, when the deformation ( $\delta$ ) of the contact area is in the elastic range, the normal force will equal to the Hertzian force  $F_E$ ; when the plastic deformation starts, the normal force will be calculated according to the second equation ( $F_p$ ), which is calibrated from a micro-compression test and  $k_f$  is a factor that is related to the flow stress of the particle material.  $\delta_p$  is obtained from  $F_E = F_p$ , and the term  $c_n \dot{n}$  corresponds to the damping force in

normal direction.

$$F_n = \begin{cases} F_E = 0.733E \sqrt{\frac{R_i R_j}{R_i + R_j}} \delta^{\frac{3}{2}} + c_n \dot{n}, & \text{when } \delta \leq \delta_p \\ F_p = \frac{\pi}{2} \bar{R} \delta \times k_f + c_n \dot{n}, & \text{when } \delta \geq \delta_p \end{cases} \quad (2-2)$$

where  $E$  is Young's modulus,  $R_i$  and  $R_j$  are the radii of the contacting particles and  $\bar{R}$  is an effective radius.

Some recent discrete element models treat particle as a deformable body that may be mapped by a finite mesh and the mechanical behavior of the particle under loading is also included in the analysis (Munjiza et al. 1995; Ransing et al. 2000; Ransing et al. 2004). This approach allows the inclusion of failure at the particle level, due to either ductile or brittle mechanisms.

When plastic deformation occurs, the excess material at the contact between the two overlapping particles is transported away from the contact zone. Depending on the constitutive behavior of the powder, the material may be deposited far away from the contact zone or stay in the vicinity of the contact. For two particles indenting normally, the evolution of the contact area has been formulated by Storåkers and his coworkers (Storåkers et al. 1997).

Due to the explicit nature of the model, the numerical scheme will be unstable if the time step  $\Delta t$  is taken as a fraction larger than one of the critical time step. The critical time step could be determined according to (Cundall and Strack 1979):



$$\Delta t = 2 \times \sqrt{\frac{M}{k}} \quad (2-3)$$

where  $M$  is the smallest particle mass of the compact and  $k$  is the approximate contact stiffness given by the constitutive equations.

Due to the assumption that the shape of the particle is regular circle and the fact that the force-displacement law is very simple, some researchers further simplified the DEM model to a truss model (Heyliger and McMeeking 2001; Newell et al. 1995). With this method, each particle is simplified into a node, and a truss element was established between contacting nodes.

The increase of computational power and the development of special integration algorithms have rendered DEM increasingly attractive because 3D problems involving thousands of particles can be handled now on a personal computer. However, there are still limitations, for instance, 10,000 particles in a 3D problem correspond to only 20-25 particles in each direction. For typical particle dimensions of 50  $\mu\text{m}$ , the corresponding macroscopic dimension addressed is about 1mm. Furthermore, if there is a size distribution, then the number of particles that must be included increases dramatically (Zavaliangos 2002). As a summary, this approach may be suitable for the problem in our hands that involves compaction of particulate materials into micro-scale cavities.

### **2.2.3.3 Atomistic/molecular dynamics models**

On much smaller scales, molecular dynamics (MD) techniques address the response of individual atoms under mutual interactions. In the molecular dynamics (MD) technique, the trajectories of particles are generated by solving Newton's equations of

classical mechanics (Heyes 1998). There are fundamental limitations in MD simulations imposed by computer speed and memory of modern computers and algorithmic restrictions. Therefore, both the length and the time scales that can be addressed practically today are infinitesimal compared to practical applications.

Recently, Sanchez-Castillo carried out simplified molecular dynamics simulations of the compaction of a single (Sanchez-Castillo and Anwar 2003), three-dimensional model granule composed of 1004 spherical particles interacting through a Lennard-Jones interaction potential. This representation enabled the modeling of substantial deformation and also captured some of the behavior of real materials during compaction. He also used this methodology to investigate the effects of varying compaction speed (strain rate) on the deformational behavior of the granule. However, his simulation conditions were not suitable for micro-scale particles since: (1) the particle was assumed to be composed of 1004 atoms, but in reality, a 10  $\mu\text{m}$  particle will have  $10^{12}$  atoms (assuming the size of atom is 0.3 nm), which is out of the computational ability of the current computer (able to handle  $10^5$  atoms); (2) Sanchez-Castillo assumed that the particle is a single crystal, but a real particle usually has a polycrystal structure, which imposes another difficulty in the MD modeling, that is, how to effectively define the grain boundary in a single particle.

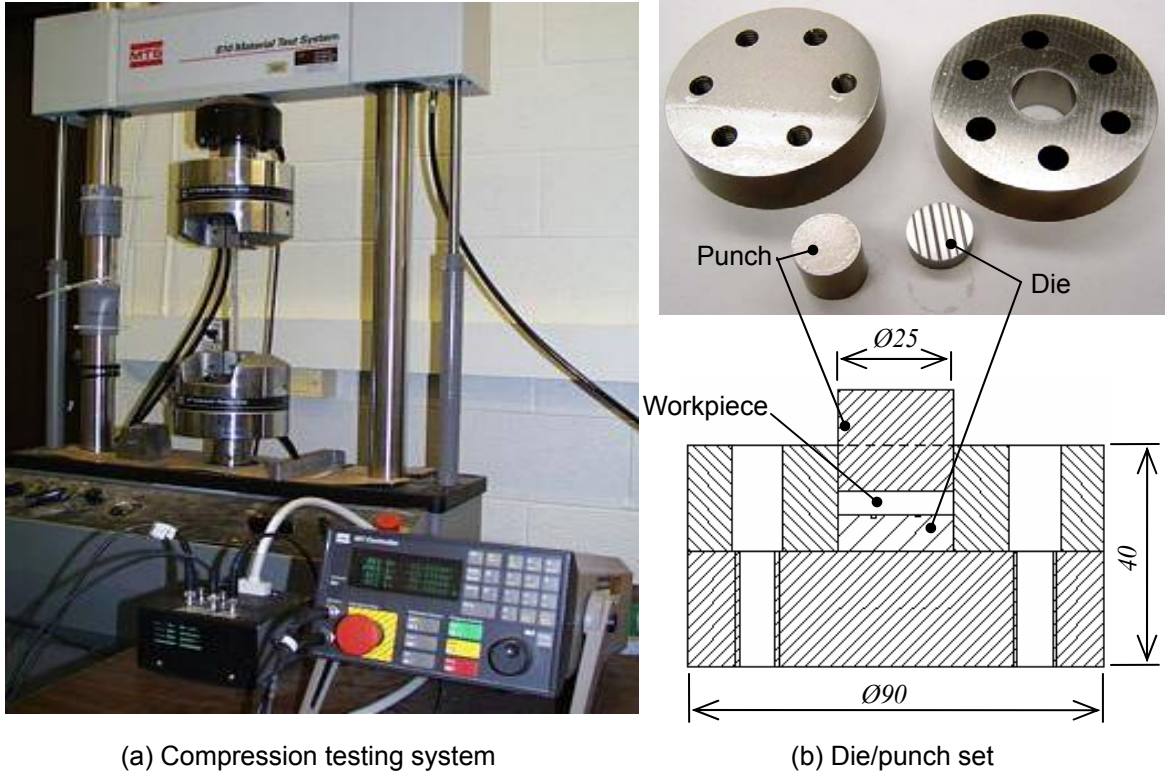
### **2.3 Experimental Investigation**

Experimental work has been performed to investigate the possibility of forming porous micro-features using cold compaction and incomplete sintering process. Important process parameters were identified and assessed. This section describes the experimental procedures and the discussion of the results. Due to its high conductivity and relatively low cost, copper is usually in the heat transfer industry. Therefore, the material used in

this study was copper powders.

### **2.3.1 Experimental Set-up and Procedures**

To investigate the consolidation performance of the powder into micro-scale features, close die compaction of copper powder was carried out. The experimental set-up consists of a compression testing system and a die/punch set as shown in Figure 2-10. MTS model 810, a compression testing system which had a maximum capacity of 100 kN, was used in the experiments. The MTS system is controlled by a computer, allowing the operator to select the speed of the punch travel into the die and the final load applied to the workpiece. Hydraulic grips are used to mount the upper and lower platens. The upper grip is stationary, and the lower grip moves up and down. The die/punch set was placed between the upper and lower platens of the MTS testing system, and force – displacement data were recorded during the compression experiment. The punch speed was set to constant values throughout the experiments: 0.2 mm/min. Each experiment was stopped at a target maximum load and then released. Designed by Kim et al., the die/punch set was fabricated from tool steel D2 (Kim et al. 2007), and was precision ground to make sure a perpendicular compression.

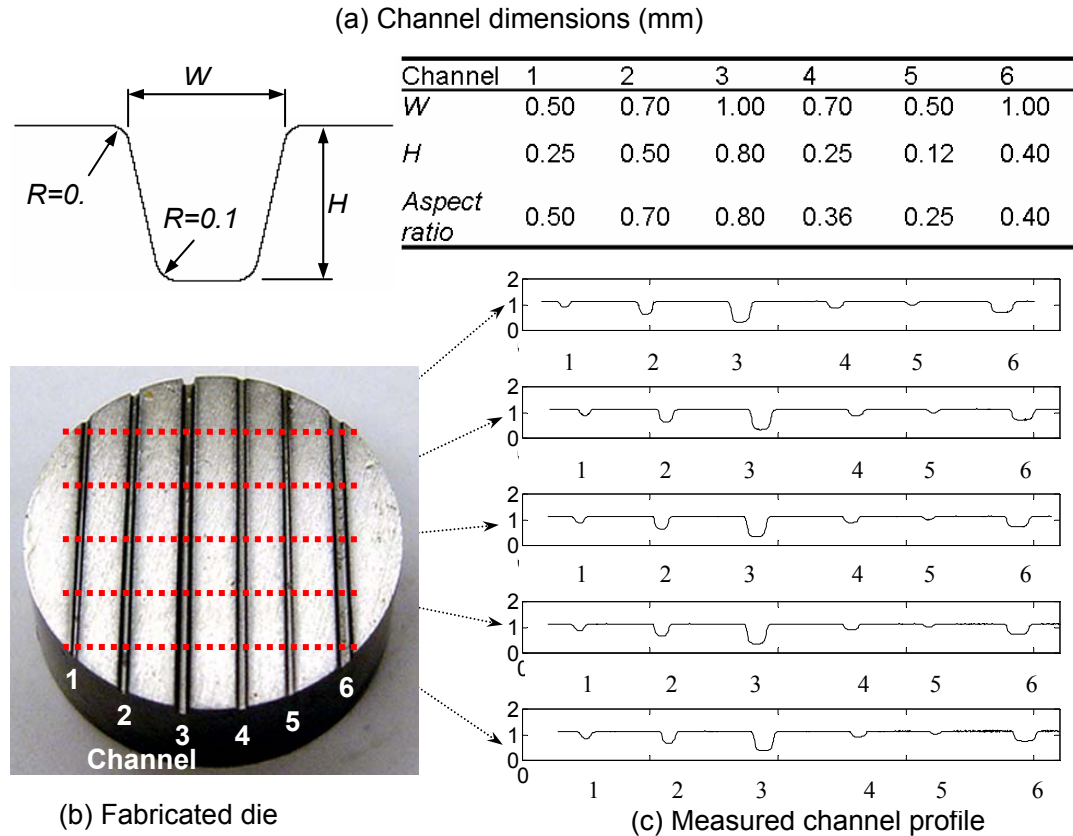


(a) Compression testing system

(b) Die/punch set

**Figure 2-10 Experimental set-up and punch/die set (Kim et al. 2007)**

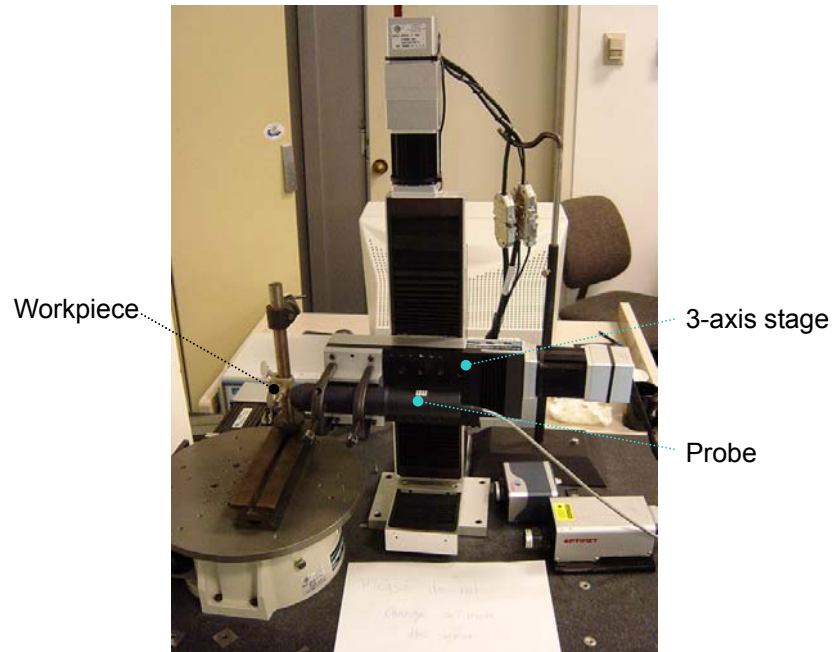
Detailed channel geometries of the die are shown in Figure 2-11. Six channels with different aspect ratios were engraved on the die by electro-discharge machining (EDM) process. To ensure the geometry of the channels are consistent after EDM, their profiles were measured by Blade Inspection Machine (BIM) at five different cross sections as shown, which indicated consistent channel geometry. BIM is composed of a laser scanning probe and 3 axis stages as shown in Figure 2-12.



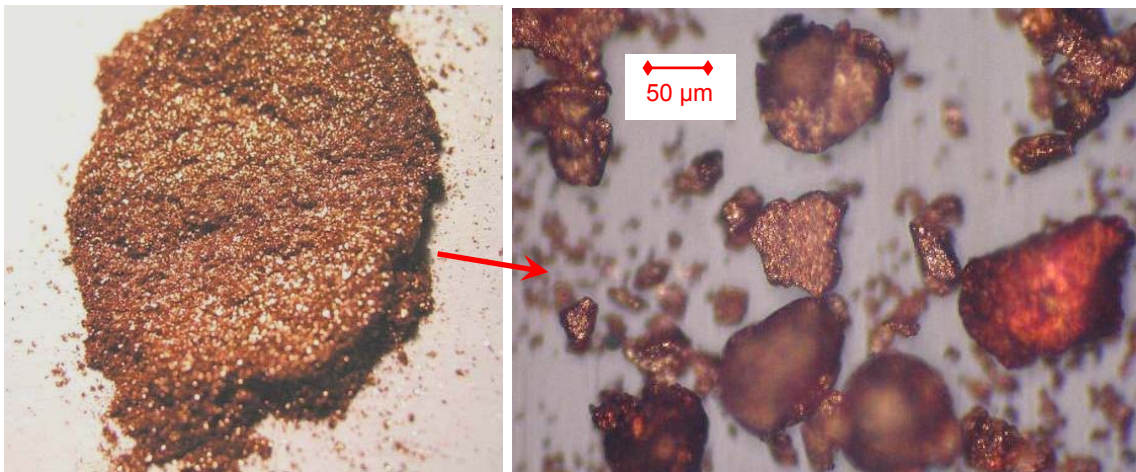
**Figure 2-11 Microchannel dimensions and measured data (courtesy of Gap-yong Kim)**

The copper powder used was Grade 185E from ACuPowder International, LLC (NJ, USA), which was produced by water atomization. As shown in Figure 2-13, the powders have irregular shape and show large variation in size (10% of particles are finer than 25  $\mu\text{m}$ , 50% of particles are finer than 50  $\mu\text{m}$ , and 90% of particles are finer than 100  $\mu\text{m}$ ). In this phase of study, we chose to use these nonuniform-size and irregular-shape powders due to the following reasons: 1) the large size distribution in the powders actually helps to improve the amount of diffusion bonding according to (German 1996), which will result in a better part mechanical strength; 2) the irregular shape introduces the interlocking of particles, which will also result in a better part mechanical strength (German 1994); and 3) the cost of the water atomized powder is very low, and would be

preferred in the practical application to reduce manufacturing cost.



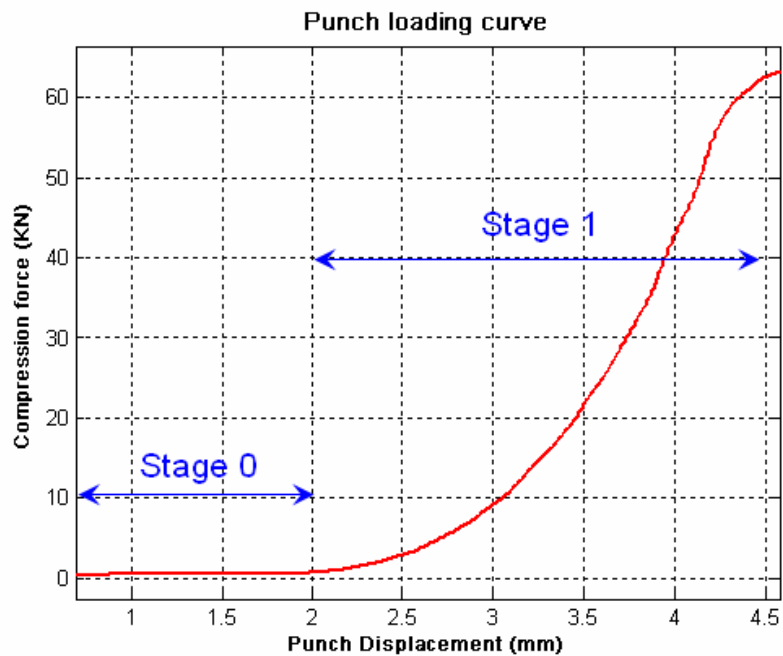
**Figure 2-12 Laser measurement system (BIM)**



**Figure 2-13 Copper powder**

In an effort to increase the compression force on the powder compact in the channel during the compression, the die was placed on the top of the powder. This

compaction set filled with powder was then put onto the MTS machine to undertake compression load. Figure 2-14 shows the evolution of the punch loading force as a function of the punch displacement, which indicates that the punch load was very low and did not increase much at the stage 0 compaction. In the stage 1 compaction, the compaction force increased dramatically at a high rate. Stage 2 compaction did not occur since the compression force was not large enough to pinch off the interconnected pore structure, which was not desired in our study. The maximum compression force in this case was about 63KN.



**Figure 2-14 Punch load curve during die pressing**

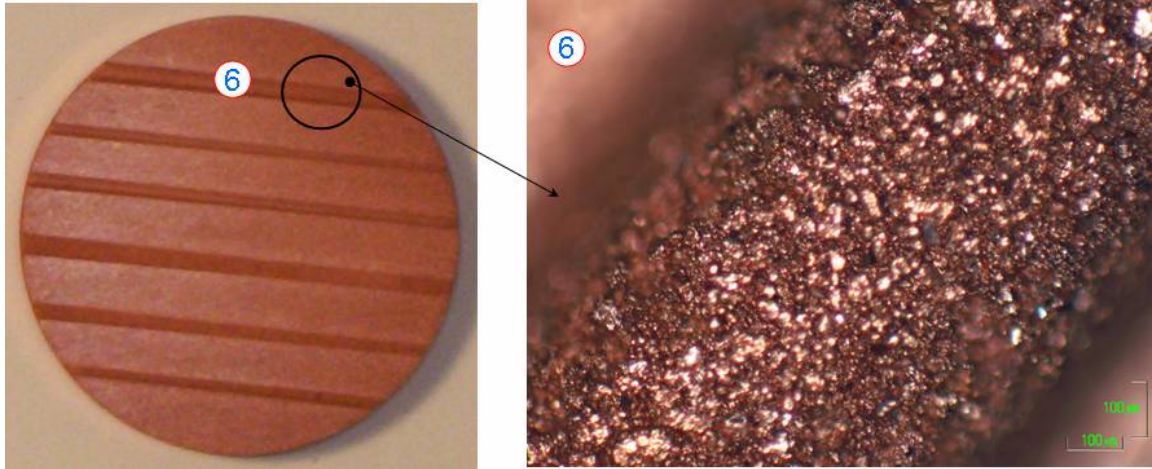
After the shape of the micro-features was obtained via cold compaction, the bonding strength of the green part was further improved by incomplete sintering. A Lindberg/BlueM Furnace (1700, 5000W) was used for sintering. Before the green part

was placed into the furnace, the furnace was first pre-heated to a steady-state target temperature. The sintering time was under 15 minutes to avoid shrinkage.

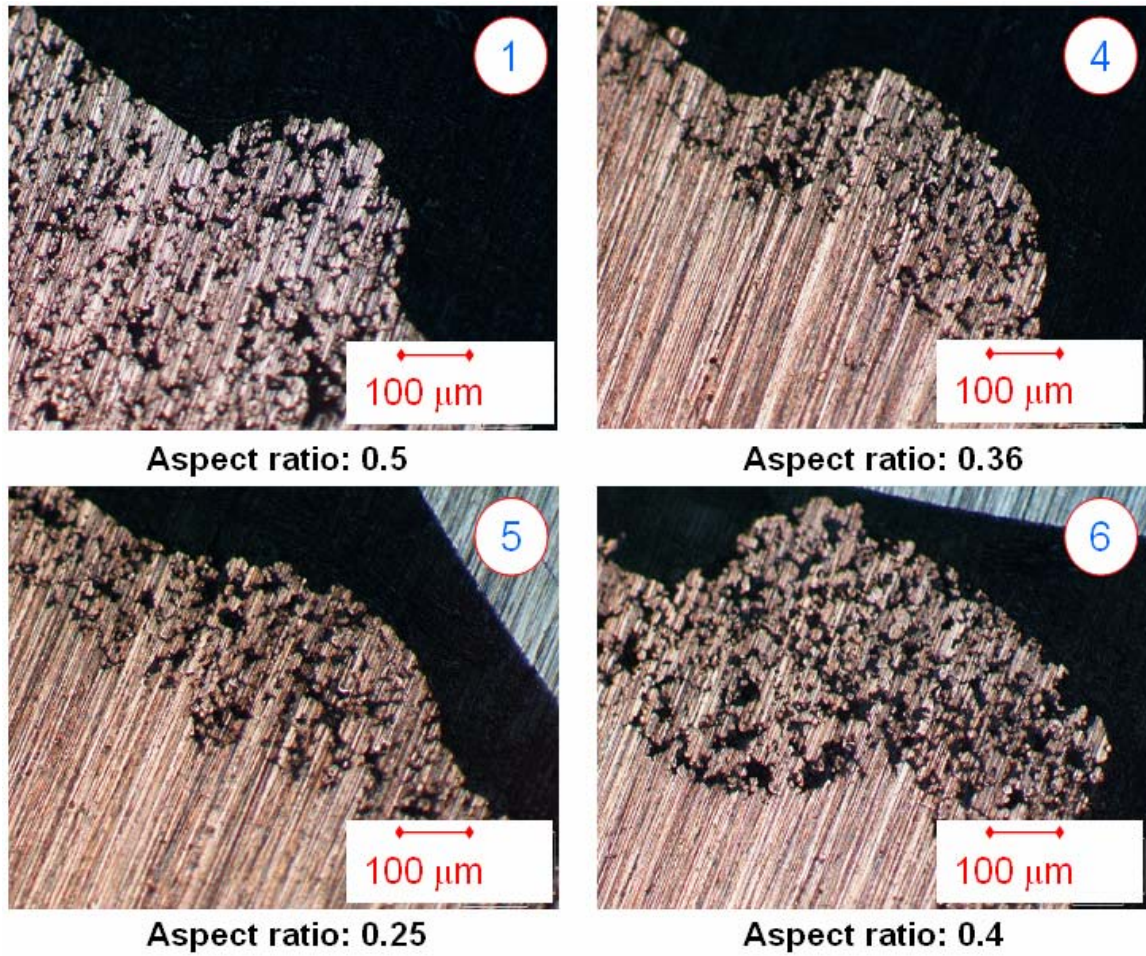
### **2.3.2 Experimental Results and Discussion**

As shown in Figure 2-15, the left-hand side is the powder compact made from this experiment; the right-hand side is the magnified top view of a micro-protrusion on the compact surface. A closer look of each micro-protrusion from the side view is shown in Figure 2-16 (successfully formed micro-features) and Figure 2-17 (unsuccessfully formed micro-features), which indicates that the pores are interconnected. It was observed in the experiment that protrusion number 2 (aspect ratio 0.7) and 3 (aspect ratio 0.8) were not successfully formed due to the fact that their large aspect ratios and the protrusions on the compact were entrapped inside the channel during the ejection. But all the other micro-features (aspect ratio 0.25-0.5) were formed successfully. Therefore it can be concluded that the maximum achievable aspect ratio through cold compaction is around 0.5 in this case. The porosity distribution around the bumps indicates that the protrusion part has a higher porosity (low density) than the base part, which is due to the fact that less compression force was distributed inside the channel and most loads was taken by the flat surface. In other words, the porosity distribution of a compact made by die pressing is affected by the structure of the die/part. In terms of heat transfer efficiency, higher porosity in those micro-protrusions is desired (Liter and Kaviany 2001). Figure 2-18 shows the SEM of the compact surface at two different scales.

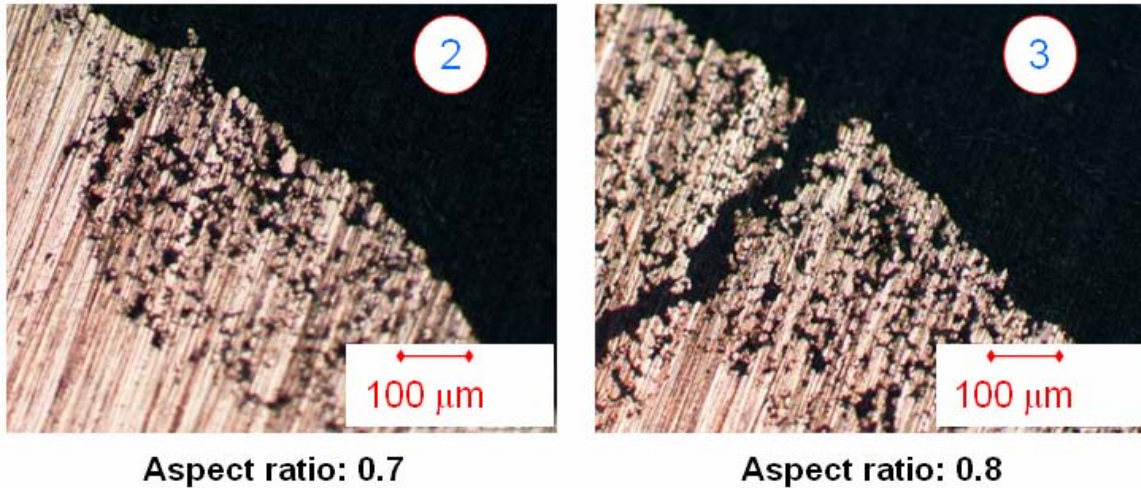




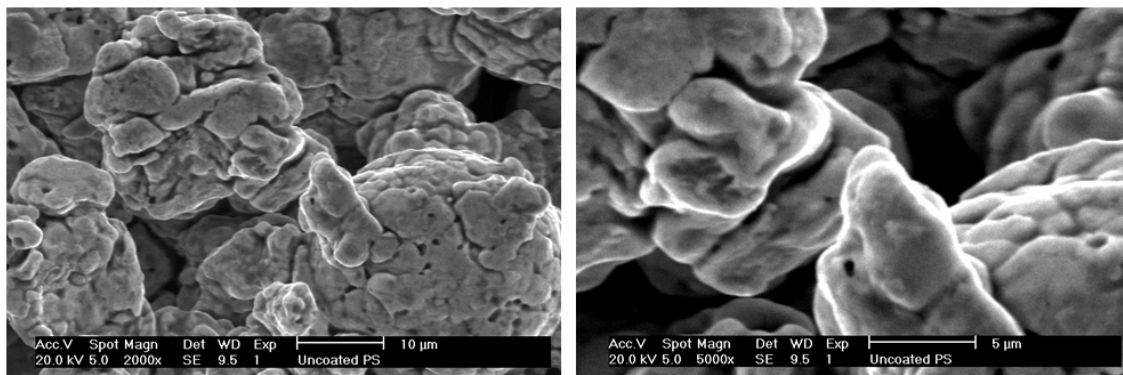
**Figure 2-15 Powder compact with micro-protrusion made from the experiment**



**Figure 2-16 Magnified side view of successfully formed micro-protrusions**



**Figure 2-17 Magnified side view of unsuccessfully formed micro-protrusions**



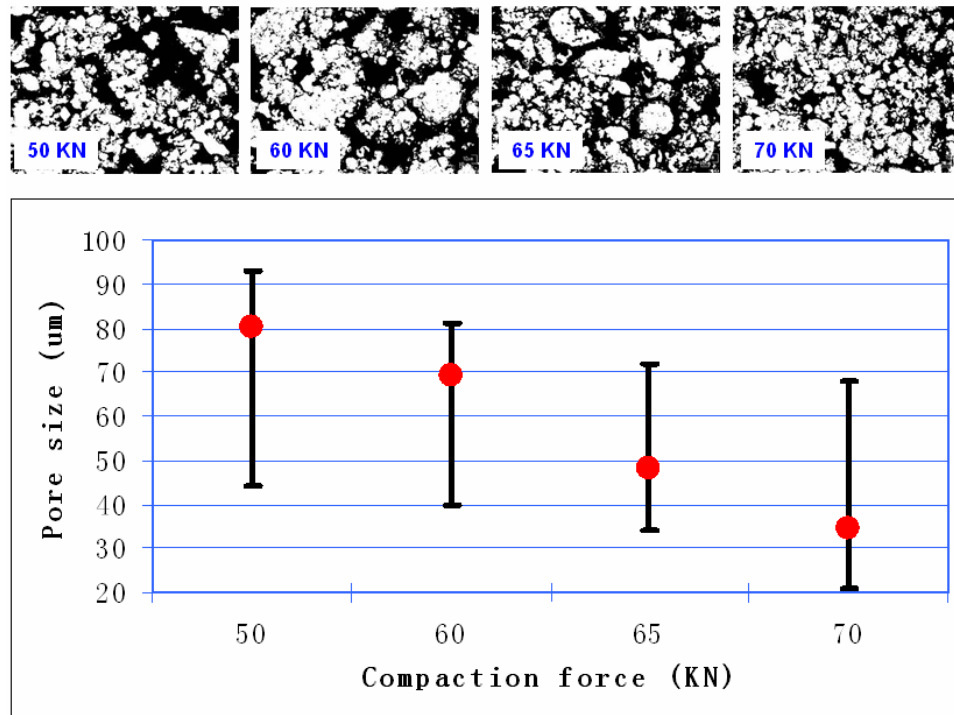
**Figure 2-18 SEM of the compact surface**

### 2.3.2.1 Effect of Compaction Force on the Pore Size

To investigate the effect of compaction on the pore size distribution, different compression forces (50, 60, 65, 70KN) were used to make the same part. By using image processing software (Matrox Inspector), the pore size was measured from the microscopic picture taken from the top surface view of the part. As shown in Figure 2-19, the images are on the top and the pore size distributions are shown in the lower graph. All the pores in the pictures were measured, the dots in the graph are the mean values, and the upper and lower bars indicate the highest and lowest measured values. Obviously, the



mean pore size reduced with the increasing compaction force. ANOVA technique was used to test whether or not the effect of compaction force on the pore size was statistically significant. The obtained statistics are F (7.77) and p-value (0.001), which indicates that the effect of compaction force is significant on the pore size with a confidence level of 99.9%. The scattering range of the pore size distribution did not change much as the compaction force increased.

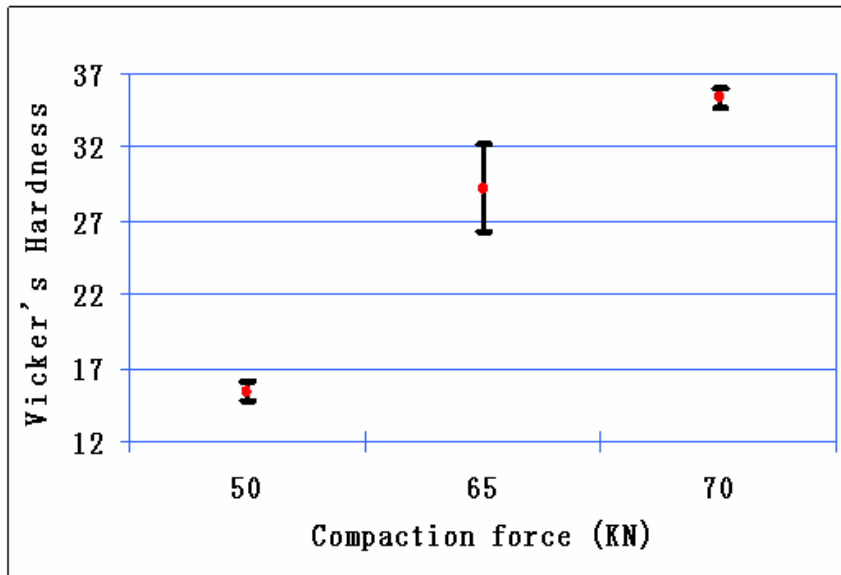


**Figure 2-19 Pore size distribution at different cold compaction force**

### **2.3.2.2 Effects of Compaction Force and Sintering on the Strength of the Formed Micro-features**

Microhardness test was conducted to characterize the mechanical strength of the part. As shown in Figure 2-20, the hardness of the green compact increases as the

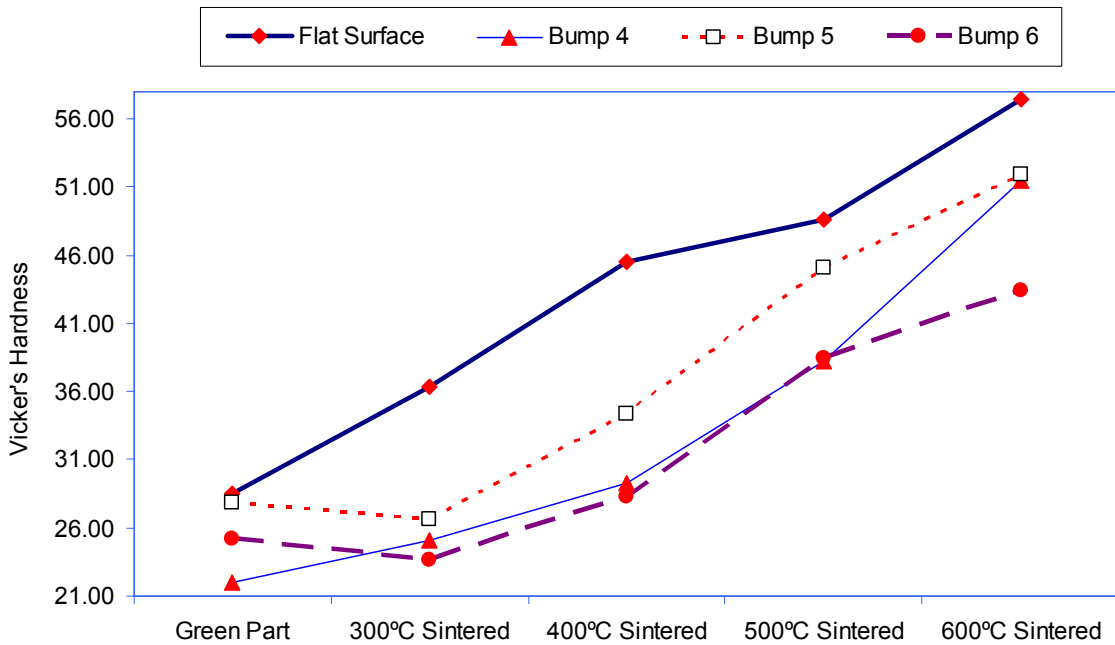
compaction force increases. ANOVA technique was used to test whether or not the effect of compaction force on the hardness is statistically significant; the obtained statistics are F (31.98) and p-value (0.009), which indicates that the effect of compaction force is significant on the micro-protrusion strength with a confidence level of 99.1%. The maximum hardness of the cold compacted part is less than HV40 (Vicker's hardness), which is rather soft. However, our experimental data indicates that sintering at 800°C for 20 minutes help to strengthen a 65 KN compacted part by a factor of 180% (from HV29 to HV 52).



**Figure 2-20 Hardness of the cold compacted part compressed using different force**

To further investigate the effects of sintering temperatures on the strength of the formed micro-features, parts compacted with a force of 70 KN were sintered at 300 °C, 400 °C, 500 °C and 600 °C respectively for 15 minutes. The hardness measurements on them are shown in Figure 2-21 (5 repeated measurements on each location). Although there were some measurement uncertainties, the general trend shows that the sintering

temperature has a strong influence on the mechanical strength of the formed part. As shown in Table 2-1, ANOVA test results further proved that sintering temperature has a significant effect. Comparing to a  $\alpha$ -level of 0.10, most p-values are lower than it, which indicates that the effect of temperature is strong. There are also a few p-values larger than  $\alpha$ , which indicate an insignificant effect. However, those large p-values are mostly corresponding to a small temperature difference (100 °C) or at low sintering temperature. Considering the uncertainties in the experiment and measurement, the general trend shows that sintering temperature has a significant effect on the part strength in the range from 300 °C to 600 °C. Especially, there is a jump in the part strength when the sintering temperature was increased from 200 °C to 450 °C.



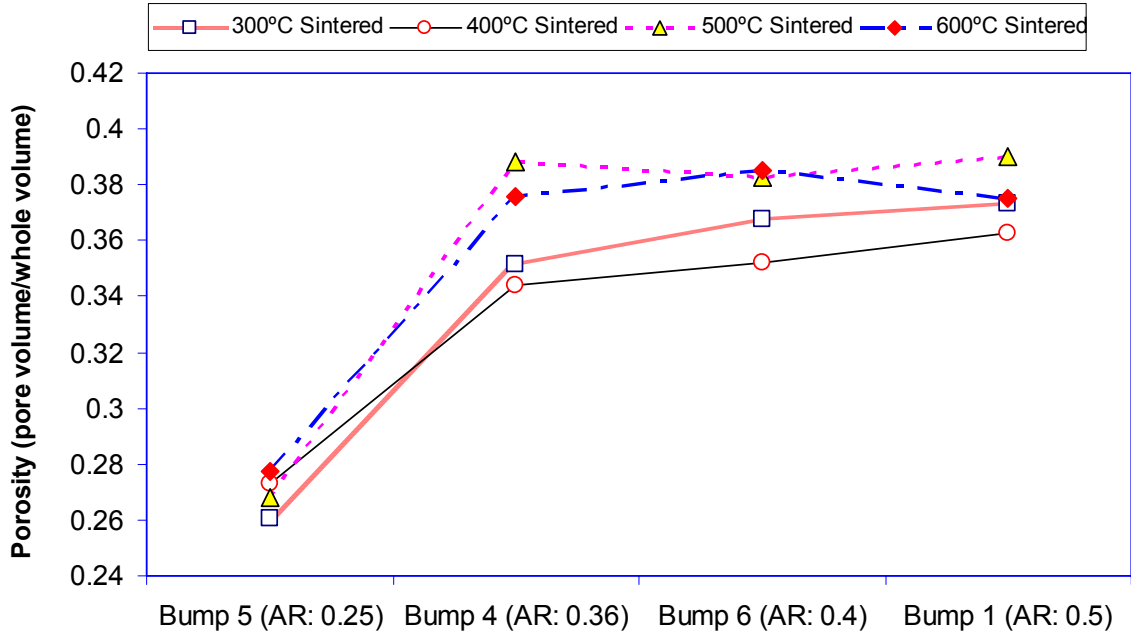
**Figure 2-21 Hardness of part sintered at different temperatures**

	p-value				
	Bump 1	Bump 4	Bump 5	Bump 6	Flat Surface
Green vs 300°C	0.950	0.166	0.664	0.406	0.019
Green vs 400°C	0.295	0.005	0.105	0.214	0.001
Green vs 500°C	0.000	0.000	0.003	0.021	0.000
Green vs 600°C	0.000	0.000	0.000	0.001	0.000
300°C vs 400°C	0.309	0.064	0.050	0.074	0.007
300°C vs 500°C	0.000	0.000	0.001	0.012	0.000
300°C vs 600°C	0.001	0.000	0.000	0.001	0.000
400°C vs 500°C	0.000	0.004	0.033	0.071	0.331
400°C vs 600°C	0.003	0.000	0.001	0.006	0.005
500°C vs 600°C	0.010	0.000	0.116	0.414	0.009

**Table 2-1 F-test to determine the effect of the sintering temperatures on the hardness**

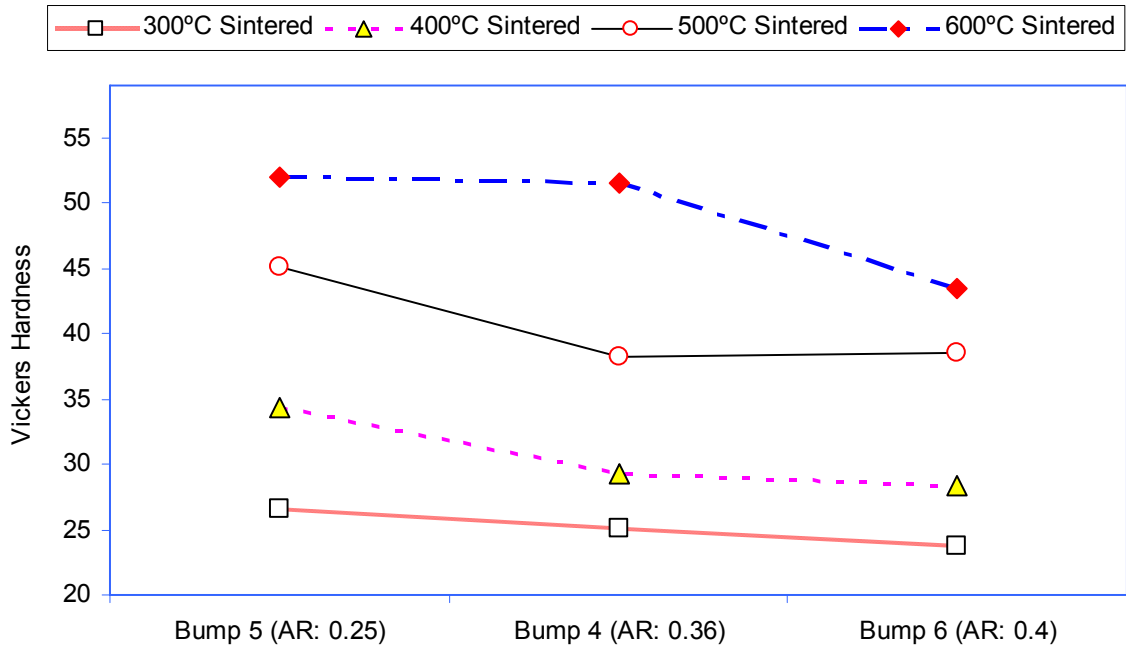
### **2.3.2.3 Effects of Aspect Ratio on the Strength and Porosity of the Formed Micro-features**

Due to the different consolidation force distribution (during compaction) on micro-protrusions with different aspect ratios, the obtained micro-features will have different properties as the aspect ratio varies. To investigate the effect of aspect ratio on the strength and porosity of the formed micro-features, micro-protrusions on above mentioned parts (compacted with a 70 KN force and sintered at 300 °C, 400 °C, 500 °C or 600 °C for 15 minutes) were studied. There are four aspect ratios available for the current tooling: 0.25 (bump 5), 0.36 (bump 4), 0.4 (bump 6) and 0.5 (bump 1).



**Figure 2-22 Porosity of formed micro-features with various aspect ratios**

As shown in Figures 2-22 and 2-23, the porosity and hardness have a similar trend as the aspect ratio varies in all the cases (parts sintered at different temperatures). Five measurements were made on each measured porosity/hardness. Bump 5 has the lowest aspect ratio (0.25), which results in a lower porosity and higher hardness. However, the porosity/hardness differences among other bumps are not very significant.

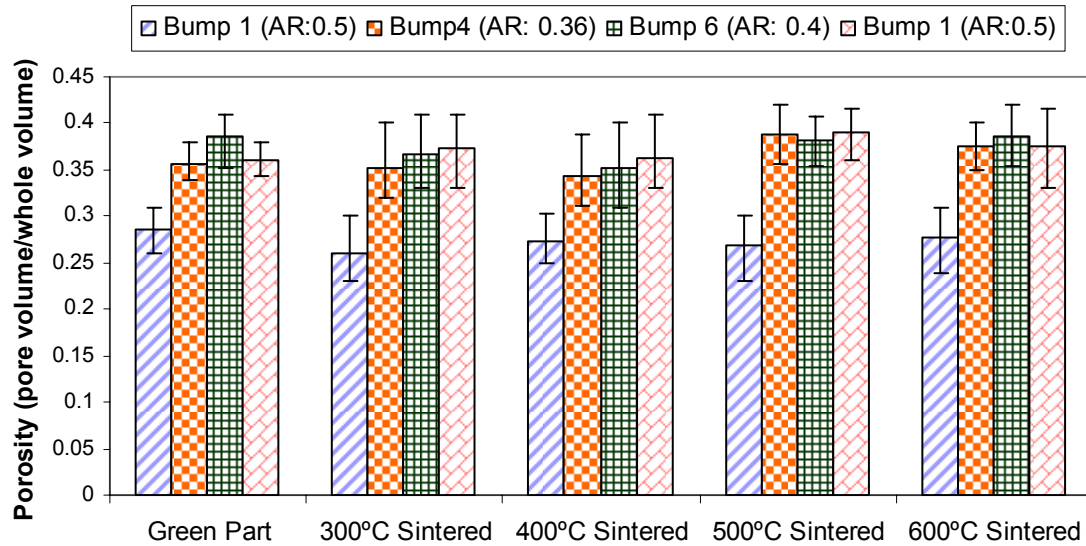


**Figure 2-23 Hardness of formed micro-features with different aspect ratios**

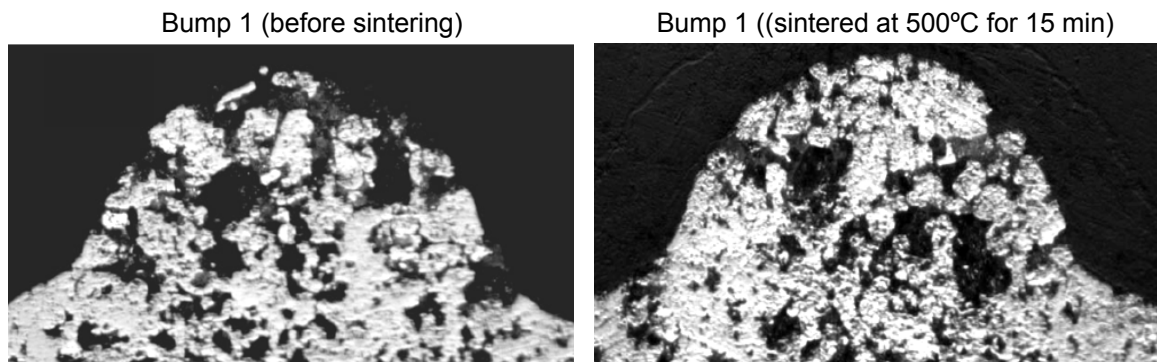
#### 2.3.2.4 Effects of Sintering on the Porosity of the Formed Micro-features

As shown in Figure 2-24, the effect of sintering temperatures on the porosity of the formed micro-features (70KN compacted and sintered for 15 minutes) is not significant as the sintering temperatures varied from 300 °C to 600 °C. And the porosity remained the same as that of the green part, which indicates that the sintering did not proceed to the final stage (fully shrinkage) and the pore structure was maintained. Figure 2-25 shows the cross-sectional views of the bump1 before sintering and after sintered at 500 °C for 15 minutes. Although the pore distributions are not similar due to the fact they are from different cross sections, the overall porosities of the bump are close.





**Figure 2-24 Porosity of formed micro-features sintered at different temperatures**



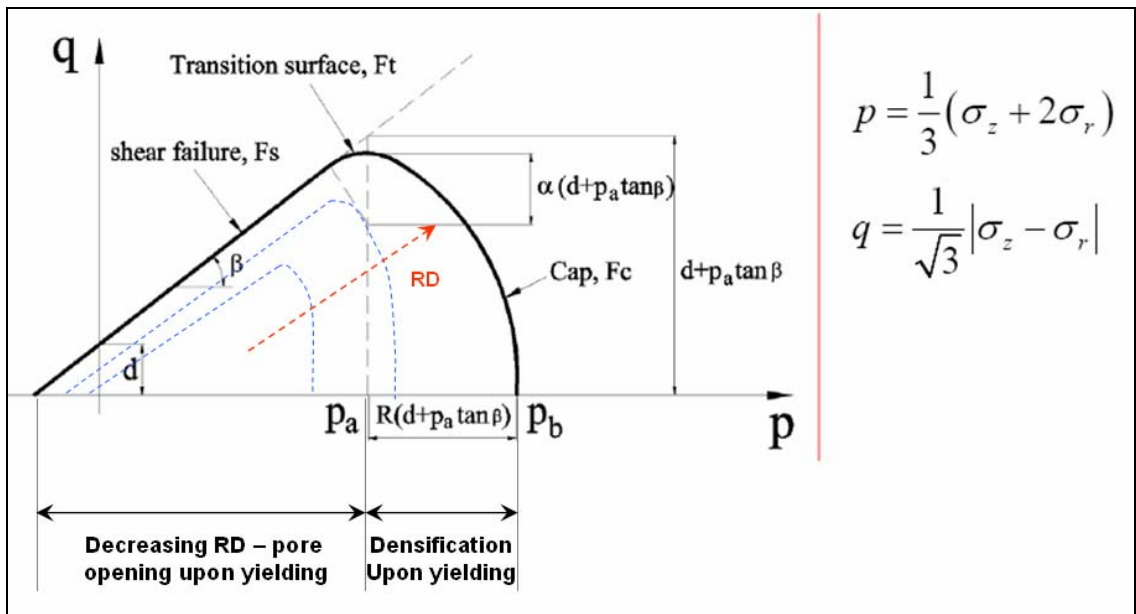
**Figure 2-25 Cross-sectional views of the bump1 before and after sintering**

## 2.4 Cold Compaction Simulation

In order to simulate the cold powder compaction process, a finite element analysis (FEA) model was developed utilizing the material property data from previous studies in literature. With this model, the density distribution of the formed micro-features could be studied.

### 2.4.1 Material Modeling for Compaction Simulation

As briefly introduced in the literature review section, the deformation of powder compacts can be divided broadly into two modes. When the applied stress state is highly confining (such as in the later stages of die compaction), the material densifies if the stresses exceed a certain limit. When the stress field is close to simple shear, the degree of confinement is low and the compact will exhibit shearing failure. These two types of behavior are represented in the form of the yield locus of the modified Drucker-Prager/Cap (DPC) model as shown in Figure 2-26.



**Figure 2-26 The DPC model (PM Modnet Computer Modelling Group 1999)**

In the following subsection, we adopt the DPC model, which is the most accepted model at present in the powder metallurgy and ceramic industries. This is a phenomenological model that has been adapted from soil mechanics. It is popular in compaction modeling because it contains features that are in accordance with the physical

response of particulate compacts (PM Modnet Computer Modelling Group 1999; Drucker et al. 1957).

The DPC model at low hydrostatic pressures is a shear failure model, similar to those used in granular flow, and reflect the dependence of the strength on the confining pressure. It predicts that the strength in tension is smaller than that in compression, a concept that is common for rocks, brittle materials, and pressed powder compacts. In its simplest form, it is represented by a straight line in the  $p$ - $q$  plane, which is also known as the Mohr-Coulomb shear failure line  $F_S$ :

$$F_S(q, p) = q - d - p \times \tan(\beta) = 0 \quad (2-4)$$

The two parameters are termed cohesion ( $d$ ) and internal friction angle ( $\beta$ ). If the stress state is such that the corresponding Mises equivalent stress ( $q$ ) and hydrostatic pressure ( $p$ ) result in a value of  $F(q, p) < 0$ , then the stress causes only elastic deformation. If the stresses are such that Equation 2-4 is satisfied, the material fails in shearing. At high hydrostatic pressures, the yield surface is described by a cap surface  $F_c$ :

$$F_S(q, p) = q - d - p \times \tan(\beta) = 0 \quad (2-5)$$

This form is consistent with the DPC model implemented in the finite element package ABAQUS. The parameters  $p_a$  and  $R$  are obtained from compaction experiments, where  $R$  is a material parameter that controls the shape of the cap, and  $p_a$  is an evolution parameter that represents the volumetric inelastic strain driven hardening/softening which

is related to hydrostatic compression yield stress ( $p_b$ ). The parameter  $\alpha$  does not have a physical meaning but ensures a smooth transition between the cap and the shear failure regions. Typically, a small value ( $\alpha = 0.01-0.05$ ) is used to avoid the situation of  $\alpha = 0$  for which a corner forms at the intersection of  $F_c$  and  $F_s$  which may lead to numerical problems (Hibbit et al. 1994). Because this is simply a numerical trick which affects the efficiency but not the accuracy of the computation, it can also be assumed that  $\alpha = 0$ . The geometric representation of the complete yield locus is represented in the  $p$ - $q$  plane as a limiting curve  $F(q, p, RD) = 0$ , see Figure 2-26.

#### 2.4.2 FEA Validation: a Case Study on Compaction of Zirconia Powder

In order to establish a numerical model for our own problem (micro-scale modulated porous surface), we first performed validation analysis using the existing experimental data and information in the literature. Due to the lack of data for copper, Zirconia powder was used instead of copper for initial validation.

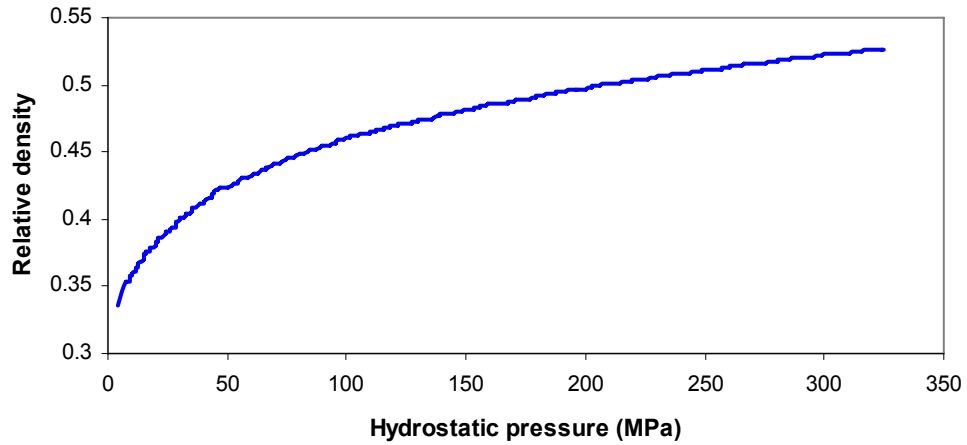
Full density	Initial density	Particle size	$\beta$	$\alpha$
6.08 (g/cm <sup>3</sup> )	1.885 (g/cm <sup>3</sup> )	0.53 $\mu$ m (Nominal)	54.3°	0.03
E	$\nu$	d	R	
206 GPa	0.31	1.53 MPa	0.835	

**Table 2-2 Material properties of zirconia powder (Kim et al. 2000)**

This simulation validation is based on the experimental results of Kim et al. (Kim et al. 2000). The material properties used for the simulation are summarized in Table 2-2. These values were adopted from the experimental work of Kim et al. (3mol% Y<sub>2</sub>O<sub>3</sub>

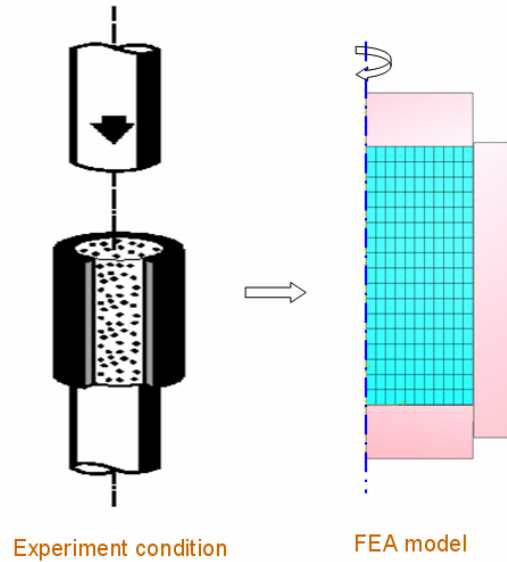
stabilized zirconia powder, HSY-3.0, Daiichi-Kigenso Kagaku Kogyo CO. Ltd., Japan).

Figure 2-27 shows the densification behavior of this powder.



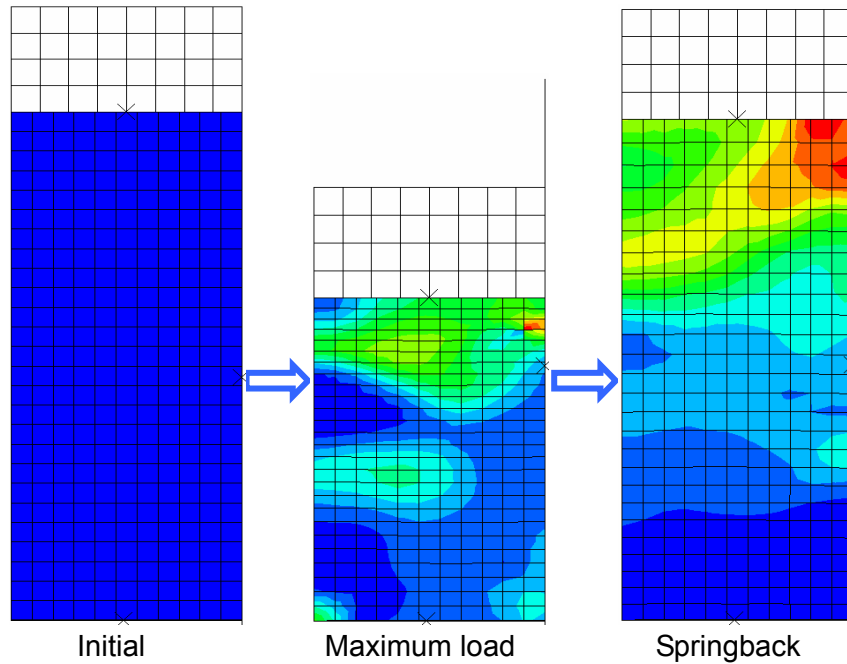
**Figure 2-27 Densification behavior of the zirconia powder (Kim et al. 2000)**

Kim et al. conducted uniaxial die compaction of zirconia powder. The radius of the die is 6.55 mm and the fill height of powder is 15.74 mm. An axial pressure of 100 MPa was applied to compact the powder. After the powder was ejected from the die, the density distribution of the compact was measured using Vicker's hardness test by assuming a given relationship between density and hardness.



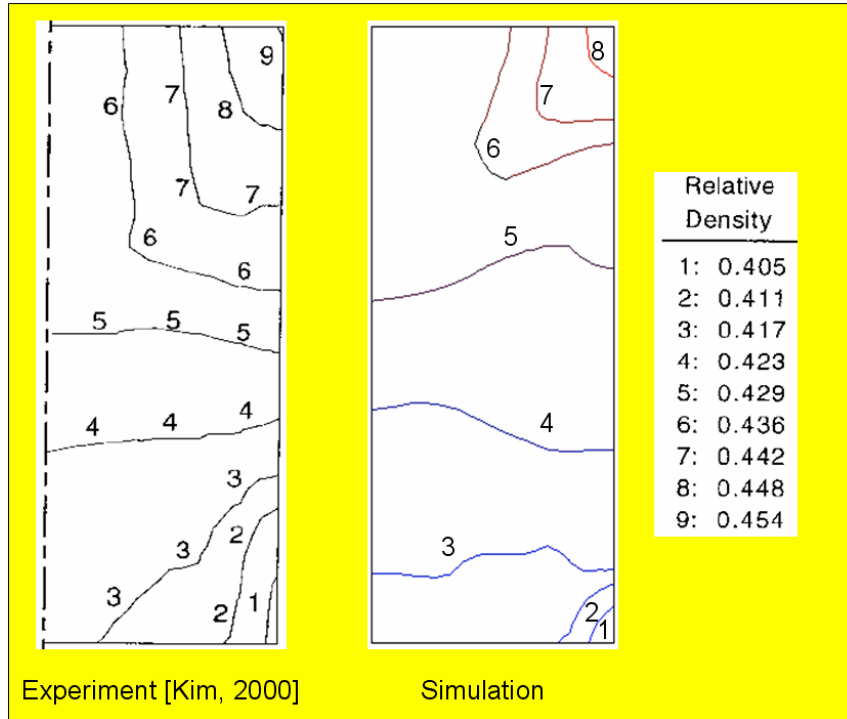
**Figure 2-28 Illustration of the FEA model**

Considering the geometric symmetry of the process, only an axisymmetric section of the compact was simulated using the commercial FEA software ABAQUS v6.5 (Figure 2-28). The tooling was represented as rigid elements, whereas the material mesh for the powder was comprised of an array of  $26 \times 11$  4-node bilinear axisymmetric quadrilateral element with reduced integration (CAX4R). The powder was modeled as an elastic-plastic material with linear elasticity, using the modified Drucker-Prager/Cap model for the plasticity. Figure 2-29 is an illustration of the simulation process.



**Figure 2-29 Die compaction process**

A comparison of the relative density ( $RD = \text{local density} / \text{full density}$ ) distribution obtained from the simulation and Kim's experiment is presented in Figure 2-30. It was observed that the relative density was the highest at the corner of the contact surface between the upper punch and the die wall, and the lowest at the corner of contact surface between the lower punch and the die wall, which is caused by the friction effect imposed by the die wall. The overall density distribution trend predicted by simulation agreed well with that of experiment, though it was underestimated.

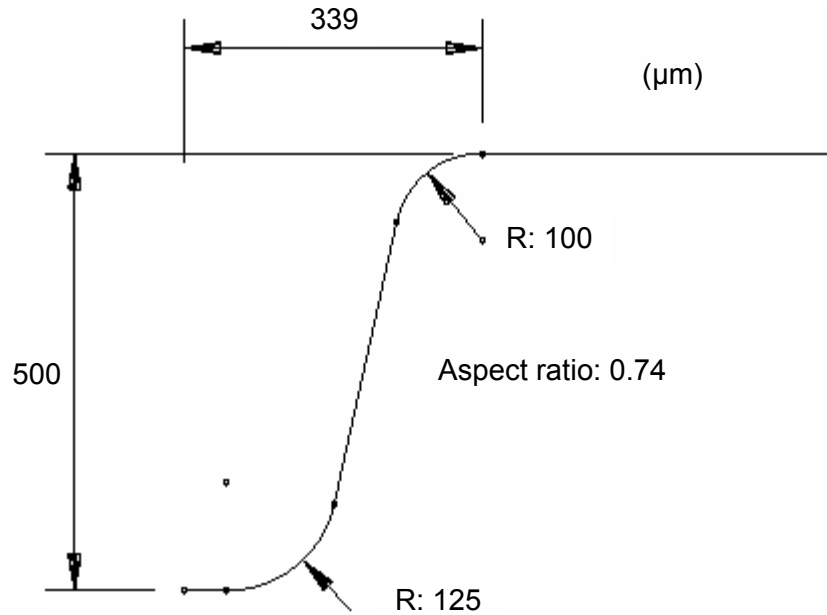


**Figure 2-30 Simulation validation (relative density distribution)**

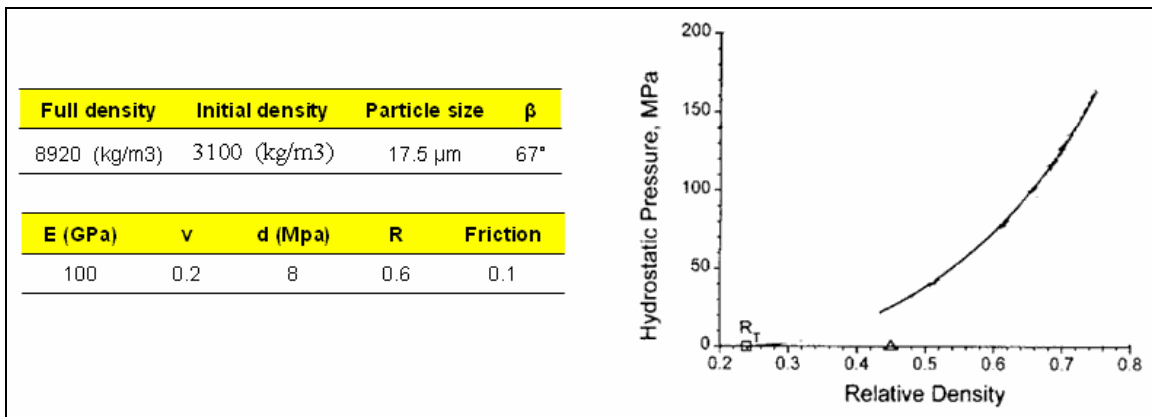
### 2.4.3 FEA Modeling: Compaction of Copper Powder into Micro-features

In this case study, copper powders were pressed in a die to form a micro-bump as shown in Figure 2-31 (symmetric view). The FEA procedure used in the previous section was employed. The tooling was represented as rigid elements, whereas the material mesh for the powder was comprised of 486 elements (CPE4R: 4-node bilinear plane strain quadrilateral with reduced integration). The powder used in this case study was electrolytic copper powder. Since there is no available material property data, the DPC inputs (Figure 2-32) in the ABAQUS were collected from the following references: (Martin et al. 2002; Park et al. 1999; Vyal and Laptev 2002).





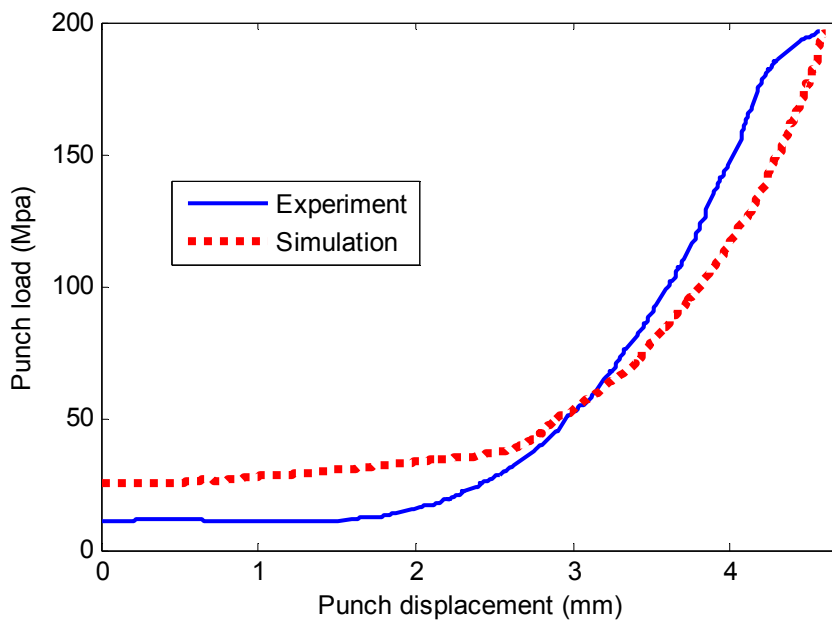
**Figure 2-31 Geometry and dimension of the die (symmetric view)**



**Figure 2-32 Material properties used in ABAQUS (Martin et al. 2002; Park et al. 1999; Vyal and Laptev 2002)**

As shown in Figure 2-33, the loading curve obtained from experiment (Figure 2-14) is compared with the loading curve from the simulation. In general, the simulation results agree well with the experiment. The overestimation of the load at the initial loading stage is mostly likely due to inaccuracy of the material modeling at low densities, which is very common in compaction since the material testing at low density is very

difficult. The punch load in the experiment starts to flatten out at the end, which is caused by the maximum loading pressure setting (around 65 Mpa) used in the hydraulic pressure device. Therefore, the corresponding portion of the loading curve is not a true representation of the material response, which explains the difference between simulation and experiment in the final stage.



**Figure 2-33 Compaction simulation validation**

The shape and density of the powder compact before and after compaction are shown in Figure 2-34. Due to the non-uniform pressure inside the die, the density of the lower tip (micro-bump) is relatively low when compared to the other part of the compact. The highest density occurs around the lower corner of the protrusion.



1. Porous micro-protrusions were successfully formed using uniaxial compaction and incomplete sintering processes in the current experiments. Existing equipment (press and furnace) can be directly used for this process without additional devices.
2. In this specific case, maximum achievable aspect ratio through cold compaction is around 0.5.
3. A higher compaction force can significantly improve the mechanical strength of the formed micro-features and reduce the nominal pore size, but doesn't have a significant effect on the variation of the pore size distribution.
4. Sintering at 500-800°C for 15-20 minutes can significantly increase the strength of the compacted part, while the interconnected pore structure can be maintained. In other words, sintering is limited to initial stage (surface transport) under this setting.
5. A lower aspect ratio would result in a higher strength and lower porosity.
6. The density of the lower tip of the micro-protrusion is relatively low when compared to the other part of the compact. The highest density occurs around the bump corner.

## **CHAPTER 3**

### **FORMING OF POROUS MICRO-FEATURES AND PARTICLES/SUBSTRATE BONDING USING HOT COMPACTION**

#### **3.1 Introduction**

As investigated in the previous chapter, the achievable aspect ratio using cold compaction and incomplete sintering technique is rather low (about 0.5). To obtain micro-features with a higher aspect ratio, it is essential to ensure a better particle bonding strength during the shaping stage, which could be achieved by employing hot powder compaction processes. By introducing heat during the shaping stage, a good diffusion bonding among particles could be achieved (Chen et al. 2007).

More importantly, the diffusion mechanism of atoms during hot compaction is also different from that of the traditional sintering, which further enhances the bonding of particles. In traditional sintering, the diffusion is purely induced by heat. On the other hand, during hot compaction processes, the diffusion is enhanced by the pressure-induced diffusion (German 1996). Therefore, with two diffusion mechanisms occurring at the same time, parts made of hot compaction usually have a better mechanical strength than those made of traditional sintering if the temperature conditions are the same. On the other hand, most studies on the hot compaction process focus on the forming of non-

porous product (full density). Therefore, more efforts on the investigations of porous features forming using hot compaction are needed.

In this section, a hot compaction experimental system is developed that is capable of performing high temperature operation (700 °C), quick heat-up, and avoiding oxidation. 3D thermal simulation of the experimental setup was conducted to investigate the heat transfer performance and internal temperature distribution, which was then used as a reference for the experiment. Hot compaction experiments were carried out, and the effects of compression force and temperature on the quality in terms of powder consolidation strength and porosity were investigated. In addition, the achievable aspect ratio and taper angle were also discussed.

Besides the forming of porous micro-features, it is also required that the porous layer being coated onto a solid substrate. With hot pressing technique, zero thermal-resistant bonding could be achieved. Hot pressing experiments were conducted to bond particles onto a copper substrate. The bonding strength was tested with two different techniques.

### **3.2 Literature Review**

Hot compaction processes combine the simultaneous application of pressure and temperature, which is also termed as pressure assisted sintering. The four most popular forms of hot consolidation that have been commercially successful are hot pressing, hot isostatic pressing (HIP), forging and hot extrusion. Figure 3-1 depicts the basic schematic diagram of these four processes (German 1994). Numerous other techniques have evolved from these four conventional techniques. Bose summarized these new hybrid

techniques as quick HIP (Q-HIP), isostatic high rate pressing (ISP), CERA-CON & Electroconsolidation, rapid omnidirectional compaction (ROC), plasma activated sintering (PAS), dynamic magnetic consolidation (DMC) and consolidation by atmospheric pressure (CAP) (Bose 1996).

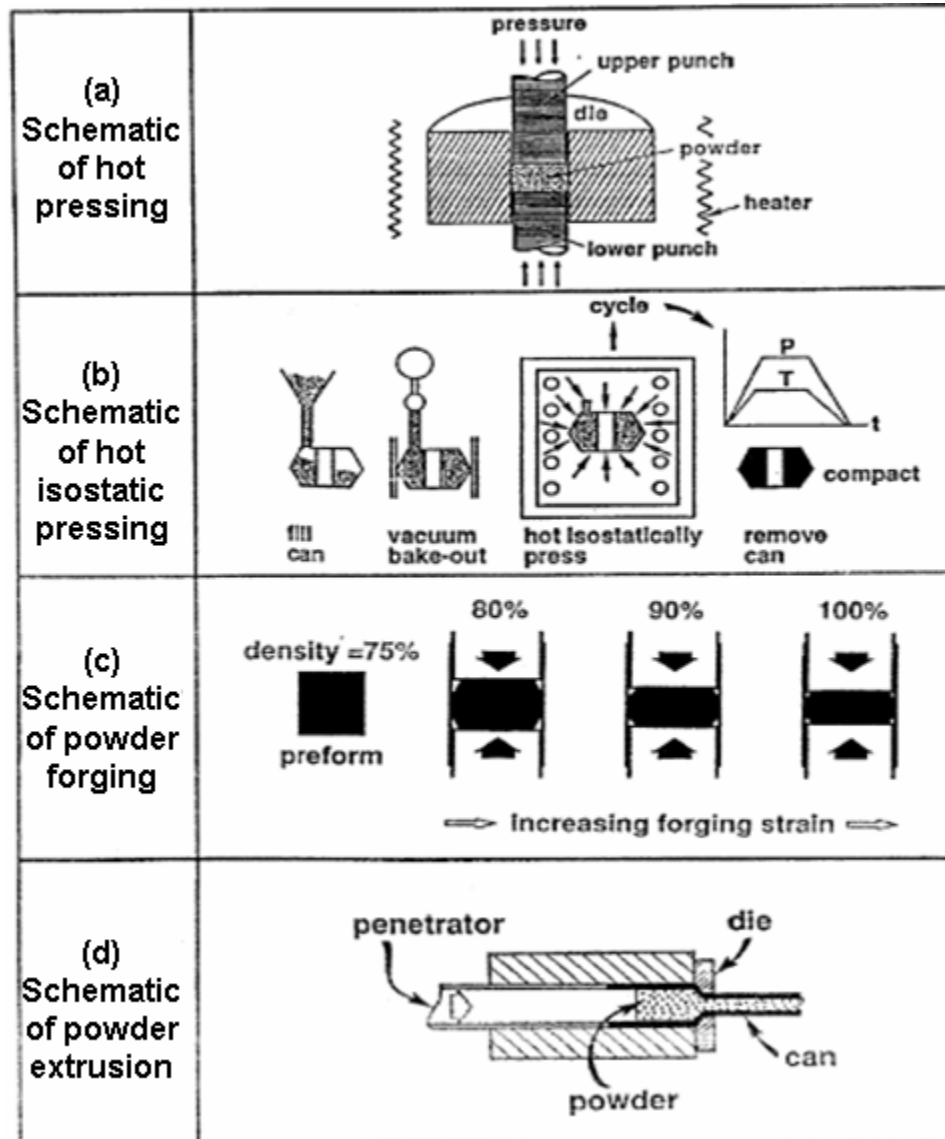


Figure 3-1 Schematic of four conventional hot consolidation processes (German 1996)

Considering that hot die compaction will be used in this study, hot pressing and powder forging are discussed here in details. The detailed description of other hot consolidation processes can be found in (Bose 1996).

### **3.2.1 Uni-axial/uni-directional hot pressing (hot die compaction)**

This is the simplest form of hot consolidation process that is extensively used to densify materials at high temperatures. In its simplest form, the process of hot pressing consists of loading loose powders of the material to be consolidated into a graphite die. The die is usually of a simple cross-section. The graphite die is generally lined with a non-reactive carbonaceous material to reduce reaction between the powder material and the die. Other die materials used are refractory metals and alloys, and some ceramics. The pressure applied is uni-axial in nature and is applied to the punches through a ram. The temperature capability of this process is very high and can be in the range of 2373K. The pressure is usually on the low side, and is limited by the strength of the graphite. Typically, pressures used are in the range of 25 to 40 MPa. The schematic of the process is shown in Figure 3-1a. Although the pressure applied is uni-axial, the die wall constraint creates a radial pressure. Thus, a small amount of shear is imparted to the powder particles in this process. Hot pressing is generally carried out in vacuum though a protective gas such as argon, helium, or nitrogen has also been used.

Hot pressing is extensively used in processing high temperature materials, exotic material compositions, and a variety of different composites with reinforcing agents in the form of particulates, platelets, whiskers, and fibers. Some of the commercial applications include metal-bonded diamond cutting tools, sputtering targets and Tic-Fe composites.



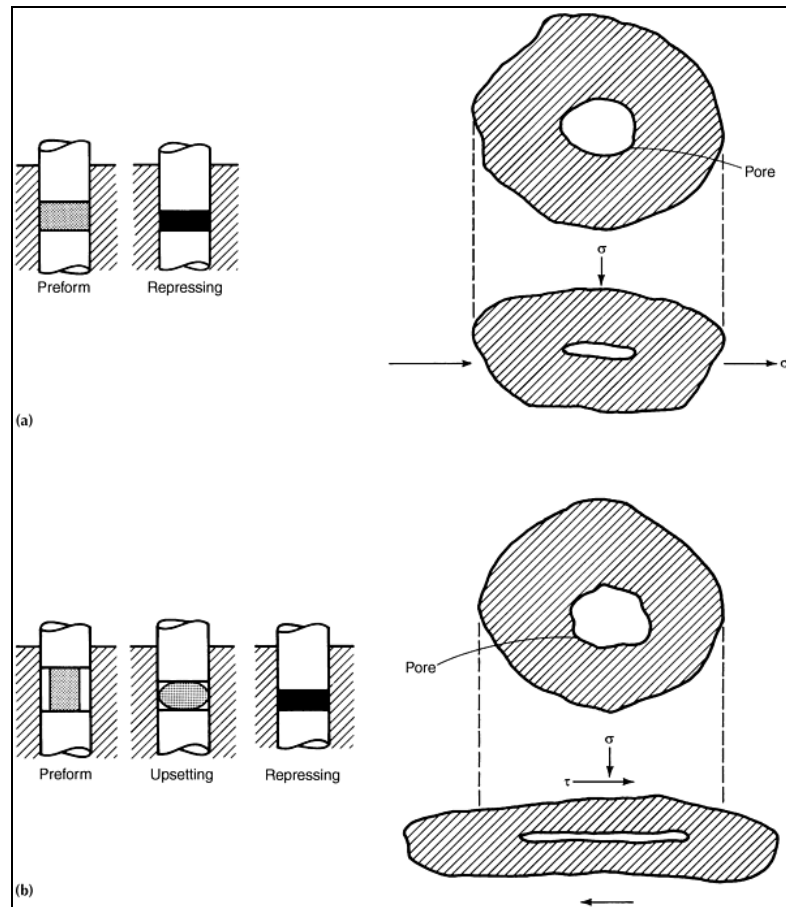
### **3.2.2 Powder forging (P/F, P/M forging, P/M hot forming)**

This is a process in which un-sintered, pre-sintered, or sintered powder metal preforms are hot formed in confined dies. When the preform has been sintered, the process is often referred to as “sinter forging.” The modern era of powder forging was rekindled around the middle of this century when various components such as water pump gears, materials for nuclear power generation, feed pawl for antiaircraft guns, etc., were processed by powder forging.

Powder forging is a natural extension of the conventional press and sinter process, which has long been recognized as an effective technology for producing a great variety of parts to net or near-net shape. In essence, a porous preform is densified by hot forging with a single blow. Forging is carried out in heated, totally enclosed dies, and virtually no flash is generated. This contrasts with the forging of wrought steels, in which multiple blows are often necessary to form a forging from bar stock and considerable material is wasted in the form of flash. The recent successful application of this process includes net-shape formed connecting rod, gear and other precision components (James 1994). There are two basic forms of powder forging:

- Hot upsetting, in which the preform experiences a significant amount of lateral material flow;
- Hot re-pressing, where material flow during densification is mainly in the direction of pressing. This form of densification is sometimes referred to as hot re-striking, or hot coining.

These two deformation modes and the stress conditions they impose on pores are illustrated in Figure 3-2. More extensive explanation of powder forging can be found in (James 1994).



**Figure 3-2 Forging modes and stress conditions on pores for: a) re-pressing; b) upsetting (James 1994)**

### **3.3 Forming of Porous Micro-features Using Hot Compaction**

Experimental investigation of porous micro/meso-feature formation by hot powder pressing has been performed to demonstrate the capability of the proposed manufacturing method. A low cost hot compaction system was designed and fabricated,

which could be conveniently integrated into the existing cold pressing equipment. The forming of porous micro-features with high aspect ratio was studied. Important process variables were identified and evaluated.

### **3.3.1 Experimental Setup and Procedures**

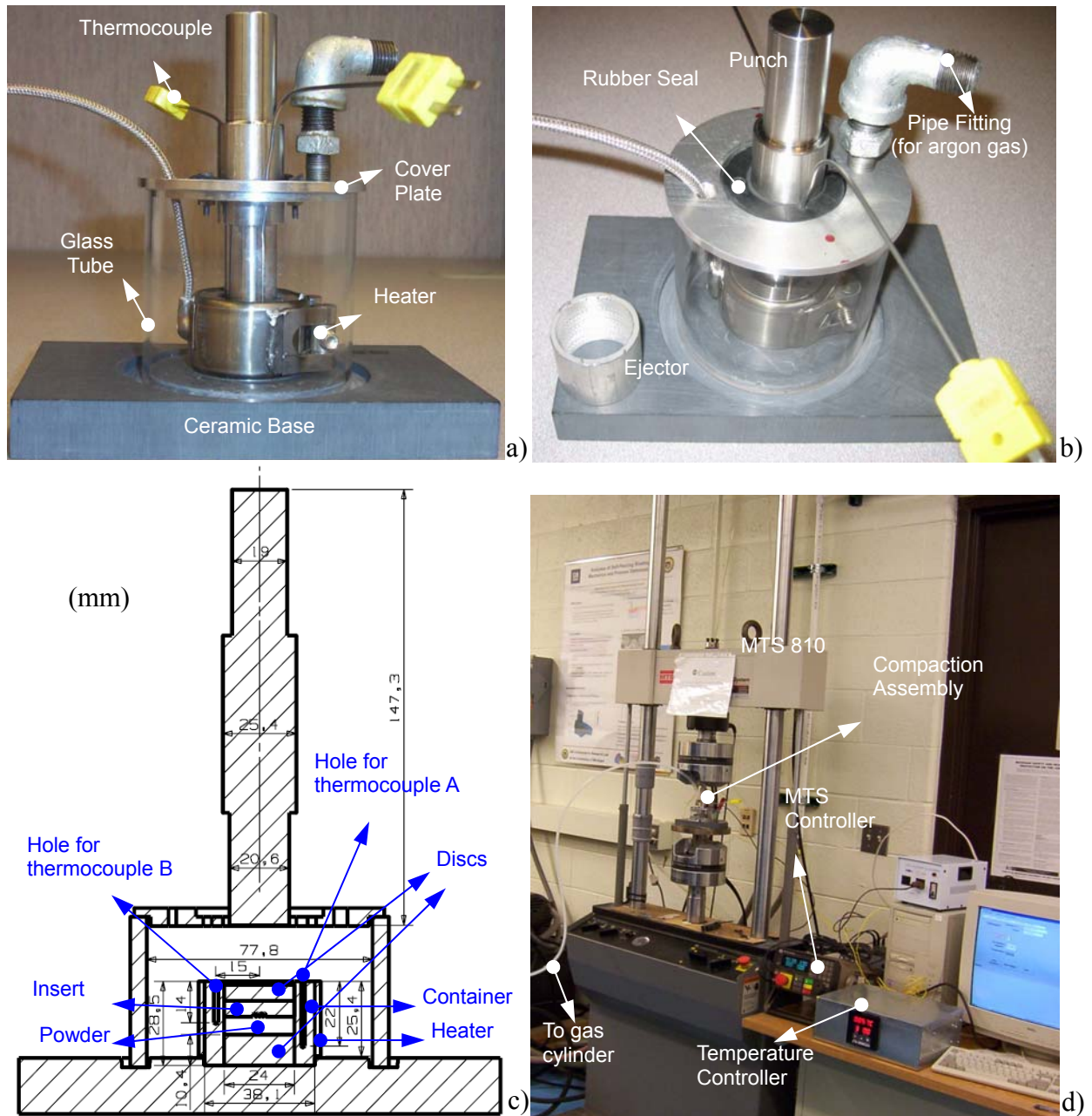
To select a proper material for tooling components, a few common tool materials were compared in terms of their mechanical strength, thermal properties, durability and cost. As summarized in Table 3-1, Tungsten Carbide is excellent in all aspects. However, its cost is very high and also it is difficult to machine. Graphite has good thermal properties, but its mechanical strength and durability are low. Conventional tool steels (A2, D2 and H13) have high mechanical strength, but their maximum service temperature is the lowest. Stainless steels stand out to be the best candidate due to their excellent durability, low cost and good balance between mechanical strength and thermal properties. Thus, we selected Stainless steel 316 as our tooling material. All material properties in Table 3-1 were obtained from a commercial software called CES Selector.

	Price (\$/kg)	Coefficient of thermal expansion (m/m/°C)	Conductivity (W/m <sup>2</sup> /K)	Yield strength (Mpa)	Max. service temperature (°C)	Durability (Oxidation at 500°C)	Hardness (HV)	Melting temperature (°C)
Graphite	11.2 - 17	$0.6-4.3 * 10^{-4}$	24-116	25-55	1300-2690	Average	20	3650
A2 tool steel	4.8 - 7	$13 * 10^{-4}$	26	1800	561-594	Good	700	1423
D2 tool steel	2.7 - 6	$10.3-12 * 10^{-4}$	29.3-31	1864	561-594	Good	610	1430
H13 tool steel	2.4 - 3.6	$10.2-10.7 * 10^{-4}$	27.5 - 29.8	1609 - 1691	561 - 594	Good	480	1460 - 1500
Tungsten Carbide	83 - 124	$5.8 - 6.1 * 10^{-4}$	48 - 52	1404@1000°C	600 - 630	Very good	1500	2800 - 2870
Stainless steel 304	2.6 - 3.1	$16 - 18^{-4}$	14-17	205-310	750-925	Very good	170-210	1450
Stainless steel 310	5 - 5.7	$16 * 10^{-4}$	14.2	275	1150	Very good	160-225	1450
Stainless steel 316	4.9 - 5.4	$15 - 18 * 10^{-4}$	13 - 17	205 - 310	750 - 925	Very good	190-220	1375 - 1400
Stainless steel 430	1.4 - 1.8	$10 - 11 * 10^{-4}$	23 - 27	205 - 370	750 - 870	Very good	150-195	1425 - 1510
Stainless steel 442	1.5-1.9	$9 - 12 * 10^{-4}$	23 - 27	205 - 370	920 - 1025	Very good	190-225	1425 - 1530
Stainless steel 440A	1.9 - 2.3	$9 - 11 * 10^{-4}$	23 - 27	370 - 460	700 - 800	Very good	190-250	1370 - 1480

Table 3-1 Tool materials properties (CES Selector)

As described in the previous Chapter (Figure 2-13), the copper powder used was Grade 185E from ACuPowder Company. The setup for the hot compaction experiment is shown in Figure 3-3. The basic assembly includes a punch, a container, two discs, and an insert. The function of the discs is to avoid direct contact of the powder and insert with other components so that the internal temperature is maintained during compaction. Basic assembly components were made from Stainless Steel 316. The punch was gripped by the upper fixture of the MTS machine. And it is automatically forced to be perpendicular to the ceramic plate. Therefore, the surfaces of the components inside the container need to be parallel to the ceramic plate to ensure a vertical pressure. Hence, the surfaces of the discs and the insert were precision ground to half micron accuracy. The temperature of the system was measured at two locations (two thermocouple holes in the container). A mineral insulated band heater (WATLOW, 400W) was wrapped around the container to supply heat.

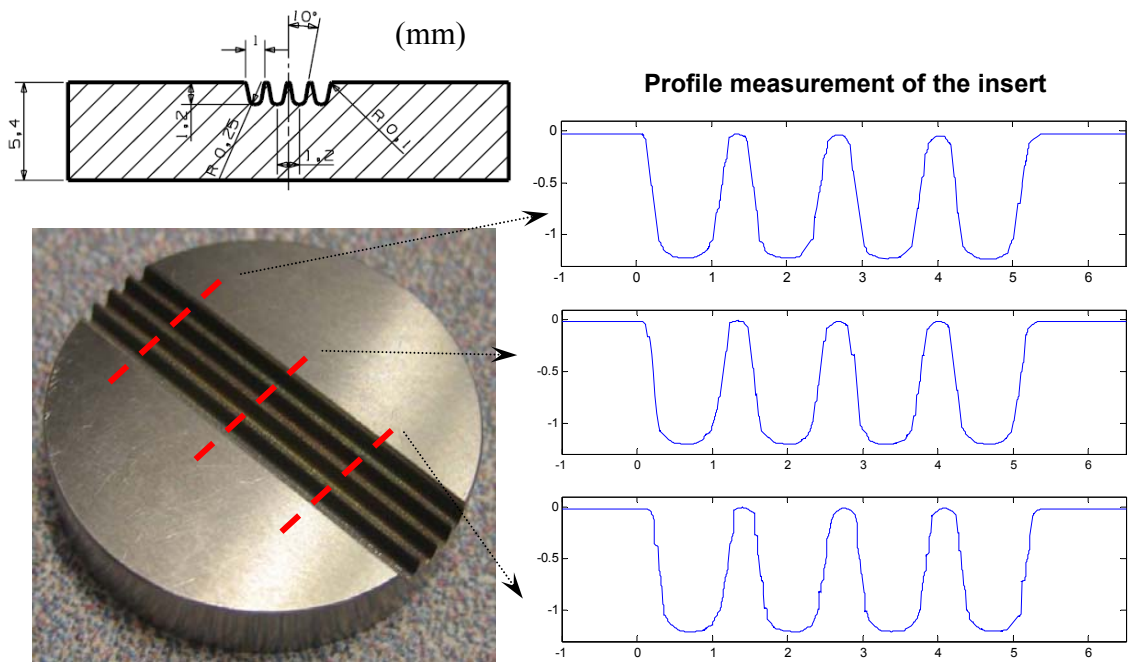
Below the basic assembly, a ceramic plate (902 machinable Alumina silicate, CONTRONICS CORP.) was used to insulate the system from the compression testing system (MTS 810). Together with the ceramic base and the cover plate, the glass tube (Borosilicate Glass) provides an inert environment, which helps to further reduce heat loss and oxidation. Argon gas was continuously supplied into the system during the experiment to minimize the oxidation. As shown in Figures 3-3a and 3-3c, a circular slot was milled on the ceramic plate. The clearance between the inner diameter of the glass tube and the outer diameter of the circular protrusion on the ceramic plate is small, which seals the bottom of the chamber. A rubber seal was used on top of the cover plate to close the clearance between the cover plate and the punch.



**Figure 3-3 Experimental setup: a) compaction assembly (front view); b) compaction assembly (top view); c) compaction assembly (section view); d) whole setup**

Type K thermocouples were used to measure the temperature of the system, which were placed inside the container (thermocouples A and B, see Figure 3-3c). The temperature from thermocouple B was used as the feedback signal to the temperature

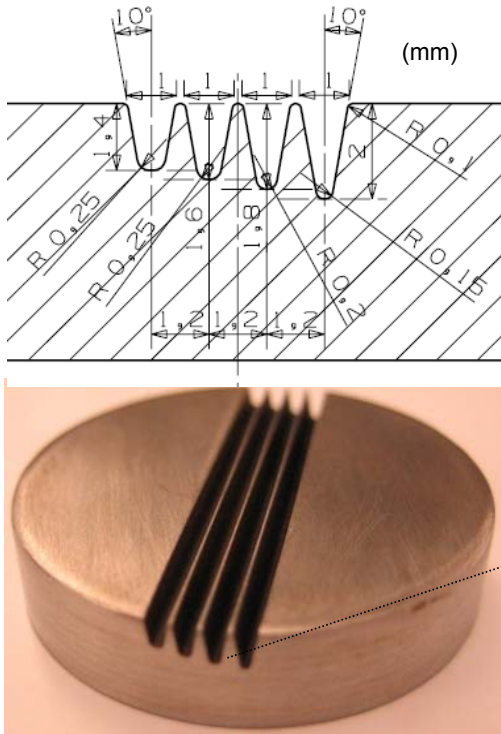
controller (Omega CN616).



**Figure 3-4 Die insert #1 and profile measurement of the micro-channels at different cross sections**

Three inserts with different channel geometries were fabricated using electrical discharge machining (EDM). The EDM parameters were closely controlled to obtain a good surface finish (typically around  $1 \mu\text{m Ra}$ ), which is much smaller than the particle size. A closer look of insert #1 is shown in Figure 3-4. The aspect ratio of the channels is 1.2 (height/width), and the gap between the channels is  $200 \mu\text{m}$ . The profiles of micro-channels were measured using a laser inspection machine at three different cross sections. The measurements (Figure 3-4) indicated that the channel dimension was quite consistent at different sections. As shown in Figure 3-5, insert #2 has four channels with different aspect ratios: 1.4, 1.6, 1.8 and 2.0. In the case of insert #3 (Figure 3-6), the aspect ratio was fixed at 1.5 and the taper angle of the four channels varied from  $0^\circ$  to  $8^\circ$ .





Aspect ratio: 1.4, 1.6, 1.8, 2.0

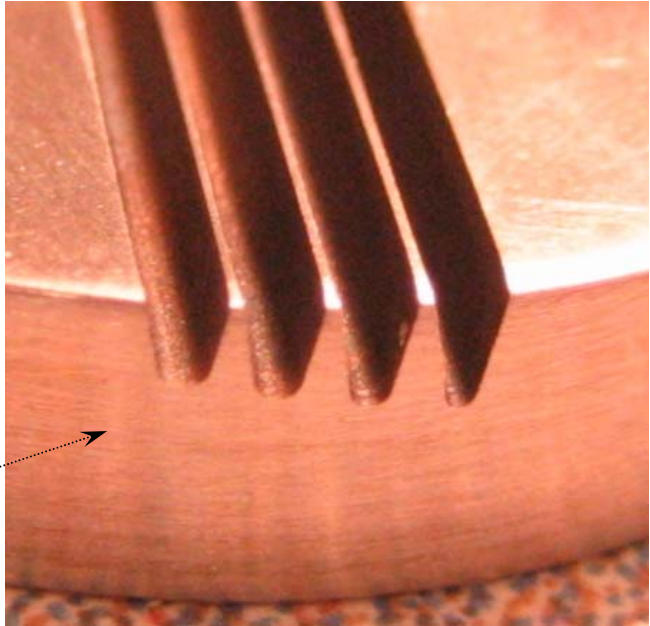
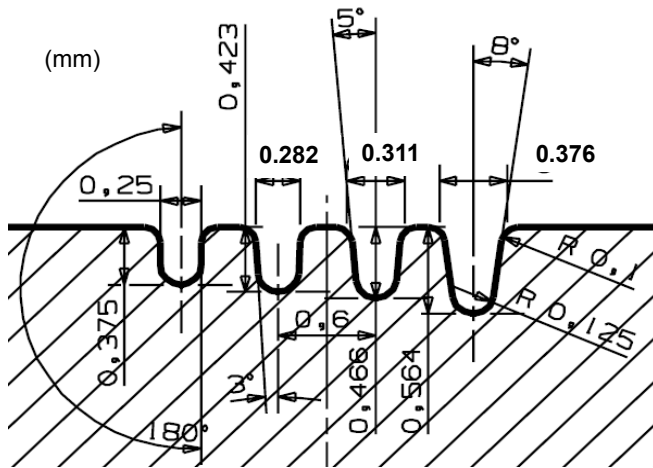


Figure 3-5 Die insert #2



Aspect ratio: 1.5

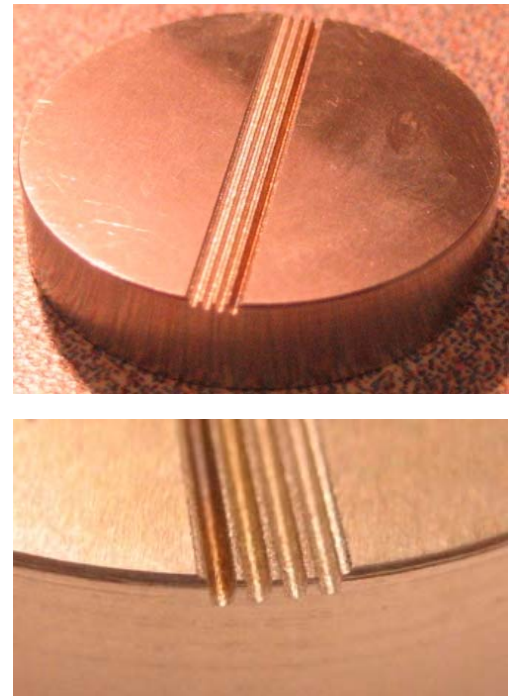
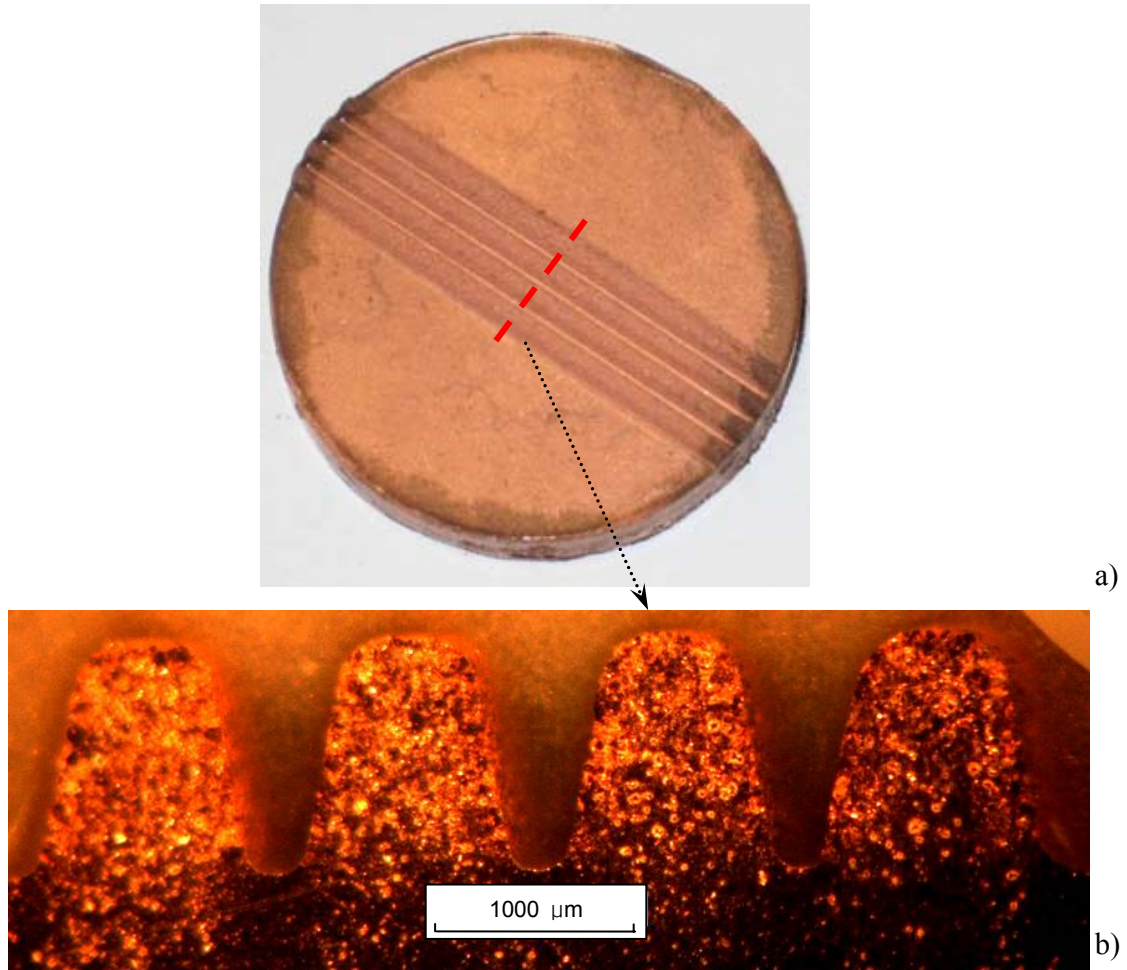


Figure 3-6 Die insert #3



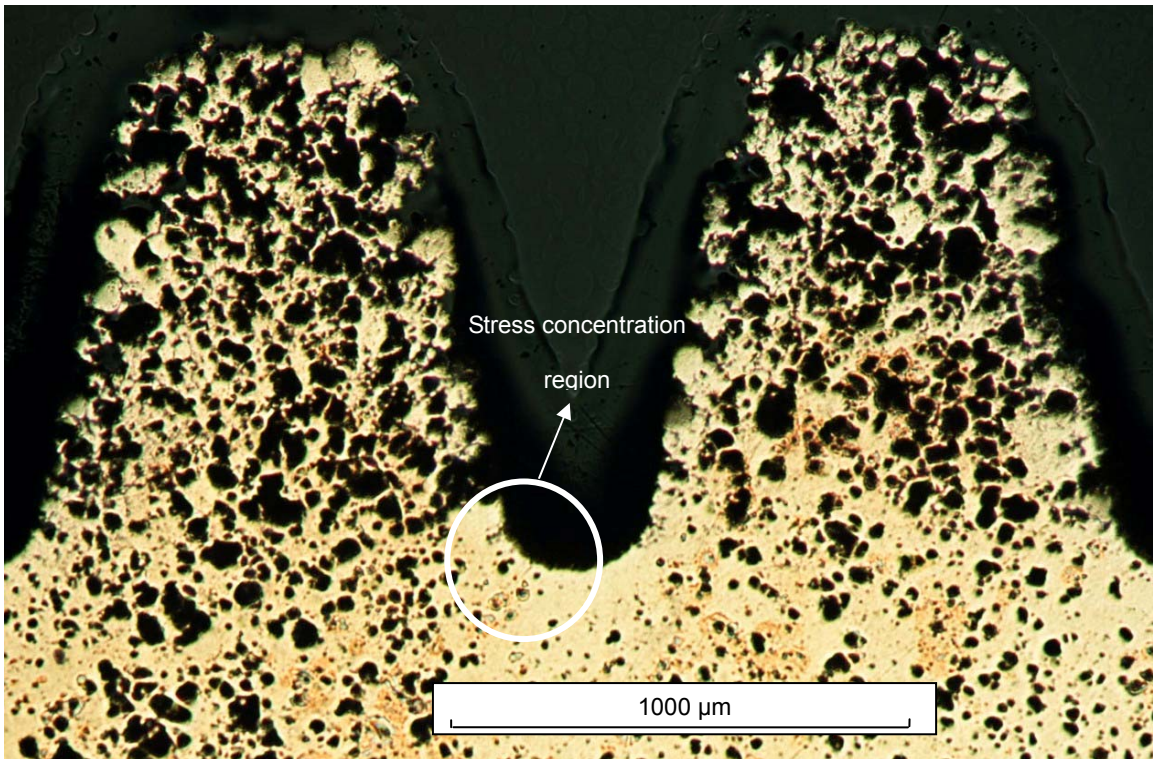
### 3.3.2 Experimental Results and Discussions

As shown in Figure 3-7, micro-protrusions with an aspect ratio of 1.2 were successfully formed by hot compaction. As mentioned in the previous chapter, the maximum achievable aspect ratio is only 0.5 if sequential cold compaction and incomplete sintering technique was employed. Compared with the sequential method, hot compaction technique significantly increased the achievable aspect ratio by providing a better powder bonding strength. In addition, the spacing between the micro-features was also reduced greatly. Since the lower corner of the micro-protrusion is the stress concentrated region (Figure 3-8), the compacted part usually develops cracks in that area. To avoid cracking, it is preferred to increase the spacing between the micro-features to reduce the stress gradient in the corner region. In the cold compaction case, a large gap between features (about 2 mm) was employed to make sure that the desired micro-feature could be successfully formed. However, in the hot compaction case, this concern is no longer a constraint. The enhanced diffusion ensures a good particle bonding to overcome the stress concentration. In this study, the gap between micro-features is 0.2 mm, limited by the wire size used in our EDM process.



**Figure 3-7 Hot compacted part: a) successfully formed micro-features; b) magnified cross-sectional view (insert #1)**

The interconnected porous structure of the hot compacted micro-protrusion is shown in Figure 3-8. Water drops were added to the top of the part, and was found on the bottom of the part instantly, which indicates that the pores are open. Due to the pressure gradient in the cavity of the insert during compaction, the porosity of the formed micro-protrusion is not homogeneous. Generally speaking, the upper portion has a higher porosity than the lower portion, and the internal region has a higher porosity than the outer section for the micro-protrusion.



**Figure 3-8 Interconnected porous structure of the formed micro-features (insert #1)**

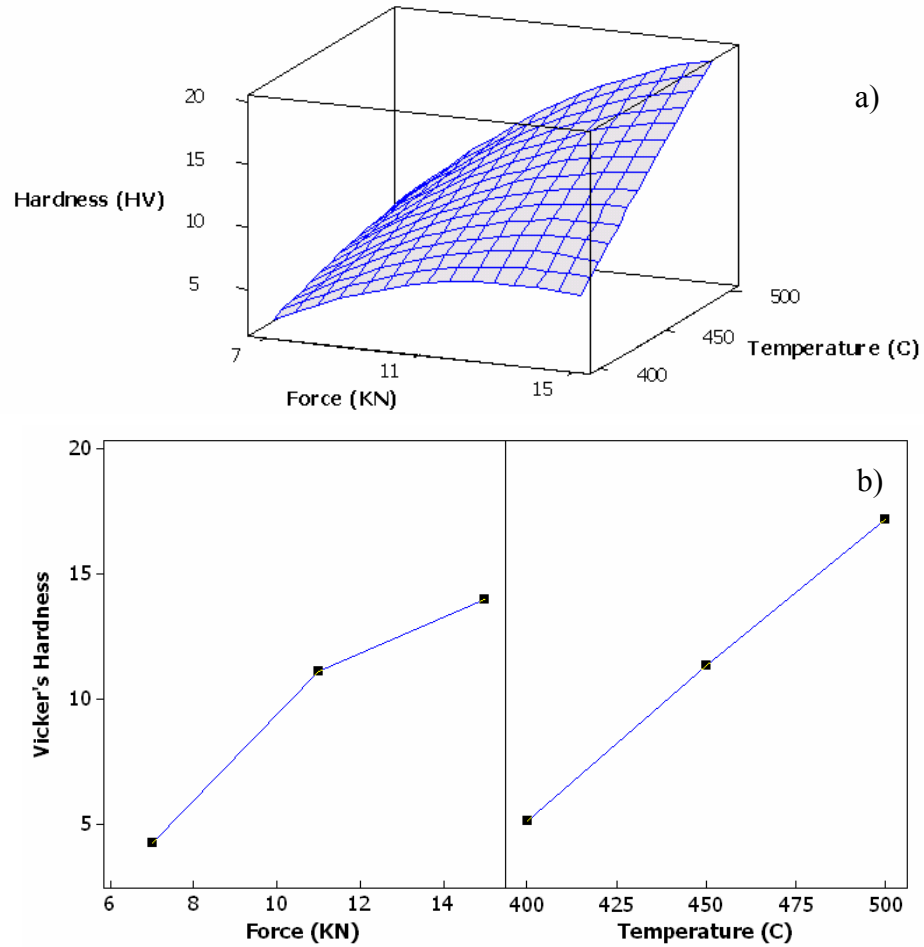
### **3.3.2.1 Effects of Process Variables on the Part Quality (insert #1)**

To systematically investigate the effects of process variables on the part quality, a response surface experiment design was employed. The compaction force and the target temperature of thermocouple B were chosen as design factors with three levels. Based on our preliminary experimental tryouts, the compaction force was set in the range of 7-15 kN (corresponding to a pressure of 15 – 32 MPa), and the temperature was selected in the range of 400-500 °C. Hardness and porosity were used as the measurements of the part quality. As summarized in Table 3-2, a central composite design with five center points was used for this 2-factor and 3-level experimental design. Analysis was carried out using MINITAB (a statistical software).

Runs	Factors		Responses	
	Force (kN)	Temperature (°C)	Porosity	Hardness (Hv)
1	15	500	0.18	18.45
2	11	450	0.27	11.74
3	7	450	0.30	4.17
4	11	500	0.19	16.53
5	11	450	0.30	11.47
6	11	450	0.27	10.36
7	15	400	0.28	7.59
8	11	450	0.25	10.99
9	7	400	0.47	3.35
10	11	400	0.36	4.88
11	7	500	0.38	5.2
12	15	450	0.23	14
13	11	450	0.25	10.93

**Table 3-2 Experimental design and results**

To ensure that the compacted micro-features could function well under certain loading conditions, it is crucial to have a good bonding strength between neighboring particles. Practically speaking, it is very difficult to directly measure the bonding strength between two micro-powders. Therefore, we used the micro-hardness of the compacted micro-protrusion as an indication of the powder bonding strength. The measured Vickers's hardness is listed in Table 3-2.

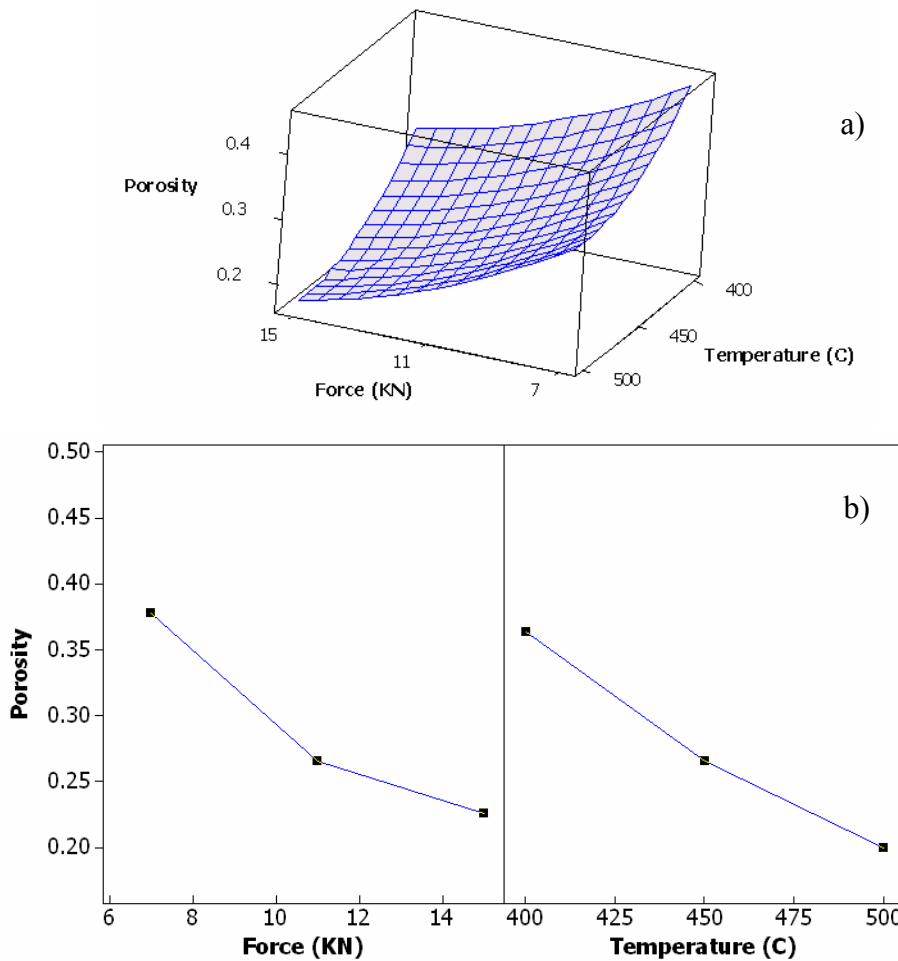


**Figure 3-9 Effects of design factors on the hardness: a) response surface; b) main effect plot**

The response surface of the hardness is shown in Figure 3-9a. The main effect of factors on the hardness is shown in Figure 3-9b. Basically, as the force and temperature increased, the mechanical strength of the part increased correspondingly. To investigate whether the factors are significant, the analysis of variance (ANOVA) was used. Factors with a p-value less than 0.05 were considered significant. It was found that force, temperature, force to the power of two, and the interaction between force and temperature have significant effect on the resulting part hardness. The regression model of hardness as a function of above factors is:

$$H = 11.1 + 2.277 * \frac{F - 11}{4} + 2.03 * \frac{T - 450}{50} + 1.126 * \frac{F - 11}{4} * \frac{T - 450}{50} - 1.012 * \left(\frac{F - 11}{4}\right)^2 \quad (3-1)$$

where H is vicker's hardness, F is force (kN) and T is temperature (°C).



**Figure 3-10 Effects of design factors on the porosity: a) response surface; b) main effect plot**

For different applications, different porosity is desired. Therefore, it is necessary for the manufacturer to control the porosity of the formed part. By using image

processing software (ImageJ), the porosity of the formed micro-protrusions was measured from the microscopic picture taken from the cross-sectional view of the part. For each case, the porosity at twelve different cross sections was measured, and the average value was used. Table 3-2 shows the measurement results.

The response surface of the porosity is shown in Figure 3-10a. The main effect of factors on the porosity is shown in Figure 3-10b. Basically, as the force and temperature increased, the porosity of the part decreased correspondingly. It was found that force and temperature had a significantly negative effect on the porosity. The interaction of temperature and force does not have a significant effect on the porosity. Therefore, a desired porosity could be obtained by tuning either the force or temperature. The regression model of porosity as a function of above factors is:

$$P = 0.2599 - 0.039 * \frac{F - 11}{4} - 0.03 * \frac{T - 450}{50} \quad (3-2)$$

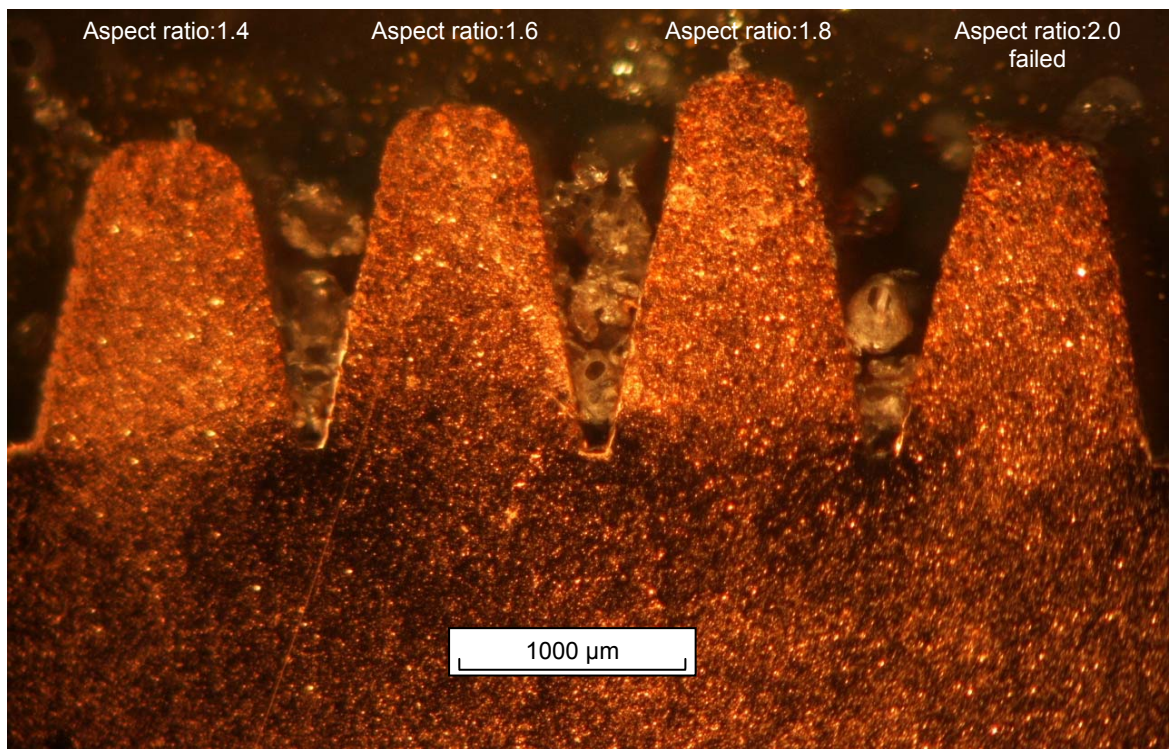
where P is porosity, F is force (kN) and T is temperature (°C).

### **3.3.2.2 Achievable Aspect Ratio (Insert #2)**

The bonding strength of the particles during pressure assisted sintering (hot compaction) depends greatly on the amount of pressure. As the aspect ratio increases, the pressure in the tip area decreases, which results in a low bonding strength in that area. If the bonding strength is below a certain level, the tip will break during disassembly. Therefore, the achievable aspect ratio is limited in this process. Die insert #2 was designed to investigate the maximally achievable aspect ratio under a certain



experimental condition. In this set of experimental study, the temperature was fixed at 500 °C, and the compaction force was in the range from 15 kN to 27 kN. When a 15 kN compaction force was applied, we successfully formed micro-protrusions with aspect ratio of 1.4 and 1.6, but the micro-protrusions broke for the aspect ratio of 1.8 and 2.0. As the force increased to 21 kN, the achievable maximal aspect ratio increased to 1.8. We then further increased the compaction force to 27 kN; however, the 2.0 aspect ratio protrusion was still not successfully formed (Figure 3-11).

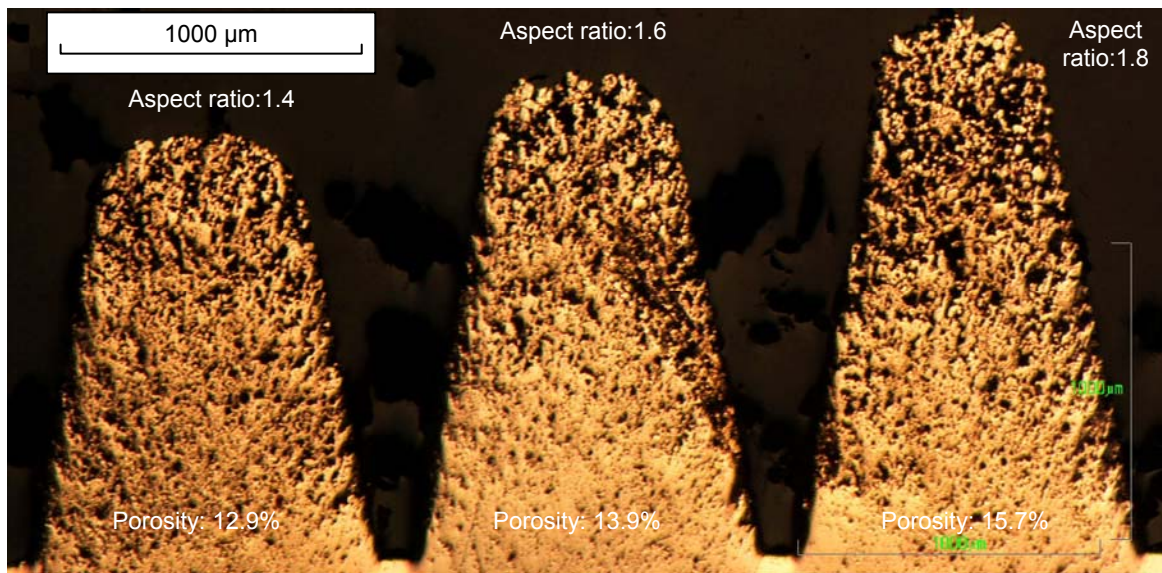


**Figure 3-11 Magnified cross-sectional view (insert #2)**

Although it may be possible to eventually form higher aspect ratio at higher compaction force, we decided not to pursue further in this direction due to the following two concerns: 1) As the aspect ratio increases, the pressure differential between the tip



area and the lower section becomes higher. The pressure distribution in the tip area is very low, which requires an extremely high overall compaction force to form. 2) Due to the same reason, the porosity differential from tip to the lower section becomes significant as the aspect ratio increases. As shown in Figure 3-12, the porosity at the lower section almost disappeared for 1.8 aspect ratio protrusion.



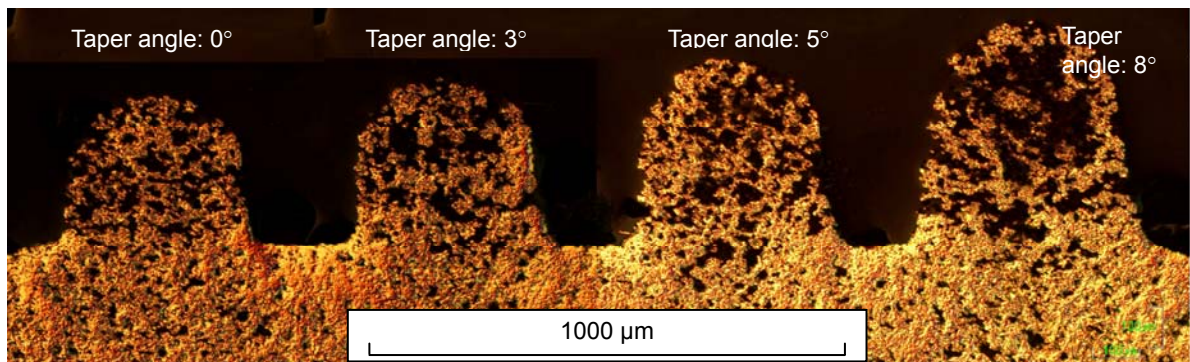
**Figure 3-12 Interconnected porous structure of the formed micro-features (insert #2)**

The overall porosity of the micro-protrusion was measured. For the 27 kN compacted part (Figure 3-12), it was found the porosity was 12.9%, 13.9% and 15.7% for 1.4, 1.6 and 1.8 aspect ratio protrusions respectively. In conclusion, as the aspect ratio increased, the overall porosity of a micro-protrusion compacted at the same pressure increased, and so did the pressure differential.

### 3.3.2.3 Achievable Minimal Taper Angle (Insert #3)

In some applications, a low taper angle is desired. For example, in the boiling heat transfer study done by Liter and Kaviany (Liter and Kaviany 2001), a micro-protrusion without taper was desired to better separate liquid and gas phases. However, due to the limitations of their fabrication method, Liter and Kaviany were only able to obtain micro-protrusions with a taper angle of  $10^\circ$ .

Therefore, die insert #3 was designed to investigate the capability of the hot compaction to produce less tapered walls. As shown in Figure 3-13, we successfully formed high aspect ratio (1.5) micro-protrusions with different taper angles ranging from  $0^\circ$  to  $8^\circ$ . The part in Figure 3-13 was formed at  $500^\circ\text{C}$  with a compaction force of 15 kN, and the porosities of all protrusions were around 30%.



**Figure 3-13 Successfully formed micro-protrusions with different taper angles (insert #3)**

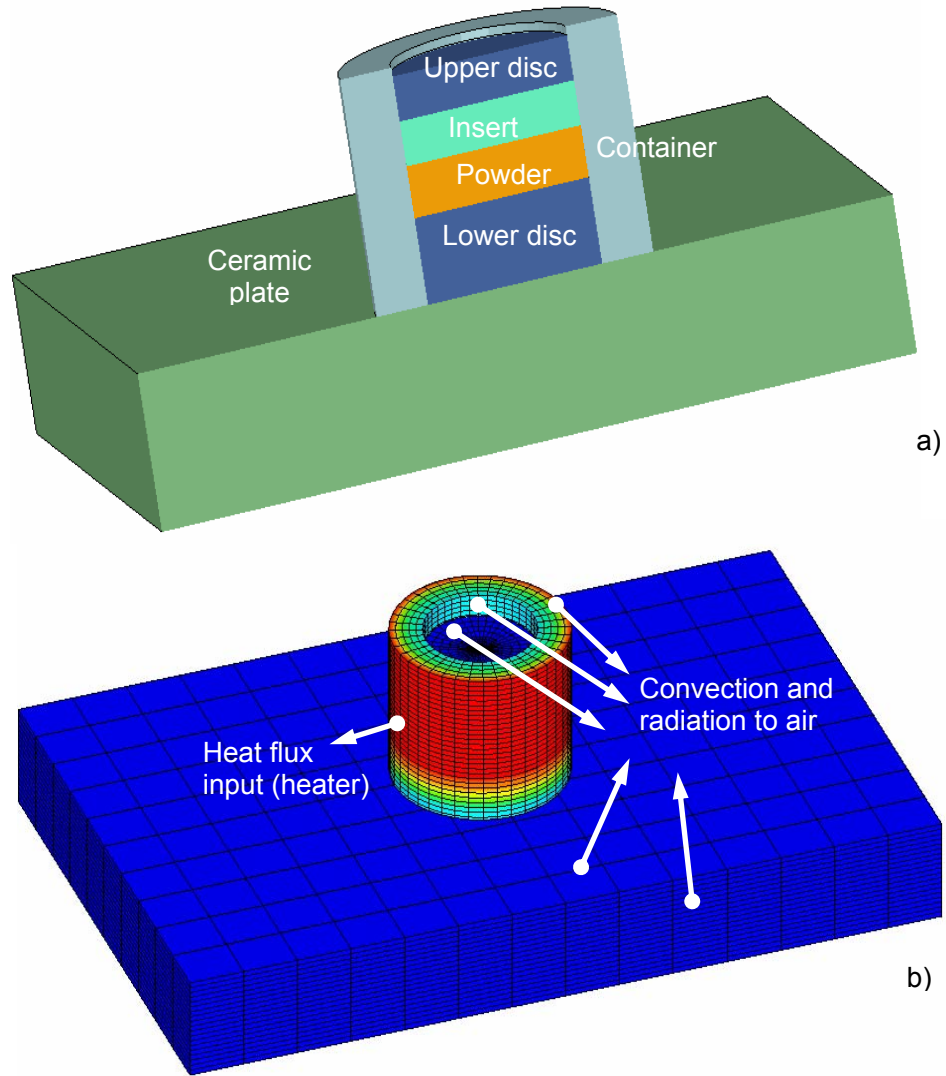
### 3.4 Thermal Analysis of the Hot Compaction System

In order to obtain the exact temperature distribution inside the container (especially the powder), a thermal analysis of the hot compaction system was carried out

using finite element analysis (FEA). The simulation results were validated with the experimental measurements. And the temperature history of the powder was predicted using this FEA model.

### **3.4.1 Finite Element Modeling of the Heat Transfer Process**

A finite element analysis (FEA) model was developed using the commercial FEA software, LS-DYNA 970. As shown in Figure 3-14, a 3D model was constructed, which included the ceramic base, container, insert, powder and two discs. The material properties used in the simulation are summarized in Table 3-3. The conductivity of the copper powder after 4KN pre-press was found to be 120 W/m/K according to Walter and Trowell (Walter and Trowell 1971). The specific heat of copper is independent of porosity, which is 385 J/kg/K (Holman 1997). The conductivity and specific heat of stainless steels are: 16.2 W/m/K and 500 J/kg/K (Holman 1997). Based on the data specification sheet, alumina silicate has a very low conductivity: 1.08 W/m/K, and its specific heat is 1050 J/kg/K. According to the matweb.com, the thermal expansion coefficient of stainless steel 316 is 16  $\mu\text{m}/\text{m}\cdot^{\circ}\text{C}$ . Thermal contact conductance between copper and steel is around 3030  $\text{W}/\text{m}^2/\text{K}$  (Yuncu 2006). Between stainless steel components, the contact conductance is 3000  $\text{W}/\text{m}^2/\text{K}$  (Fitzroy 1970). And the contact conductance between alumina silicate and stainless steel was assumed to be 400  $\text{W}/\text{m}^2/\text{K}$  based on the data published by Yuncu (Yuncu 2006).



**Figure 3-14 FEA model: a) cross-sectional view; b) boundary conditions**

The convection heat transfer coefficient in the air is usually in the range of 5-200 W/m<sup>2</sup>/K (Holman 1997). And the radiation heat transfer coefficient could be approximately calculated using the following equation:

$$h_{rad} = \sigma \varepsilon F \frac{T_2^4 - T_1^4}{T_2 - T_1} \quad (3-3)$$

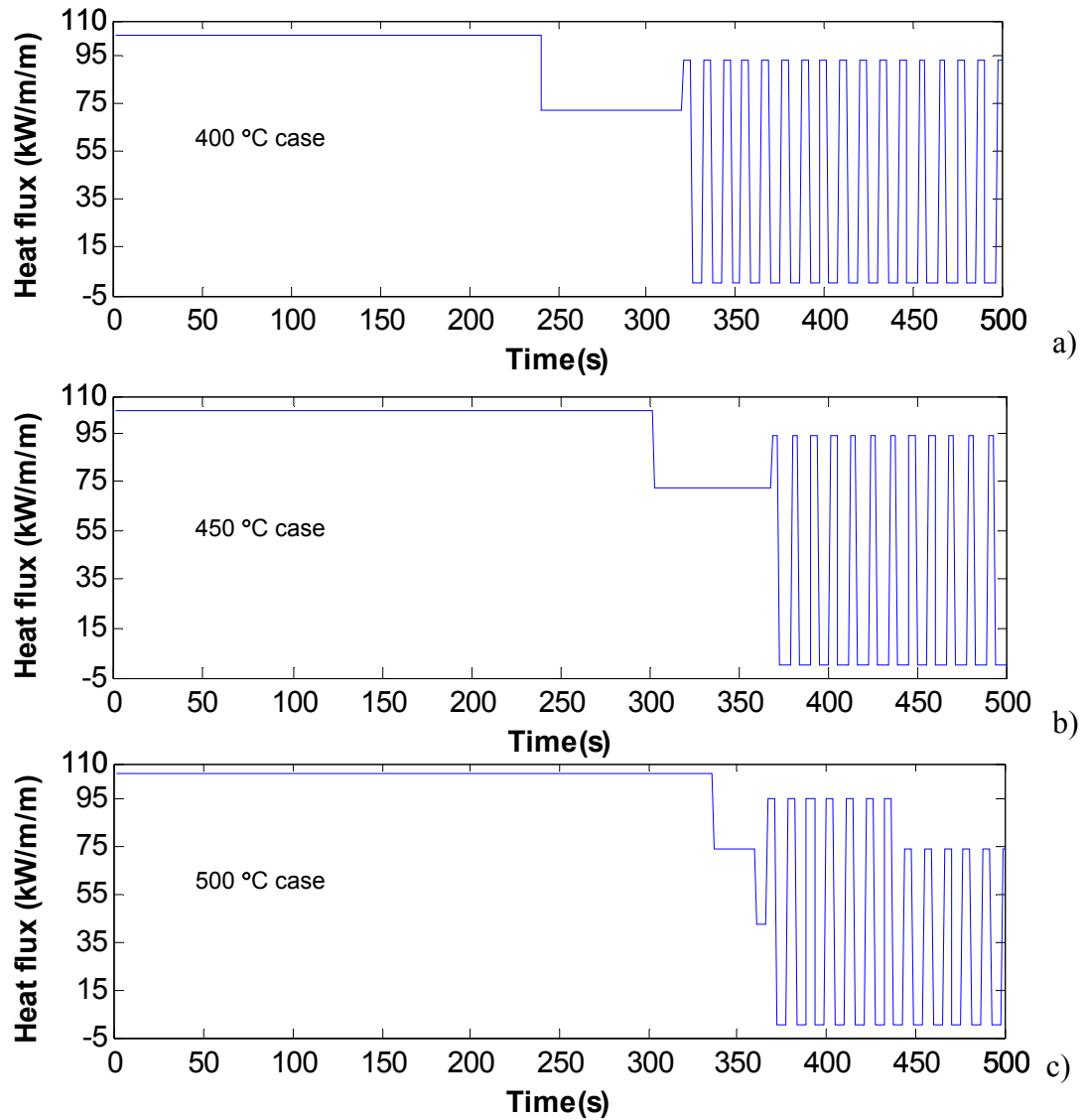
where  $\sigma$  is stefan boltzmann constant and equals to  $5.67e-08 \text{ W / m}^2 \text{ K}^4$  ;  $F$  is view factor (no units), the assumption is that the surface segments has an unobstructed view of the environment, the view factor is therefore 1;  $\varepsilon$  is surface emissivity (no units).  $\varepsilon = 0.074$  for Stainless steel,  $\varepsilon = 0.4$  for Alumina (Holam 1997);  $T_2$  is the part temperature and  $T_1$  is the air temperature. Assuming  $T_2$  equals to  $627 \text{ }^\circ\text{C}$  for stainless steel components and  $177 \text{ }^\circ\text{C}$  for ceramic base, the radiation heat transfer coefficient would be  $4.52 \text{ W/m}^2/\text{K}$  for stainless steel parts and  $4.94 \text{ W/m}^2/\text{K}$  for the ceramic base. In this study, a combined convection and radiation heat transfer coefficient was used. Based on the above calculations and calibration with the experiments, a combined value of  $30 \text{ W/m}^2/\text{K}$  was found to be a best fit to the experimental results.

Material	Conductivity (W/m/K)	Specific heat (J/kg/K)	Contact conductance with stainless steel (W/m <sup>2</sup> /K)
Copper powder (4kN pressed)	120	385	3030
Stainless steel	16.2	500	3000
Alumina silicate	1.08	1050	400

**Table 3-3 Material properties used in simulation**

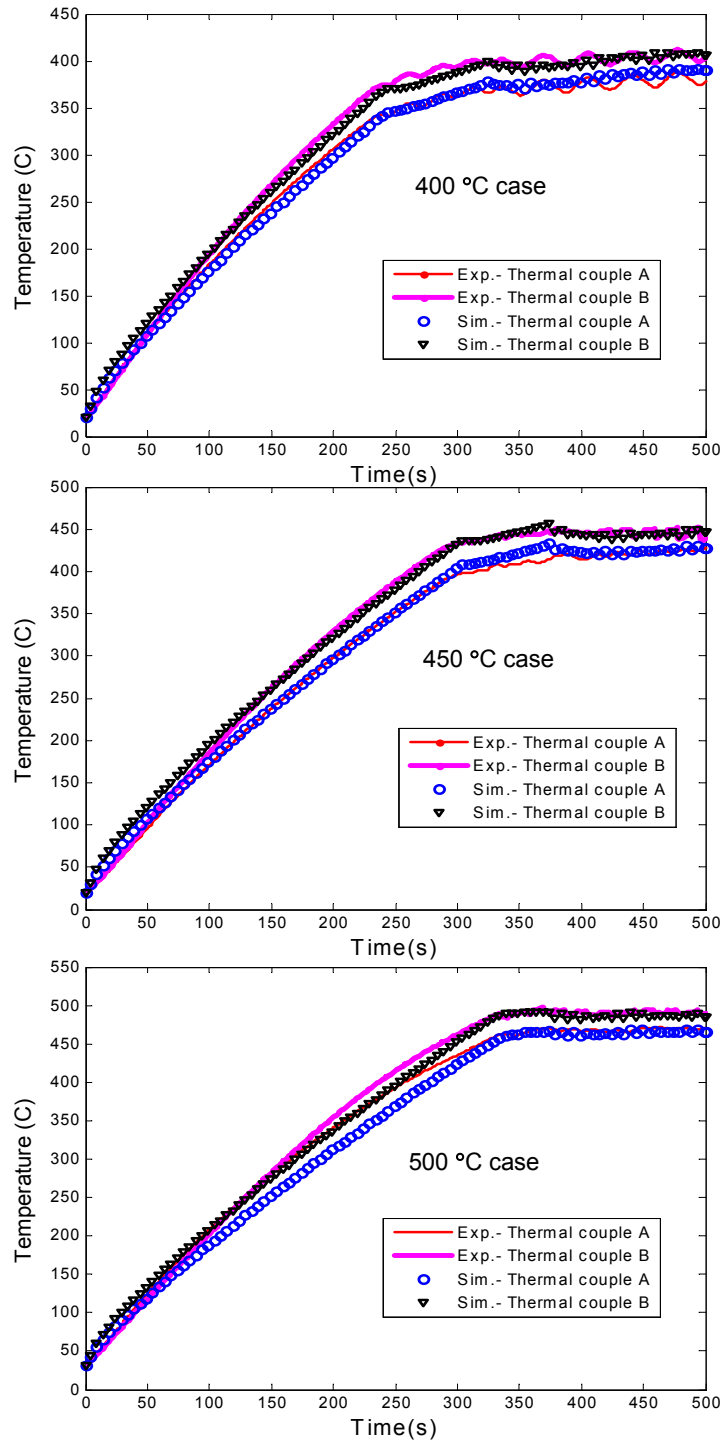
### 3.4.2 Results and Discussions

In the experiments, three levels of temperature were set as the target temperature at the thermocouple B location:  $400 \text{ }^\circ\text{C}$ ,  $450 \text{ }^\circ\text{C}$  and  $500 \text{ }^\circ\text{C}$ . By tuning the PID controller and calibrating the finite element model, it was found that the input heat flux for each temperature level was as shown in Figure 3-15.



**Figure 3-15 Heat flux input for different target temperatures: a) 400 °C; b) 450 °C; c) 500 °C**

For validation, the simulated temperature history of thermocouple A and B locations was compared with the data collected during experiment for each case. As shown in Figure 3-16, the simulation results are in good agreement with the experiments.



**Figure 3-16 Validation of the simulation with experiment**

During the hot compaction process, one of the most important requirements is that

the temperature distribution of the workpiece must be uniform. The simulation confirmed that the temperature difference between different regions was less than 10 °C for all the cases. The simulated temperature history of three different sections in the powder for all three cases is shown in Figure 3-17. For all the cases, it took less than 400 seconds to reach a steady-state temperature. The average powder temperatures for each case are: 384 °C (thermocouple B temperature: 400 °C); 422 °C (thermocouple B temperature: 450 °C); and 460 °C (thermocouple B temperature: 500 °C).

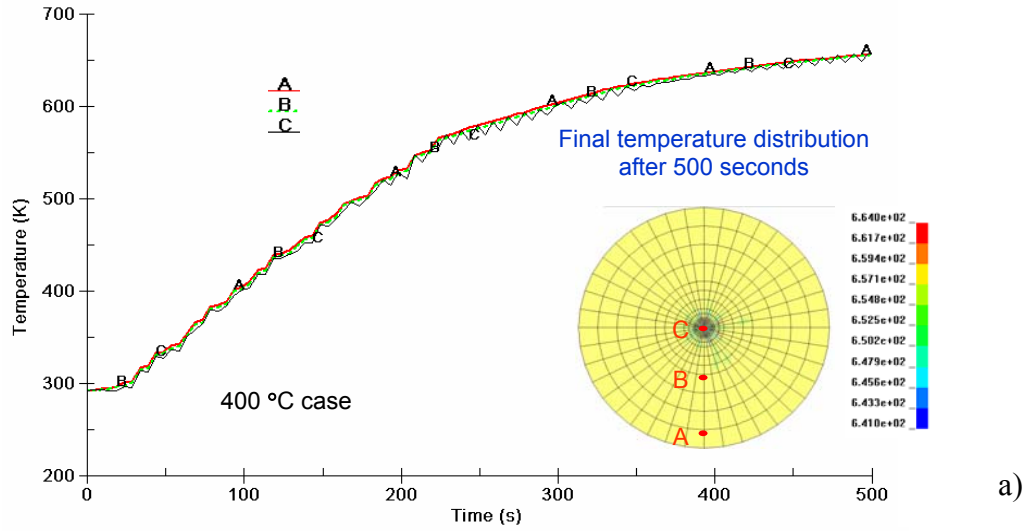
### **3.5 Particle/substrate bonding produced by hot compaction**

For advanced heat transfer application, it is essential to be able to coat the porous micro-features onto a solid substrate with a minimal thermal resistance. In this section, hot pressing experiments were carried out to bond the particle layer with a substrate. The bonding strength was tested with tape test and deformation test.

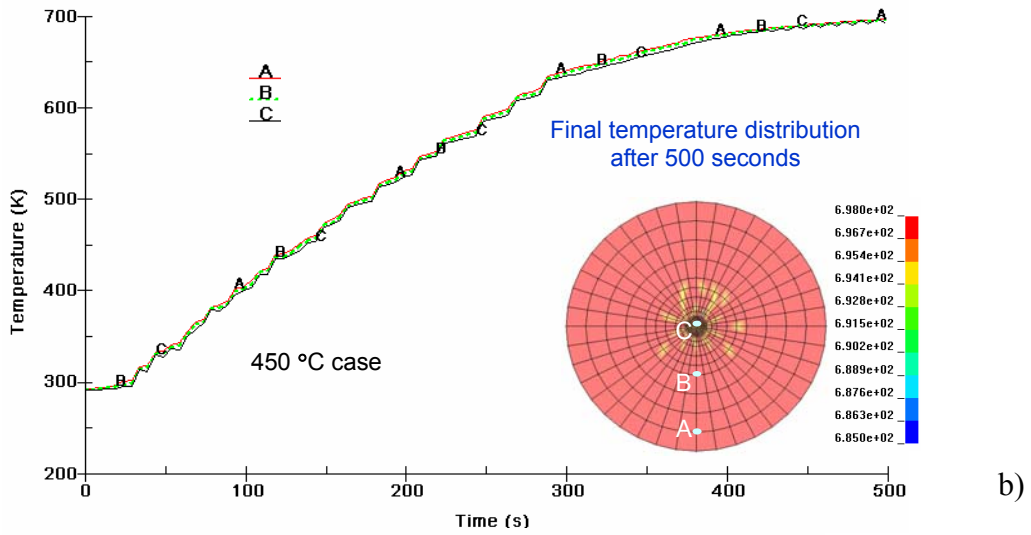
#### **3.5.1 Experimental Setup and Procedures**

Same experimental setup and procedure as used for hot powder compaction (Figure 3-3) was employed, along with insert #1 (Figure 3-4). As shown in Figure 3-18, an alloy 101 copper substrate with a thickness of 812µm was used. In order to avoid any surface oxidation or impurities to interfere with the bonding, the surface of the substrate was scratched with a 60 grit sand paper.

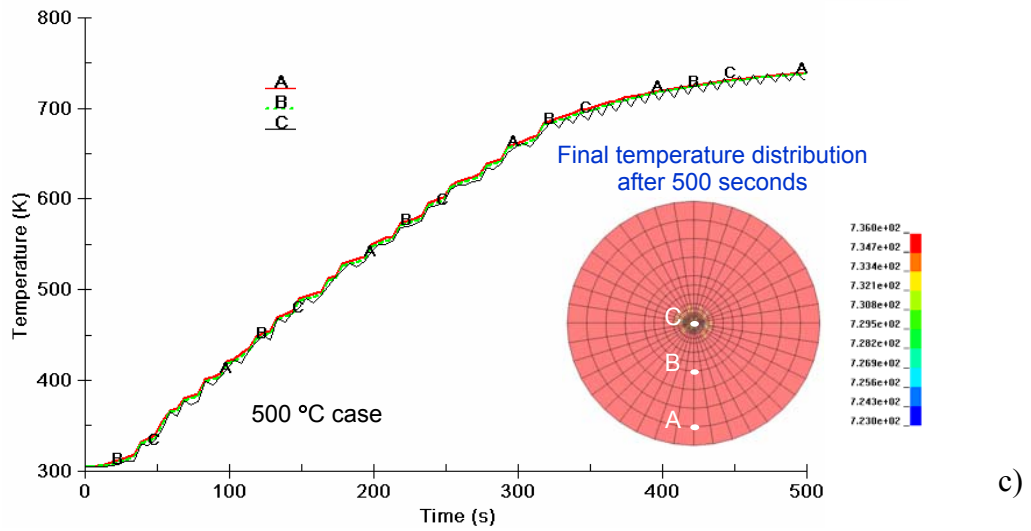




a)

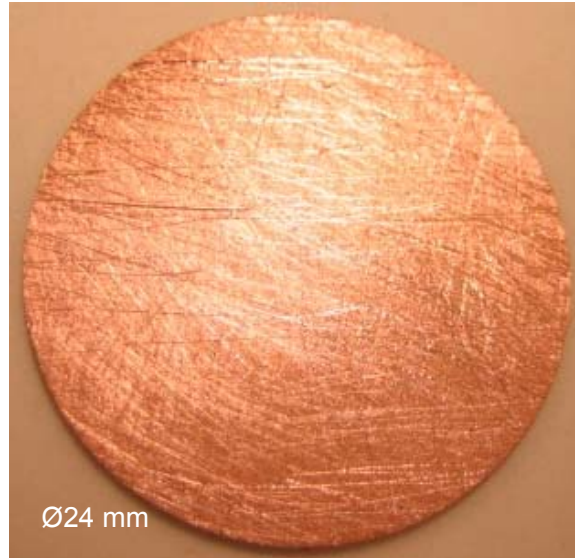


b)



c)

Figure 3-17 Temperature distribution of the powder: a) 400 °C; b) 450 °C; c) 500 °C

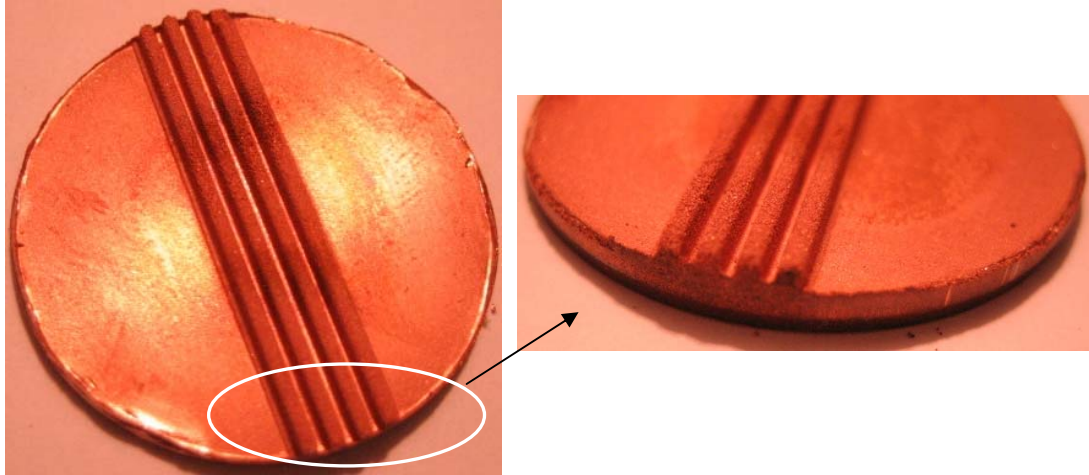


**Figure 3-18 Copper substrate with scratched surface**

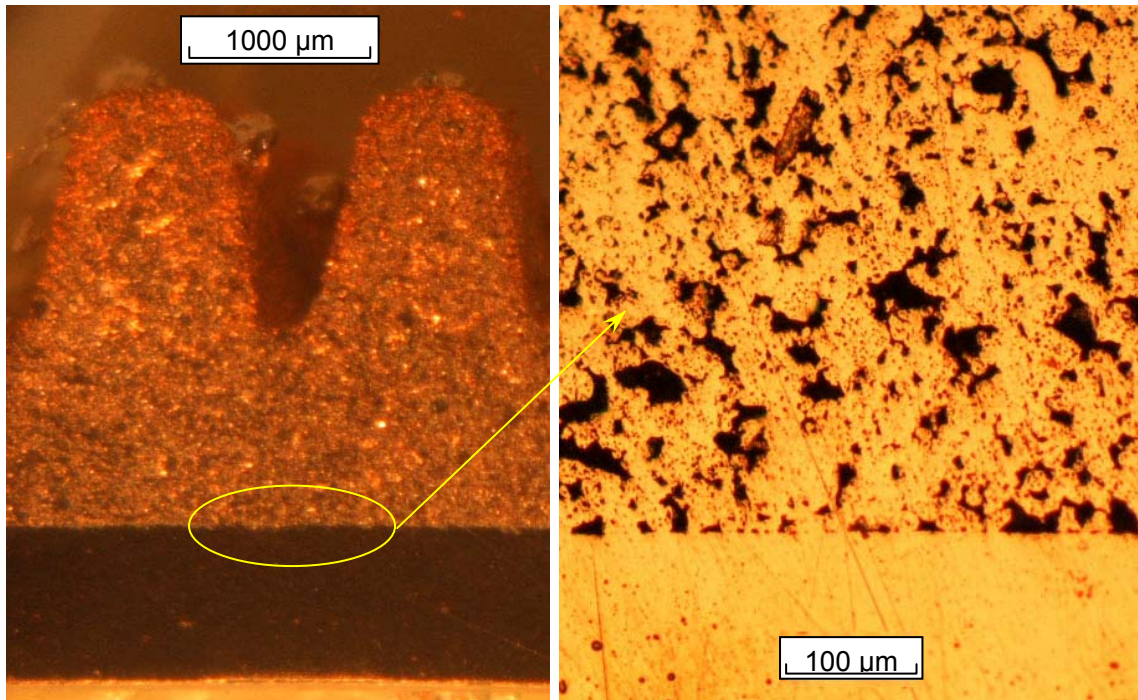
In the experiment, the copper substrate was placed on the top of the lower disc inside the container, and then the copper powder was poured onto the substrate. Temperature was set at 450 °C and a force of 11 kN (23.6 MPa) was used.

### **3.5.2 Experimental Results and Discussions**

As shown in Figure 3-19, the porous layer with micro-features was successfully bonded onto the copper substrate. A magnified cross-sectional view of the particle/substrate interface is shown in Figure 3-20. Atoms diffused well in those connected areas. Crystalline micro-structure was successfully formed, which could reduce thermal resistance between particles and the substrate when compared with non-crystalline bonding produced by conventional bonding techniques.



**Figure 3-19 Particle/substrate bonding made by hot pressing**

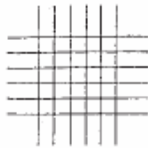
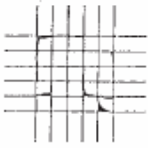
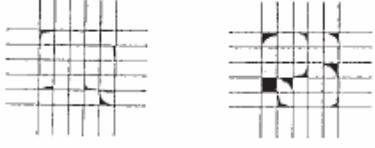
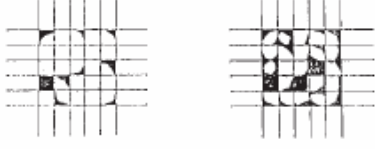

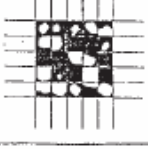


**Figure 3-20 Microscopic pictures of the bonding interface**

Based on the bonding test techniques employed by other researchers (O'Neill et al. 1971; Chang and You 1997), tape test and deformation test were used in our study to test the particle/substrate bonding strength.

### 3.5.2.1 Tape Test

Tape test is an ASTM standard (ASTM D3359) developed for assessing the adhesion of coating to metallic substrates by applying and removing pressure-sensitive tape over cuts made in the coating (Chang and You 1997). As shown in Figure 3-21, a reference is provided by ASTM for the classification of test results.

CLASSIFICATION OF ADHESION TEST RESULTS		
CLASSIFICATION	PERCENT AREA REMOVED	SURFACE OF CROSS-CUT AREA FROM WHICH FLAKING HAS OCCURRED FOR SIX PARALLEL CUTS AND ADHESION RANGE BY PERCENT
5B	0% None	
4B	Less than 5%	
3B	5 - 15%	
2B	15 - 35%	
1B	35 - 65%	
0B	Greater than 65%	

Classification of Adhesion Test Results

Figure 3-21 Reference for the tape test (ASTM D3359)

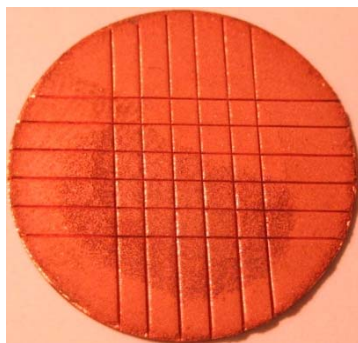


To prepare the specimen for the tape test, a cutting block with six heavy duty blades was fabricated using EDM. As shown in Figure 3-22, 6 blades were spaced 2 mm apart, and the MTS 810 machine was used to apply the cutting force. The compression was carried out at a very slow speed (0.1 mm/min) until the coating was cut through.

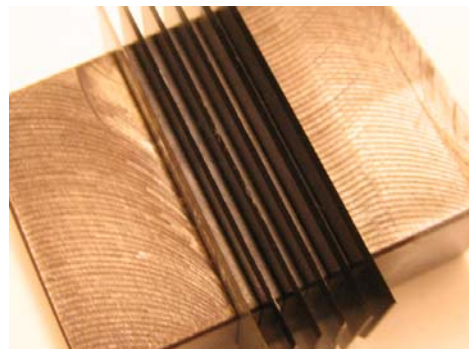
An 87 N/100 mm tape (Permacel P-665) was used. After the tape was removed, nothing was peeled off, which corresponded to a classification of 5B (Figure 3-21), indicating a very strong bonding between the porous layer and the substrate.



a)



b)



c)

**Figure 3-22 Specimen cutting for tape test: a) Compression cutting; b) Specimen made; c) Cutting block**

### 3.5.2.2 Deformation Test

O'Neill et al. employed deformation test to characterize the bonding strength of their coating (O'Neill et al. 1971). The specimen was deformed to see if the particles will be torn away before the porous coating cracks. In our study, we used three-point bending test to deform our specimen. As shown in Figure 3-23, the porous coating with micro-features held well to the substrate even after a large bending deformation, which again proved that the hot pressing could produce a strong particle/substrate bonding.



**Figure 3-23 Three-point bending test**

### 3.6 Conclusions

In this study, the forming of porous micro-features and particle/substrate bonding using hot compaction was studied. A hot compaction process for the fabrication of micro-scale porous features with high aspect ratio was successfully developed. A cost-effective hot compaction system was designed and fabricated, which could be easily integrated into the existing manufacturing facilities. The thermal analysis of the system was

simulated using FEA. The temperature distribution of the workpiece was found to be uniform and the heating speed was fast. The effects of compaction force and temperature on the part quality were investigated. In addition, the achievable aspect ratio and taper angle were also discussed. On the basis of the quantitative and qualitative analysis made herein, the following conclusions were drawn:

1. Compared with sequential cold compaction and sintering technique, hot compaction method has the following advantages: 1) required compaction force is low; 2) the achievable aspect ratio is much higher; and 3) the spacing between micro-features could be significantly reduced.
2. Both temperature and force have a positive effect on the powder bonding strength. The interaction of temperature and force has a positive influence on the strength as well.
3. The porosity reduces as the temperature and force increase. It is found that the porosity can be easily controlled by varying the force and temperature. The interaction of the temperature and force does not have a significant effect on the porosity.
4. Compared with other fabrication techniques, hot compaction method has the following main advantages: 1) the achievable maximal aspect ratio is high (1.8 in this study); 2) taper angle can be eliminated; 3) compatibility with

existing equipment is high, and it is possible to realize high volume production with this technique.

5. Low thermal-resistant bonding between porous layer and substrate could be achieved using hot pressing. The bond could sustain severe peeling and bending forces.



**CHAPTER 4**

**DISCRETE ELEMENT MODELING OF THE PRESSURE ASSISTED  
SINTERING PROCESS**

**4.1 Introduction**

It is costly and time-consuming to determine a proper experiment setting (force and temperature) by trial and error. As studied in previous sections, product qualities (such as mechanical strength and porosity) are significantly affected by the setting of the process variables.

In order to virtually study the effect of the force and temperature on the particle bonding strength and porosity, it is necessary to develop a computational model. In this section, we first reviewed existing modeling techniques for sintering and pressure assisted sintering processes. A summary and comparison of different techniques was provided.

Existing models do not take into accounts of heat directly, and boundary conditions imposed by die wall are usually not considered. Therefore, a discrete element model for pressure assisted sintering was developed for the forming of porous micro-features. The model was first validated with experimental results for a unit problem (two particles). And then it was expanded for a ten-particle channel hot pressing problem.

With such a model, we could conveniently assess the effects of force and temperature on the particle bonding strength and shrinkage, which will give us insight on deciding a proper process setting even before the actual operations (Chen and Ni 2008).

## **4.2 Literature Review**

As explained in Chapter 2, sintering process is achieved via atomic diffusions caused by agitations. In this section, various modeling techniques for sintering are summarized and compared.

### **4.2.1 Computational Modeling of Sintering Processes**

Starting from late 1950s, numerous researchers have studied the computer simulation of sintering processes (German 2002). Lots of publications can be found on this topic. According to the different scales of constitutive modeling, the existing computer models for sintering could be divided into three classes: (1) continuum model; (2) discrete model; (3) molecular dynamics model. These models will be explained as follows.

#### **4.2.1.1 Continuum Models of Sintering**

A porous medium is considered as a two-phase material including the phase of substance (porous body skeleton) and the phase of voids (pores) (Olevsky 1998). The skeleton is assumed to be made of individual particles having in general nonlinear-viscous incompressible isotropic behavior. The pores are isotropically distributed. The overall response is therefore isotropic. The effective sintering stress ( $P_L$ : Laplace pressure), which is introduced by the driving force (reduction of free energy), could be

expressed as follows (Olevsky 1998):

$$P_L(T) = \frac{\partial F}{\partial V} \quad (4-1)$$

where  $F$  is free energy per unit mass of porous medium and it is a function of  $V$  (specific volume) and  $T$  (absolute temperature).

The second law of thermodynamics can be expressed in terms of the Clausius-Duhem inequality (Olevsky 1998):

$$\sigma_{ij} - \frac{\partial F}{\partial V} \delta_{ij} \dot{\varepsilon}_{ij} - \frac{1}{V} \frac{\partial F}{\partial T} + S\dot{T} \geq 0 \quad (4-2)$$

where  $\sigma_{ij}$  and  $\dot{\varepsilon}_{ij}$  are the Cauchy stress tensor and the strain rate tensor,  $S$  is the entropy per unit mass of porous medium, and  $\delta_{ij}$  is the Kronecker symbol.

Considering the above two equations, the constitutive law for a linear-viscous incompressible material with voids can be presented as follows (Olevsky 1998):

$$\sigma_{ij} = 2\eta_0 (\varphi \dot{\varepsilon}_{ij}' + \psi \dot{\varepsilon}_{ij} \delta_{ij}) + P_L \delta_{ij} \quad (4-3)$$

where  $\varphi$  and  $\psi$  are functions of the porosity, and  $\eta_0$  is the shear modulus of the porous body skeleton.

Following a similar methodology, a lot of constitutive models have been

developed especially for hot powder forming recently (Delo et al. 1999; Sanchez et al. 2002; Geindreau et al. 1999). The disadvantage of this kind of model is that an accurate material testing in high temperature condition is required, which is difficult to obtain.

#### **4.2.1.2 Discrete Models of Sintering**

Generally speaking, there are two categories of particle-level models for sintering: (1) models developed for initial and early intermediate stage sintering (German and Lathrop 1978; Hwang and German 1984; Parhami and McMeeking 1994; Parhami and McMeeking 1998), which is dedicated to simulate the diffusion and mass transport mechanisms near the particle surface without grain growth; (2) models for late intermediate and final stage sintering, which is focused on the modeling of grain growth and pore shrinkage (Hassold et al. 1990; Tomandl and Varkoly 2001). The model for final stage sintering is especially important for ceramic sintering since large shrinkage is often encountered. Since this study is only concerned with the initial and early intermediate stages of sintering, only the first model will be discussed in detail in this work.

During the initial and early intermediate stages of sintering, necks between neighboring particles grow up; and no densification occurs. Therefore, a mathematical expression of neck growth as a function of temperature and time will be sufficient to model the free sintering process (no external load) (German and Lathrop 1978; Hwang and German 1984). For pressure assisted sintering (hot powder forming), Parhami and McMeeking have proposed a model which combines neck growth model with the DEM model (Parhami and McMeeking 1994; Parhami and McMeeking 1998).

### Neck growth model

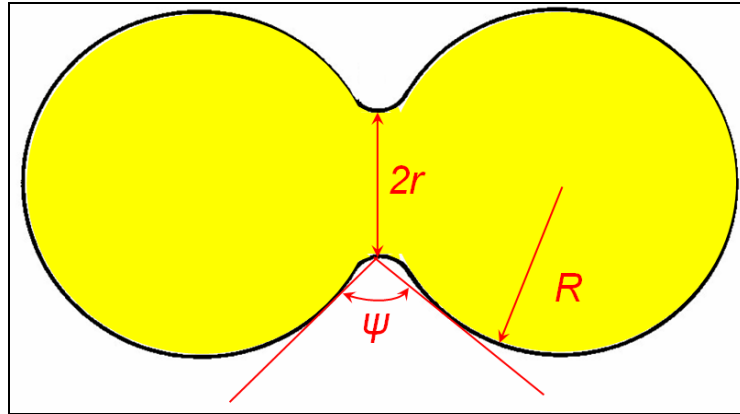
Various types of material transport mechanism including plastic flow, evaporation-condensation, surface diffusion, grain boundary diffusion, and lattice diffusion may occur, either simultaneously or separately. Assuming that the neck has a circular shape, researchers have proposed neck growth models for each mechanism (Hwang and German 1984). In essence, these models can be generalized into the same form as shown in Equation 4-4 with different coefficients ( $n$ ,  $m$ ) for each mechanism (Table 4-1).

$$\frac{r^n}{R^m} = B(D, \gamma, \Omega, \nu, k, T)t \quad (4-4)$$

where  $r$  is the neck radius and  $R$  is particle radius as shown in Figure 4-1, and coefficient  $B$  is a function of  $D$  (diffusion coefficient),  $\gamma$  (surface tension),  $\Omega$  (atomic volume),  $\nu$  (number of diffusion atoms per unit surface area),  $k$  (Boltzmann's constant) and  $T$  (temperature);  $t$  is time.

Mechanism	$n$	$m$
Surface diffusion	7	3
Surface lattice diffusion	5	2
Evaporation-condensation	3	1
Grain boundary diffusion	6.22	2.22
Grain boundary lattice diffusion	4.12	1.12

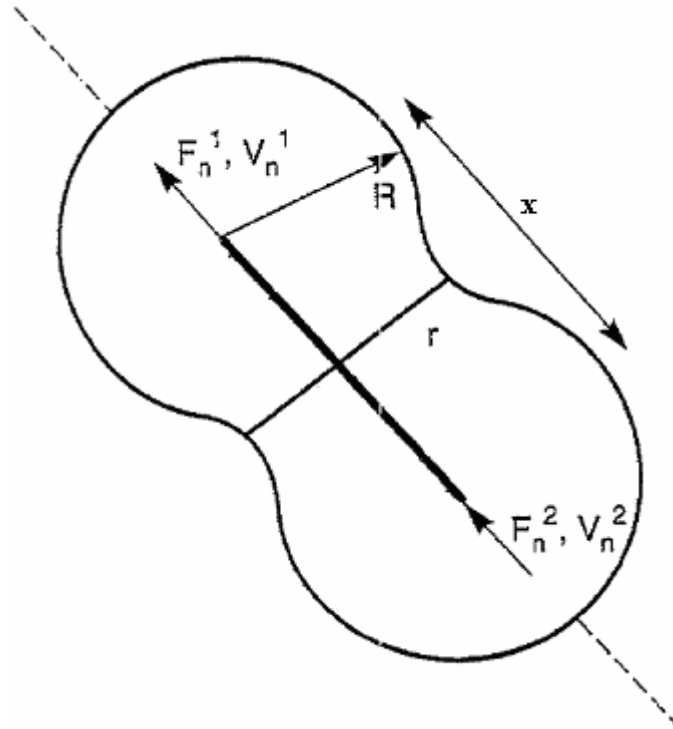
**Table 4-1 Constant  $n$  and  $m$  in Equation 5-4 (Hwang and German 1984)**



**Figure 4-1 Model for the neck growth problem (Hwang and German 1984)**

Multi-particle model for pressure assisted sintering

In the case of hot pressing (pressure assisted sintering), to accurately simulate the particle behavior under the influence of both elevated temperature and external pressure, sintering stress induced diffusion and external pressure induced diffusion should be integrated together. An efficient way to achieve this goal is to combine the existing neck growth model with DEM model, which is called *network model* by some researchers (Parhami and McMeeking 1994; Parhami and McMeeking 1998), or *truss model* (Jagota and Dawson 1988).



**Figure 4-2 2D representation of a 2 particles model**

Similar to the DEM model for compaction, every particle center is represented by a node and every contact between neighboring particles by an element. Figure 4-2 is a 2 dimensional representation of a pair of particles bonded together at a neck. A relative axial velocity of the particle centers is the consequence of atomic flux from the interparticle grain boundary to the free surface. This process, coupled to mass transport on the free surface, leads to the development of grain boundary area at the contact and the generation of thermodynamically induced normal stresses on the grain boundary. Therefore, the axial velocities were related to the thermodynamically induced stress and applied normal stresses caused by external force as follows (Parhami and McMeeking 1994):

$$v_n = \frac{8D_b\sigma}{r^2} + \frac{\alpha(R,\psi)D_b\gamma}{r^4} \quad (4-5)$$

where  $\alpha$  is a constant related to the dihedral angle at the neck ( $\psi$ ) and particle radius ( $R$ ) at the neck (Parhami and McMeeking 1998),  $D_b$  is effective grain boundary diffusivity (which is a function of temperature),  $\gamma$  is the surface tension (surface energy per unit area),  $\sigma$  is the normal stress on the contact and  $r$  is the neck radius. During the early stage of sintering, the dominant mass transport mechanisms are surface diffusion and grain boundary diffusion, in which case the neck growth rate equation could be derived as follows (Parhami and McMeeking 1998):

$$\dot{r} = -\frac{8RD_b}{r^3}\sigma + \frac{8RD_b\gamma}{r^5}\left[4R\left(1 - \cos\frac{\psi}{2}\right) + r\sin\frac{\psi}{2}\right] \quad (4-6)$$

The second terms on the right hand side of Equations 4-5 and 4-6 drive free sintering. In other words, they cause the growth of the neck even when no external forces are applied. The above two equations only describe the basic physical mechanisms of pressure assisted sintering, and the detailed numerical scheme of this model can be found in (Parhami and McMeeking 1998).

#### 4.2.1.3 Atomistic/Molecular Dynamics Models for Sintering

Zavaliangos claimed that the only problem that fits naturally to MD in terms of length scale is that of the sintering of small groups of single crystal nano-particles (Zavaliangos 2002; Raut et al. 1998; Zeng et al. 1998), and that significant advances in



computational power or improvements in MD algorithms are necessary before the results of such simulations become practically useful. For example, Zeng et al. used Oh and Johnson's potential for the sintering simulation of 13 nanofibers (4.4 to 8.8 nm) (Zeng et al. 1998). Raut and his coworker employed a MD/MC CEM (molecular dynamic/Monte-Carlo corrected effective medium) approach to model the sintering behaviors of three single crystal nanoparticles (Raut et al. 1998). As discussed in *section 3.2.3.3*, the MD simulation of polycrystal micro-scale size particle is still very difficult to implement.

#### **4.2.2 Summary of Computational Modeling Techniques for Sintering**

Based on the above reviews on the modeling techniques of powder compaction and sintering, a comparison chart was constructed as shown in Figure 4-3. Continuum model is easy to implement but incapable to obtain microstructure information. MD is highly accurate but is difficult to implement for our problem due to time and length scale limitations. Relatively speaking, multi-particle models stand out to be a sound candidate for the simulation of hot compaction of powders into micro-features.

	Advantage	Disadvantage
<b>Continuum modeling</b>	<ul style="list-style-type: none"> <li>• Easy implementation (FEA)</li> <li>• Short computing time</li> <li>• Accurate prediction of density distribution</li> </ul>	<ul style="list-style-type: none"> <li>• Complicated material model and calibration</li> <li>• Unable to obtain microstructure information</li> </ul>
<b>Multi-particle modeling</b>	<ul style="list-style-type: none"> <li>• Able to obtain microstructure information</li> <li>• No complicated material testing required</li> </ul>	<ul style="list-style-type: none"> <li>• Only suitable for small scale problem</li> <li>• Unable to simulate the interlocking mechanism among particles with irregular shapes</li> </ul>
<b>Molecular dynamics</b>	<ul style="list-style-type: none"> <li>• Able to obtain microstructure information</li> <li>• No material testing required</li> </ul>	<ul style="list-style-type: none"> <li>• Difficult to handle polycrystalline micro-scale particles</li> <li>• Time &amp; length scale limitation</li> </ul>

**Figure 4-3 Comparison of modeling techniques for powder sintering process**

### 4.3 Numerical Modeling of Hot Compaction (Network Model)

Following up the network model described in *section 4.2.1.2*, a numerical model was developed which could predict the pressure assisted sintering (hot compaction) behavior of a particle system as a function of temperature, external force and time.

#### 4.3.1 Formulation of the Numerical Model

Only the initial stage sintering was considered in our case. The neck growth rate equation was derived based on Equation 4-6 and the diffusion coefficient equation used in (Exner 1979):

$$\dot{r} = \frac{8R\delta_g D_{g0} e^{-\frac{Q_g}{R_s T}} \Omega}{kT} \left\{ -\frac{\sigma}{r^3} + \frac{\gamma}{r^5} \left[ 4R \left( 1 - \cos \frac{\psi}{2} \right) + r \sin \frac{\psi}{2} \right] \right\} \quad (4-7)$$

where  $\delta_g$  is the effective grain boundary thickness,  $D_{g0}$  is the maximum grain boundary diffusion coefficient (at infinite temperature),  $\gamma$  is the surface energy per unit area,  $Q_g$  is the activation energy of grain boundary diffusion,  $R_s$  is the gas constant,  $\Omega$  is the atomic volume and  $k$  is Boltzmann's constant. According to Swinkels and Ashby, the values of the above coefficients for copper are shown in Table 4-2 (Swinkels and Ashby 1981).

Material constant	Copper
$\delta_g D_{g0}$ (m <sup>3</sup> /s)	$5.12 \times 10^{-15}$
$\gamma$ (J/m <sup>2</sup> )	1.72
$Q_g$ (J/mole)	105000
$R_s$ (J/mole)	8.31
$\Omega$ (m <sup>3</sup> )	$1.18 \times 10^{-29}$
$k$ (J/Kelvin)	$1.38 \times 10^{-23}$
$\psi$	146°

**Table 4-2 Material property of copper (Swinkels and Ashby 1981)**

Similarly, the axial velocity of the particle was derived based on Equation 4-5:

$$v_n = \frac{8\delta_g D_{g0} e^{-\frac{Q_g}{R_s T}} \Omega}{kT} \left\{ \frac{\sigma}{r^2} - \frac{\gamma}{r^4} \left[ 4R \left( 1 - \cos \frac{\psi}{2} \right) + r \sin \frac{\psi}{2} \right] \right\} \quad (4-8)$$

where  $\sigma$  is the normal stress on the contact as shown in Figure 4-2:

$$\sigma = \frac{F_n^1}{\pi r^2} = -\frac{F_n^2}{\pi r^2} \quad (4-9)$$

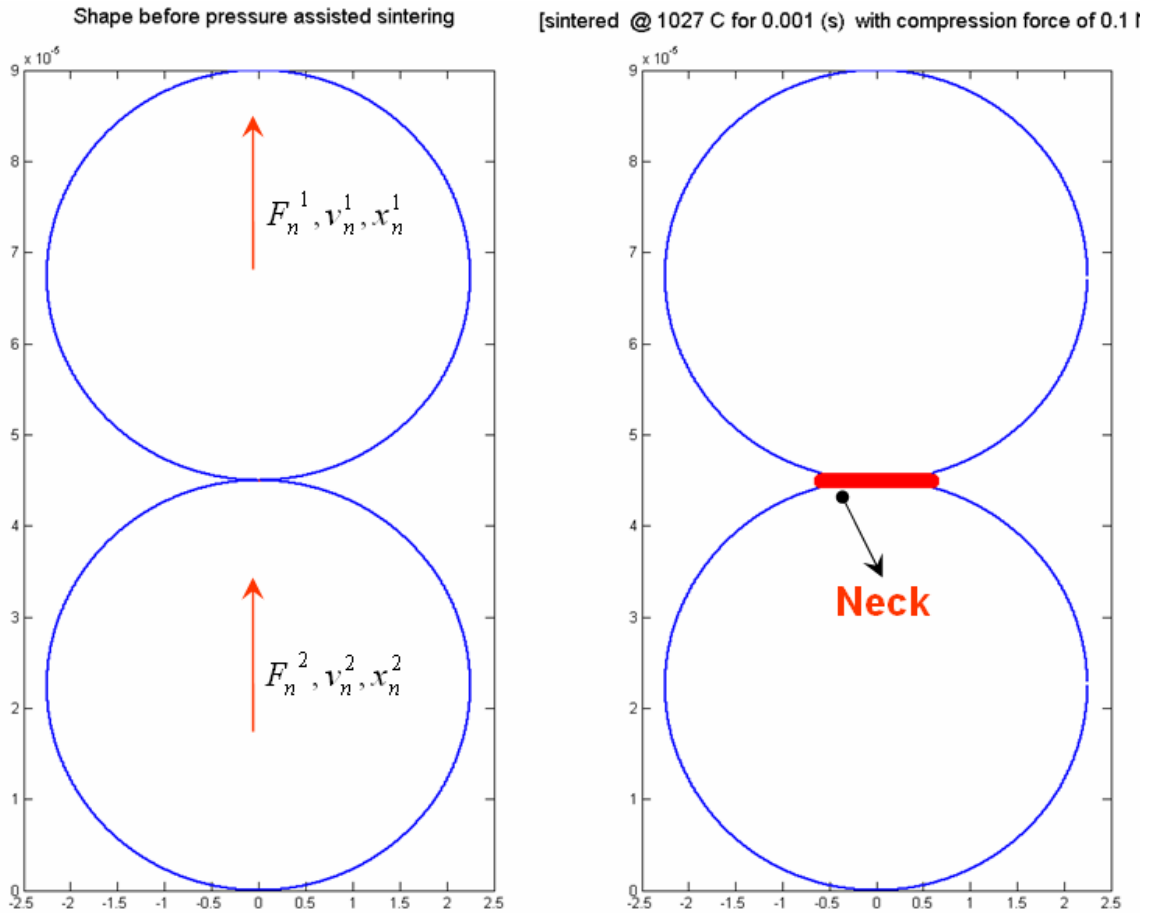
Based on the numerical scheme of DEM (Figure 2-9), the axial displacement of the particle and neck radius are updated using central finite difference method:

$$x_{N+1} = x_N + (v_n)_{N+\frac{1}{2}} \Delta t \quad (4-10)$$

$\Delta t$  was found to be around  $10^{-7}$  s (Martin et al. 2002).

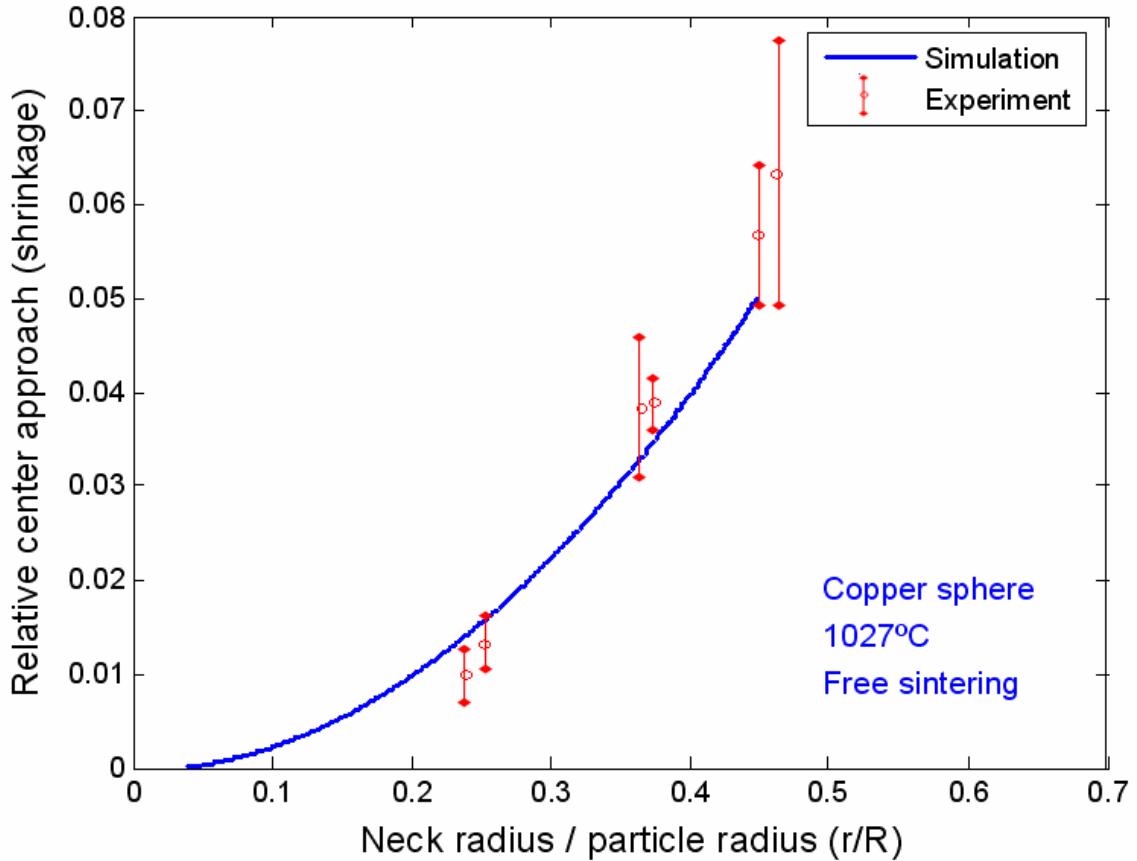
#### 4.3.2 Modeling of Unit Problem and Validation

For a simplified 2 particle model as shown on the left of Figure 4-4, tangential force and moment are ignored. A numerical model for pressure assisted sintering was developed using MATLAB based on Equation 4-7 - Equation 4-10 and Table 4-2. The right diagram in Figure 4-4 is an illustration of calculation result for hot pressing in the format of neck growth.



**Figure 4-4 Illustration of the 2-particle pressure assisted sintering model**

To validate the above numerical model, the simulation results ( $r/R$  and shrinkage) were compared with the experimental results provided by Exner as shown in Figure 4-5 (Exner 1979). In Exner's experiments, 20 large copper spheres were sintered at 1027 °C without any external force loading. In Figure 4-5, the relationship between neck radius / particle radius ratio ( $r/R$ ) and the relative center approach ( $[X_0 - X_N]/R$ ) (which is the ratio between the approaching of two particle centers and their original distance and is an indication of the shrinkage of the particle system) were presented. Simulation results agreed well with the experimental results, and the predicted trend of the evolution of shrinkage as a function of  $r/R$  matched well with the experimental observations.

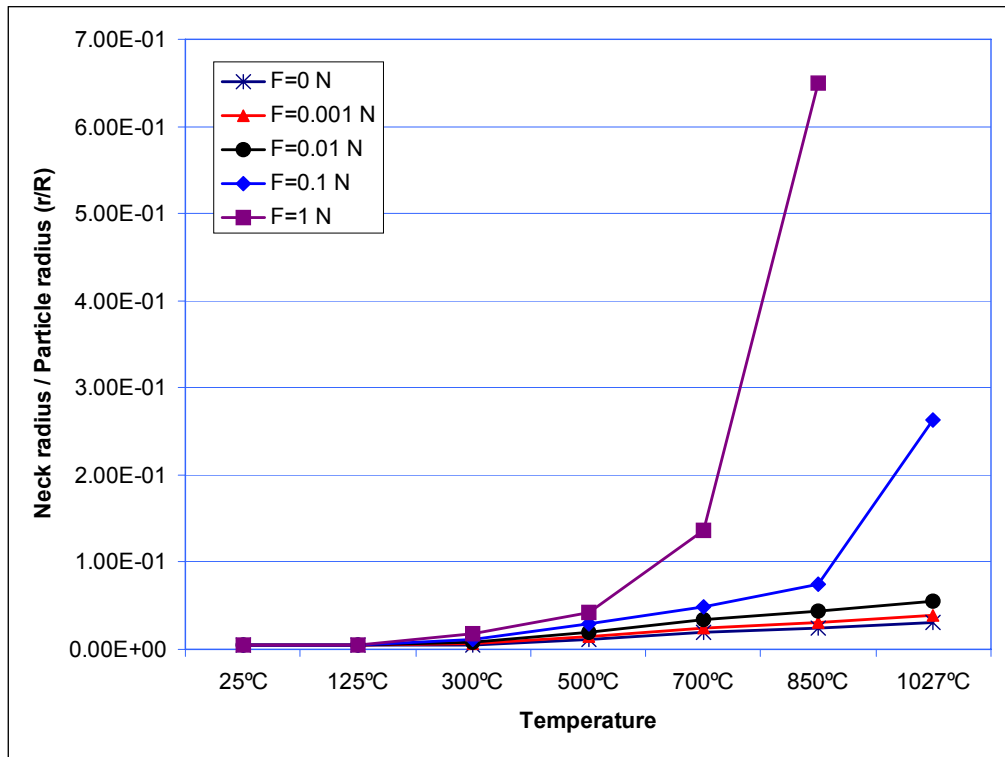


**Figure 4-5 Comparison between simulation and experiment results**

After validation, a further study of the pressure assisted sintering process was performed using the numerical model. Figure 4-6 shows the effects of temperature and compaction force on the pressure assisted sintering process. The following conclusions could be drawn from this figure:

1. The rate of neck growth is very low at a low temperature (25-150 °C), in which case neck does not grow much even if a compaction force is applied.
2. An external compression force significantly increases the neck growth rate at a higher temperature range (300-1000 °C), which is due to the fact that the material is softened in this temperature range. Especially in the

cases of 1N at 700 °C and 0.1N at 850 °C, there is a dramatic increase in the neck growth rate.



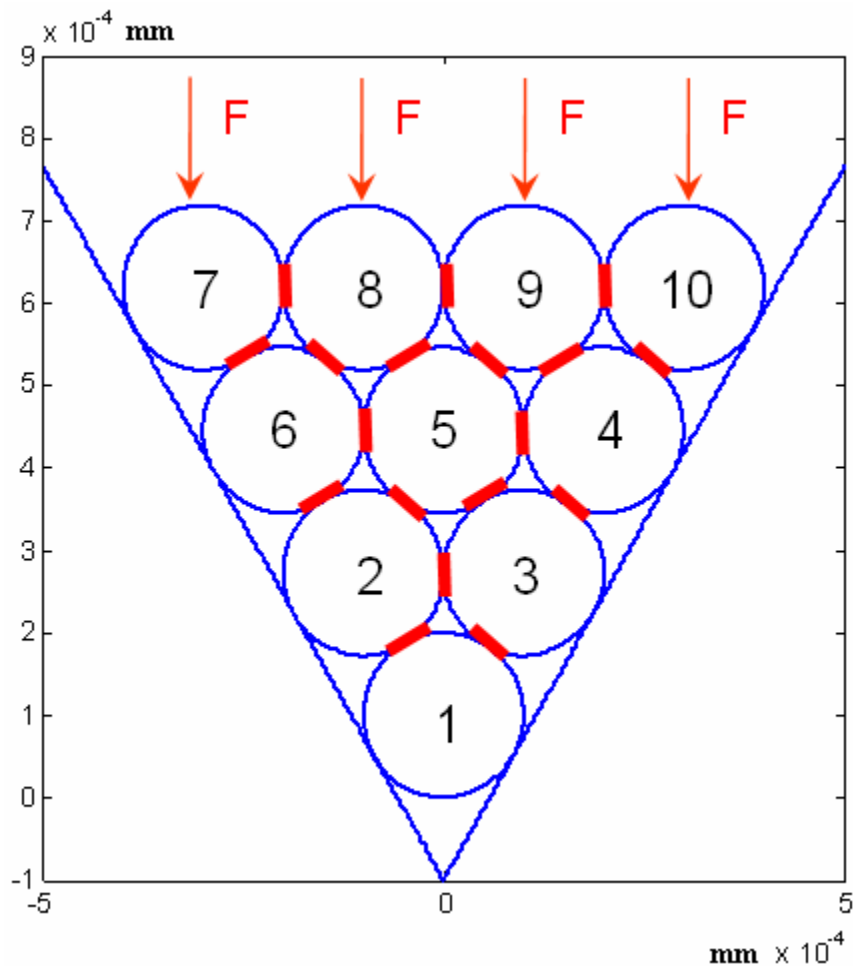
**Figure 4-6 Effects of temperature and force on  $r/R$**

### 4.3.3 Modeling of Multi-particle Problem with Boundary Conditions

The discrete element model for cold compaction developed by Cundall (Chapter 2) is based on the original particle dynamics, where contacts between particles are not sustained. It is not well-suited, however, for application where the contacts undergo large deformations and, once made, rarely break. In our case (hot compaction after pre-press), the particle assembly may be assumed to be in equilibrium at all stages of the process (Jagota and Dawson 1988), permitting solution for velocities implicitly, as discussed

below. Based on the study of Fleck and Heyliger (Fleck 1995; Heyliger and McMeeking 2001), shearing tractions between particles was neglected, which was found to play a minor role in the particle assembly, especially after pre-press.

Particle packings were treated as frameworks of links that connect the centers of particles through inter-particle contacts. The behavior of each link in the framework was based on unit problems for the interaction between individual spheres as described in the previous section.



**Figure 4-7 Illustration of the 10-particle model**



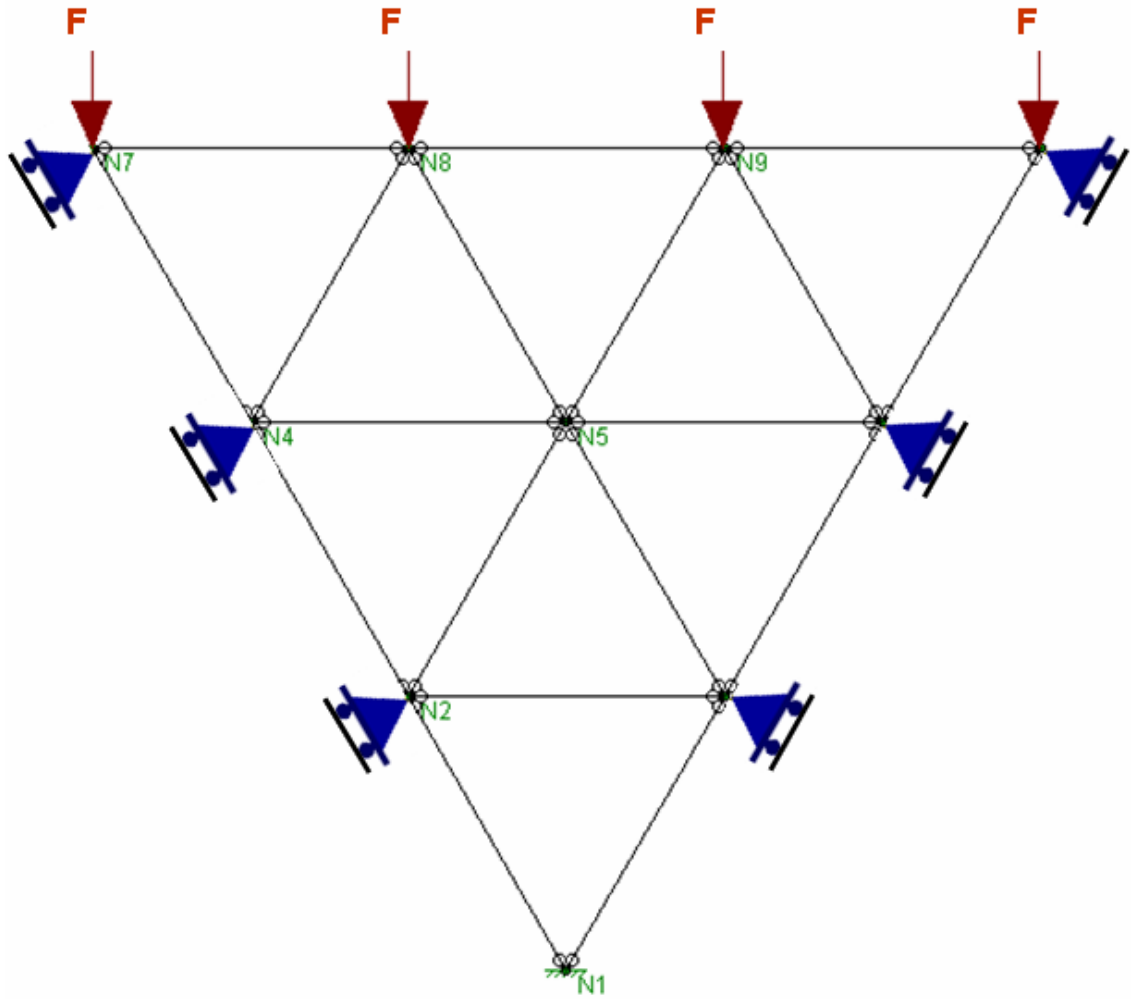
As shown in Figure 4-7, a network model for the pressure assisted sintering of ten particles in a V-shape channel was developed. The angle between two V-channel walls was 60°. The particle diameter was 200µm. Each particle was assigned a number as shown in Figure 4-7. Identical force was applied on particle 7, 8, 9 and 10 to account for the compression load.

#### 4.3.3.1 Frame Analysis of the Ten-particle System

As explained in previous discussions, the particle system was simplified as a framework of links in equilibrium. Thus, the interaction force between particles could be obtained by truss analysis (Jagota and Dawson 1988; Heyliger and McMeeking 2001). As shown in Figure 4-8, the frame analysis was carried out using RISA-3D (a structural engineering software). The obtained interaction force between particles is summarized in Table 4-3.

Particle A	Particle B	Axial Force	Particle A	Particle B	Axial Force
1	2	0.0074F	6	7	0.0523F
2	3	0.0059F	7	8	0
1	3	0.0074F	8	9	0.1293F
2	6	0.0015F	9	10	0
5	6	0.0012F	4	10	0.0523F
4	5	0.0012F	4	9	0.7492F
3	4	0.0015F	5	9	0.4055F
3	5	0.4055F	5	8	0.4055F
2	5	0.4055F	6	8	0.7492F

**Table 4-3 Axial interaction force between particles**



**Figure 4-8 Frame analysis of the ten-particle system**

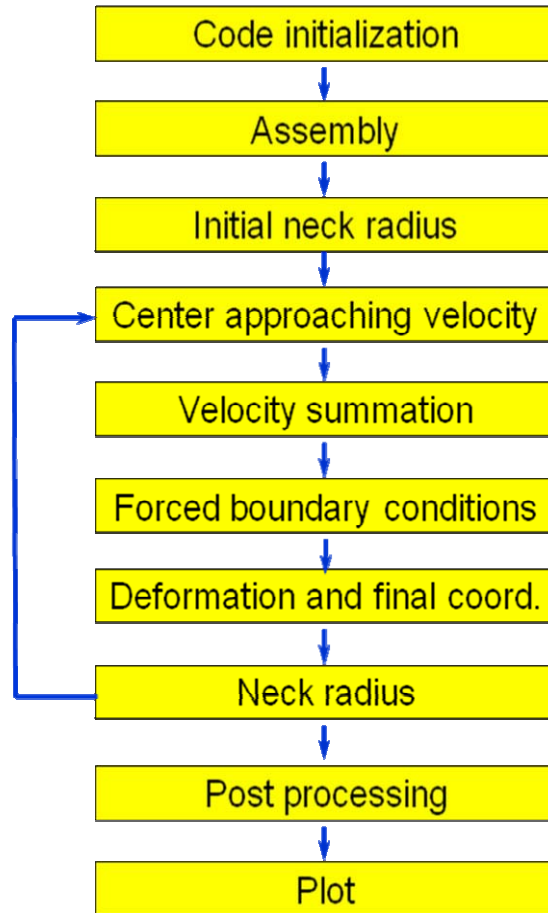
#### **4.3.3.2 Calculation Scheme for Multi-particle Pressure Assisted Sintering**

##### **Problem**

A code<sup>1</sup> was developed for this multi-particle pressure assisted sintering problem using MATLAB. The step-by-step computing structure of the code is shown in Figure 4-9.

---

<sup>1</sup> MATLAB codes are attached in Appendix.



**Figure 4-9 Calculation scheme for multi-particle pressure assisted sintering problem**

In the initialization step, constants such as material properties and temperature are defined. Geometry and dimension of the channel and particles are defined in the assembly step. The coordinates of the particles are first defined in global coordinates, and then transformed into local coordinates via rotation matrix for the ease of computational operation.

Before the hot compaction, the pre-pressed particles will have an initial neck radius due to elastic or plastic deformation, which could be solved using the original discrete element model as explained in *Chapter 2*. To roughly estimate the initial particle displacement and neck radius, the DEM scheme as shown in Figure 2-9 was used.

Equation 2-2 was used as force-displacement law. And the time step was approximated by Equation 2-3.

The subsequent five steps compose an iteration loop, which solves the pressure assisted sintering process continuously until a pre-defined sintering time is reached. The approaching velocity between every two contacting particles was calculated using Equation 4-8, which is stored in an approaching velocity matrix as shown in Equation 4-11.

$$Vn = \begin{bmatrix} Vn_{11} & Vn_{12} & \dots & Vn_{1n} \\ Vn_{21} & & & \\ \vdots & & & \\ Vn_{n1} & \dots\dots\dots & & Vn_{nn} \end{bmatrix} \quad (4-11)$$

where  $Vn_{ij}$  denotes approaching velocity on particle  $i$  caused by particle  $j$ . The matrix was constructed this way such that the absolute velocity of the particle could be assembled conveniently in the velocity summation step with only one matrix operation as shown in Equation 4-12.

$$V = \begin{bmatrix} Vn_{11} & Vn_{12} & \dots & Vn_{1n} \\ Vn_{21} & & & \\ \vdots & & & \\ Vn_{n1} & \dots\dots\dots & & Vn_{nn} \end{bmatrix} * \cos \begin{bmatrix} \theta_{11} & \theta_{12} & \dots & \theta_{1n} \\ \theta_{21} & & & \\ \vdots & & & \\ \theta_{n1} & \dots\dots\dots & & \theta_{nn} \end{bmatrix}' \quad (4-12)$$

where  $\theta_{ij}$  denotes the angle between local  $y$  axis (orthogonal to the axial direction) and the vector direction on particle  $i$  caused by particle  $j$ .

The displacement of each particle is updated using central finite difference method (Equation 4-10) with forced boundary conditions imposed by the V-channel as shown in Figure 4-8. At the end of each iteration, the neck radius is updated using equation 4-7. Post-processing step store and plot out data.

#### **4.3.3.3 Simulation Results and Discussions**

Simulations were run for the above problem with a force of 10N for 8 minutes of pressure assisted sintering at different temperatures. Each simulation took about 5 hours of computational time on a Sun Ultra 20 (1.8 GHz) workstation.

As shown in Figure 4-10, at an isothermal temperature setting (350 °C), the neck growth of different particle pairs were different. The growth of the neck was very rapid in the first 30 seconds, after which the growth slowed down dramatically and appeared as seemingly linear increase over the time. Depending on the axial interaction force between two particles, the size of the formed neck was different. Generally speaking, the higher the axial force, the larger the neck is. For example, the neck between particle 7 and particle 8 was the smallest, since the axial force between them is the lowest. However, the axial force between each given pair was not the only contributing factor; the interaction force caused by surrounding particles also affected the neck size. For example, the axial force between particle 6 and particle 8 was the highest, but their neck was not the largest. The largest neck occurred at particles 2 and 5 interface, which was more than twice the size of other necks. But its growth rate after the first 10 second was also the lowest comparing to other necks. A review of Equation 4-7 reveals that the neck growth rate is proportional to  $\frac{1}{r^3}$ , which results in a lower growth rate at a larger neck size.

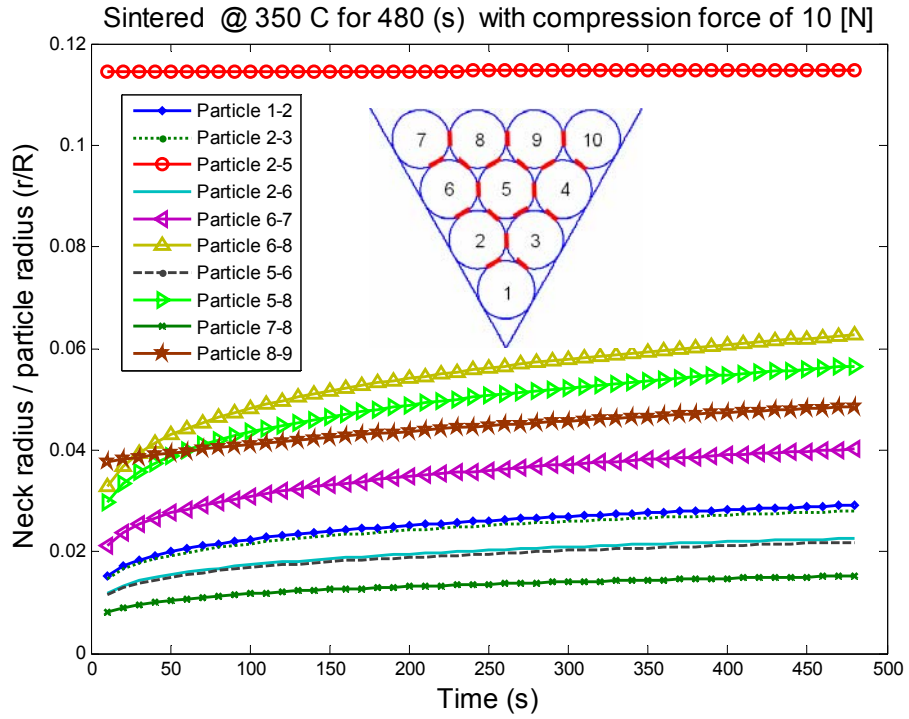


Figure 4-10 Neck radius during pressure assisted sintering (350 °C, 10N)

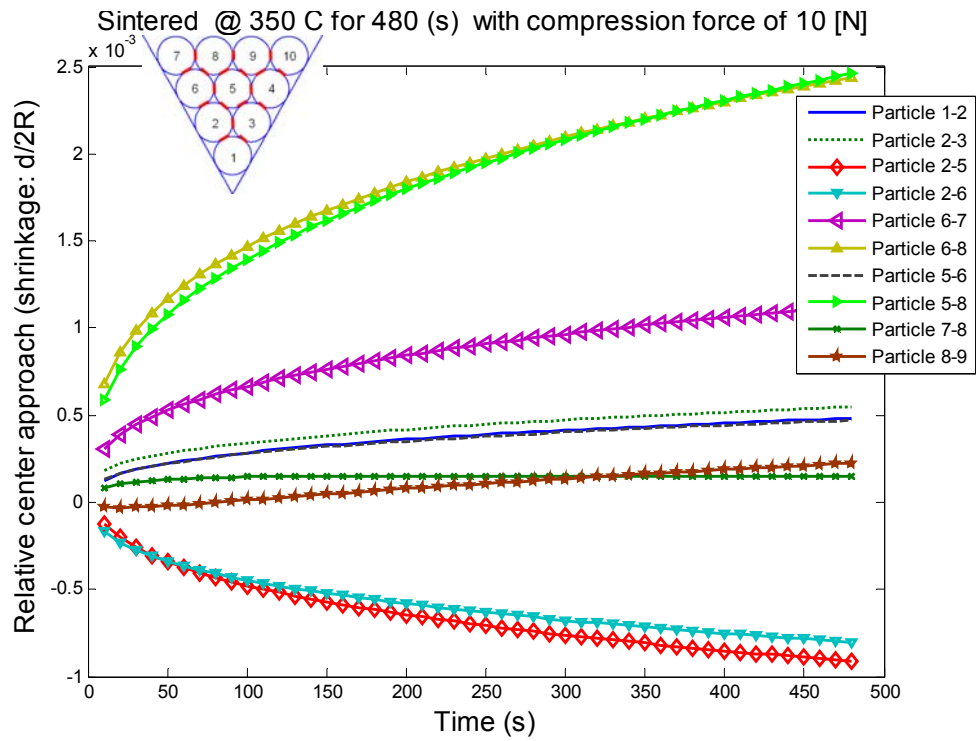


Figure 4-11 Relative center approaching (350 °C, 10N)

Figure 4-11 shows the relative center approach of the particles during pressure assisted sintering at 350 °C. Similarly to the neck growth, the lower the interaction force, the slower the approaching. While most particles were approaching each other, some particles were departing from others, as a result of the combined attraction forces from surrounding particles under an equilibrium condition. As shown in Figure 4-11, particles 2 and 3 have negative relative center approaching with particles 4, 5 and 6; meanwhile, particles 4, 5, 6, 7, 8, 9 and 10 have a relatively higher amount of center approaching, which is an indication that the tip region (particles 1, 2 and 3) does not shrink as much as the root area (4, 5 and 6) does. The micro-protrusion cross-sectional images from our experiments (Figure 3-12) indicates that the root region has a lower porosity than the tip region does, which is a match to the trend predicted by the relative center approaching plot (Figure 4-11).

Figures 4-12 and 4-13 show the neck growth of the network model at 384 °C and 422 °C. As the temperature increased, the neck size became larger. But the general growth trend remained the same.

Figures 4-14 and 4-15 show the relative center approach of the network model at 384 °C and 422 °C. As the temperature increased, the approaching speed increased. But the general growth trend remained the same.

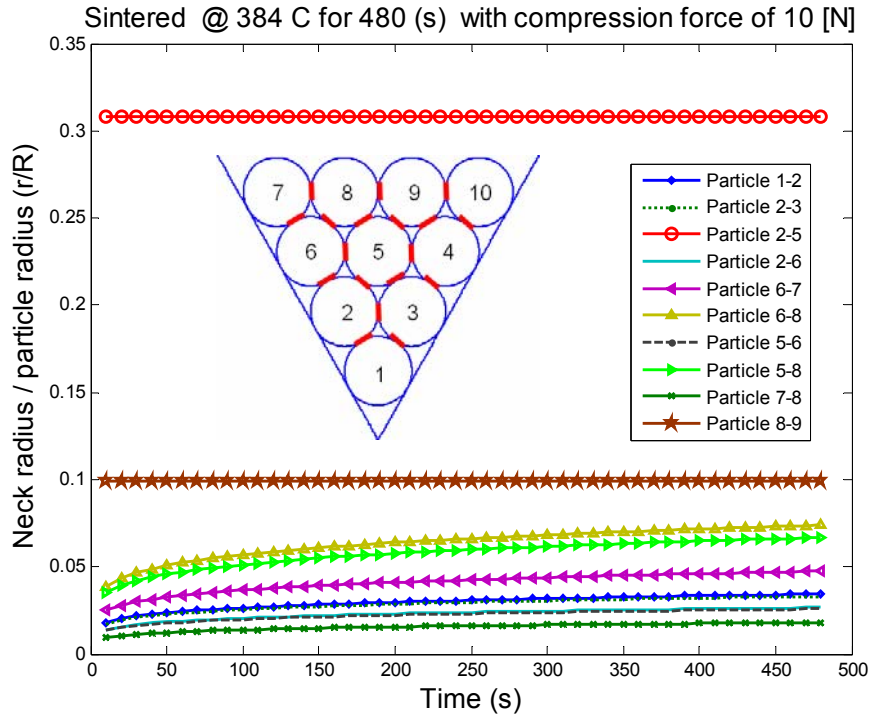


Figure 4-12 Neck radius during pressure assisted sintering (384 °C, 10N)

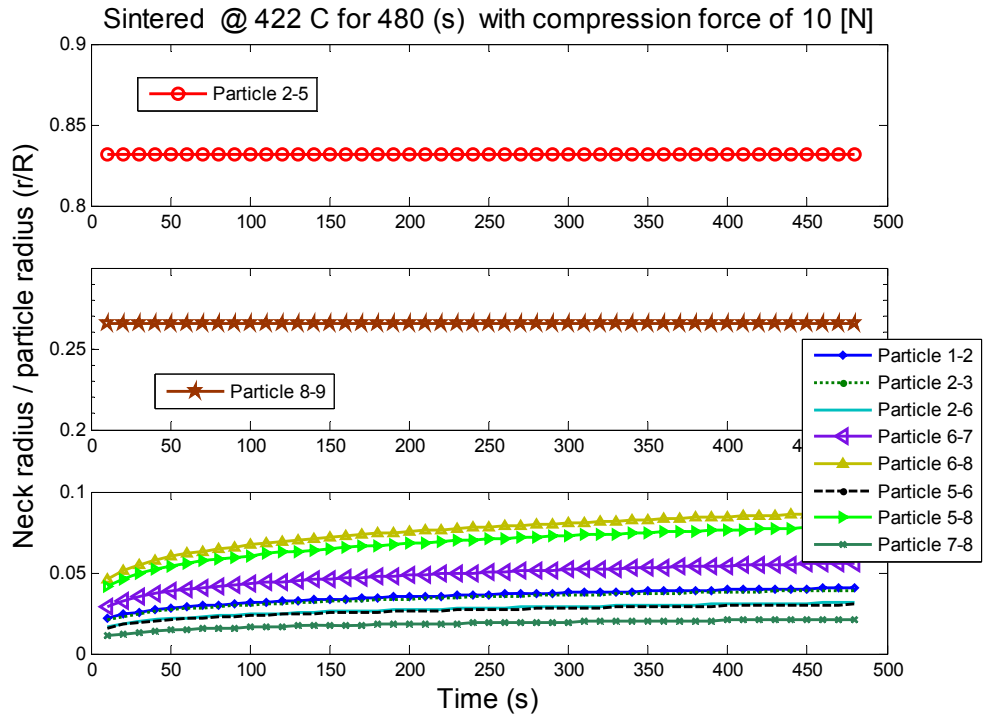
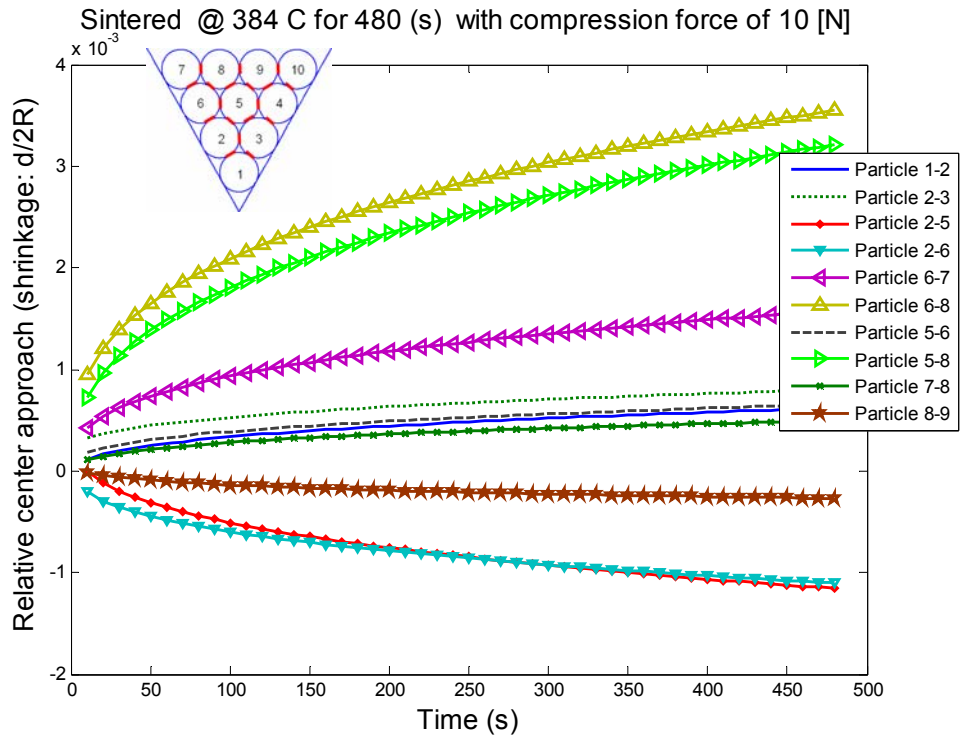
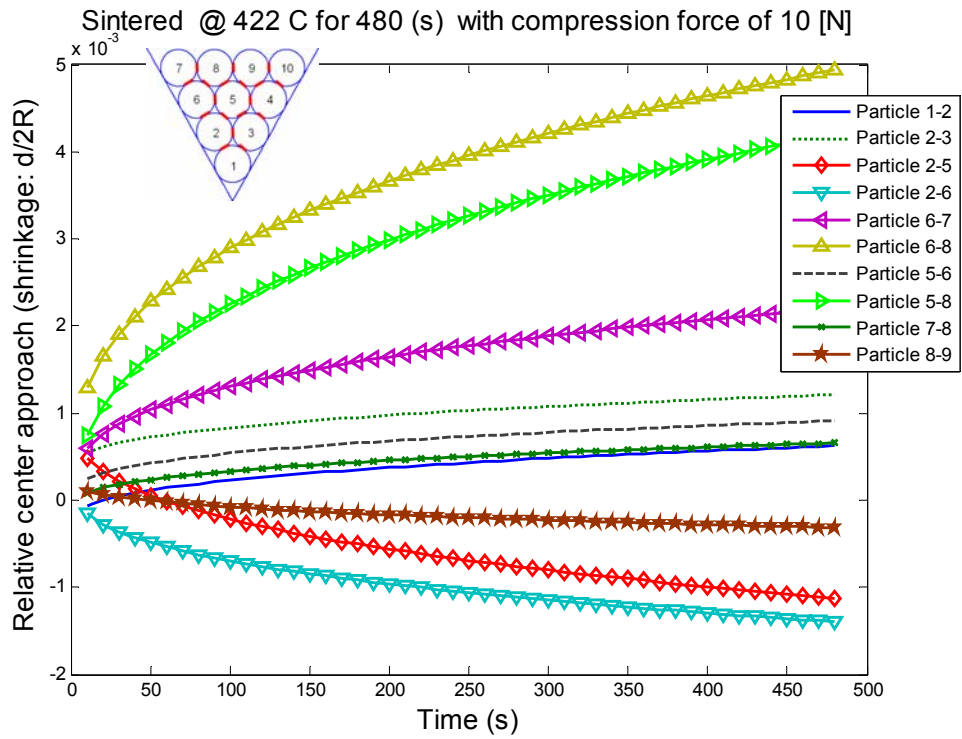


Figure 4-13 Neck radius during pressure assisted sintering (422 °C, 10N)





**Figure 4-14 Relative center approaching (384 °C, 10N)**



**Figure 4-15 Relative center approaching (422 °C, 10N)**

#### 4.4 Conclusions

A discrete element model for hot pressing was proposed, developed and showed a good agreement with experiments, which simulates the pressure assisted sintering process as a function of force, temperature and time. Under an equilibrium condition, the hot pressing process could be characterized as an atomic diffusion process, during which both heat-induced diffusion and pressure-induced diffusion took place. Since the hot compaction processing time is short in our case for the fabrication of porous micro-features, only the initial stage sintering is considered.

Comparing to the previous model developed by Parhami and McMeeking (Parhami and McMeeking 1994), our model takes into the consideration of temperature directly, so that the results is not only a function of pressure and time, but also a function of temperature. In addition, our numerical scheme takes into accounts of the boundary constraints imposed by the die wall, which is not included in previous models.

The pressure assisted sintering process was first modeled using a two particle unit problem and validated with experiments. And then this model was further extended and improved to handle a simplified closed die hot compaction problem. In the simulation, every particle center was represented by a node and every contact between neighboring particles by a link. The velocity of each node was related to applied and sintering forces arising from the deformation mechanisms which were physically active. These processes were controlled by grain boundary and surface diffusion and determined the constitutive laws for the behavior of each link. The contribution of each discrete link was then assembled into a system of equations that represented the behavior of the particle packing. To account for the effect of die, forced boundary conditions were applied to the outer

particles. The effects of temperature, sintering time and compression force on the neck radius and densification were studied using this model.

The rate of neck growth is very low at a low temperature (25-150 °C), in which case neck does not grow much even if a compaction force is applied. An external compression force significantly increases the neck growth rate in a higher temperature range (300-1000 °C), which is because that the material is softened in this temperature range. Especially in the cases of 1N at 700 °C and 0.1N at 850 °C, there is a big jump in the neck growth rate.

The growth of the neck was very rapid in the first 30 seconds, after which the growth slowed down dramatically and appeared as seemingly linear increase over the time. Depending on the axial interaction force between two particles, the size of the formed neck was different. Generally speaking, the higher the axial force, the larger the neck is. However, the axial force between each given pair was not the only contributing factor; the interaction force caused by surrounding particles also affected the neck size. The general porosity distribution predicted by this model matches the experimental results. As the temperature increased, both neck size and particle center approaching increased.

The numerical model developed in this study effectively captures the atomic diffusions caused by both pressure and heat, and provides means to extend this model for more particles with the consideration of boundary conditions.

## **CHAPTER 5**

### **SUMMARY AND CONTRIBUTIONS**

#### **5.1 Summary**

This research is a contribution to an on-going effort for the mass production of porous micro-features, with an emphasis on the applications for improved two-phase heat transfer. The feasibility of the proposed fabrication methods has been investigated through the experimental exploration and computational modeling.

##### **5.1.1 Forming of Porous Micro-features using Cold Compaction and Incomplete Sintering Method**

As a potential candidate for manufacturing parts with porous micro-scale features, a sequential cold compaction and incomplete sintering process was developed and investigated. Characteristics of micro-feature forming by this process have been investigated. Physical experiments were conducted to investigate the effects of compaction force and sintering process on the formation of porous micro-features. Cold compaction simulation was performed to study the density distribution during the formation of micro-features.

The capability of this process for the fabrication of porous micro-features was demonstrated, while its limitation was also discussed.

### **5.1.2 Forming of Porous Micro-features and Particle/Substrate Bonding using Hot Compaction**

A hot compaction process for the fabrication of micro-scale porous features with high aspect ratio was developed, which could be easily integrated into the existing manufacturing facilities. It was found this technique could overcome the limitations of the method used in the previous section. Thermal analysis of the system was carried out using finite element simulation. The effects of compaction force and temperature on the part quality were investigated. In addition, low thermal-resistant bonding between porous-layer and substrate could be obtained using this process.

### **5.1.3 Discrete Element Modeling of the Pressure Assisted Sintering Process**

Based on the models available in the literature, a new numerical model for hot pressing was proposed, which can simulate the pressure assisted sintering process as a function of force, temperature and time with the consideration of boundary conditions imposed by die. The effects of temperature and compression force on the neck radius and densification can be studied using this model, which is valuable for process developers, especially in the beginning stage.

## **5.2 Contributions**

The major contributions of the dissertation may be summarized as follows.

1. The possibility of producing porous micro-features with a good mechanical strength using uniaxial compaction/incomplete sintering process was demonstrated, which was the

first attempt in this research area. The major limitation of this process was found to be the low achievable aspect ratio. The effects of compaction and sintering processes on the formation of porous micro-features were analyzed in details, which would provide process design guidelines for the cold compaction/incomplete sintering technique. The density distribution of the formed micro-features was determined using a continuum powder finite element model.

2. Development and investigations on the hot compaction process showed a promising fabrication technique for the fabrication of porous micro-features with high aspect ratios, which was the first research attempt to use this technique for the manufacturing of micro-scale features with interconnected porous structure. The major advantages of this process were found to be high achievable aspect ratio and low taper angle. The effects of force and temperature on the quality of the formed micro-features were systematically studied using design of experiment, which would provide process design guidelines for the hot compaction process. Temperature history and distribution of the particle packing during hot compaction were determined based on a thermal finite element model.

3. The possibility of producing good bonding between porous layer and substrate was demonstrated. The bonds could sustain peeling and bending force. Microstructural analysis showed that bonding portion had a crystalline structure, which would yield a low thermal-resistant bonding when compared to other conventional bonding methods.

4. The numerical model developed for pressure assisted sintering of micro-features

provides engineers and scientists a convenient tool to study the effects of force, temperature and time on the quality of the formed micro-features.

### **5.3 Recommendations for the Future Work**

The dissertation investigated manufacturing of porous surface with micro-features. The following topics are recommended for the future work.

1. Transfer the knowledge learned from this study to continuous powder rolling process. Rolling equipment and process exist in the current industry. And the productivity of the rolling process is higher than that of the powder compaction process. Expected major challenges are: 1) powder feeder side constraints design for the continuous feeding; 2) sealing design for safety concerns; 3) design of the roller for the easy rejection of the formed part; and 4) computational modeling of the rolling process needs to take into accounts of large shear force.
2. Study the effects of the fabrication process variables on the heat transfer performance of the product directly by performing boiling heat transfer experiments. The porosity and shape of the pores in the formed micro-features are determined by the force and temperature setting used during fabrication, which will in turn affect its heat transfer performance in practical applications. By conducting boiling heat transfer experiments with the product, the optimal fabrication conditions can be determined. In addition, the durability of the product under actual boiling conditions needs to be tested.

3. Investigate the forming of porous features with smaller powders, even nanoparticles. With smaller particles, smaller features could be formed. The other advantage of smaller particles is that the particle bonding strength gets better as smaller particles improve atomic diffusions. And it would be interesting to conduct the same compaction with a different powder having a more uniform size distribution (after sieving), more regular shape (spherical), possibly gas atomized powder.

4. Investigate the feasibilities of the recently developed powder metallurgy techniques for the fabrication of porous micro-feature. Especially, a new technology called Laser Ablation of Microparticle Aerosol (LAMA) needs to be further investigated. A recent publication (Kovar et al. 2007) showed that this technology was used for producing patterns lines used in MEMS device sealing, which has a very similar feature to our studies.



## **APPENDIX**

## APPENDIX: Matlab Source Code for Discrete Element Model Simulation

```

%DEM_HC_10p: 10-particle model
clear;
format long;
%Pre-processing
%% Definition
R=10^(-4); % Particle radius (m)
T=460+273.15; % Absolute temperature
Psi=146*pi/180; % Dihedral angle
Rg=8.31; % Gas constant (J/mol)
Qb=105000; % Boundary Diffusion Activation energy (J/mol)
Db_Delta_0=5.12*10^(-15); % Maximum grain boundary diffusion coefficient
* effective grain boundary thickness(m^3/s)
Db_Delta=Db_Delta_0*exp(-Qb/Rg/T); % Boundary Diffusion
Omega=1.18*10^(-29); % Atomic volume (m^3)
k=1.38*10^(-23); % Boltzmann's constant (J/K)
Db=Db_Delta*Omega/k/T; % Effective grain boundary diffusivity
gamma=1.72; % Surface energy (J/m^2)
A=4*R*(1-cos(Psi/2));
B=sin(Psi/2);
Rho=8960; % Density (Kg/m^3)
m=Rho*(4*pi*R^3)/3; % Particle mass
theta=30*pi/180; % Taper angle (half)
E=113*10^9; % Young's modulus (Pa)
ke=0.733*E*((R/2)^(0.5)); % Elastic contact stiffness (Hertzian)
kf=0.722*10^9; % 2.97 * yield strength
kp=pi*R*kf; % Plastic contact stiffness
delta_p=R*2*(pi*kf/0.733/E)^2; % Critical deformation
cm=1; % Coefficient for neck radius during plastic

```

```

deformation
te=2*(m/ke)^0.5;
tp=2*(m/kp)^0.5;
%% Assembly definition
Gxy=[0 -0.1*10^(-3) 0.1*10^(-3) 0.2*10^(-3) 0 -0.2*10^(-3) -0.3*10^(-3) -0.1*10^(-3)
0.1*10^(-3) 0.3*10^(-3); 0.1*10^(-3) 0.2732*10^(-3) 0.2732*10^(-3) 0.4464*10^(-3)
0.4464*10^(-3) 0.4464*10^(-3) 0.6196*10^(-3) 0.6196*10^(-3) 0.6196*10^(-3)
0.6196*10^(-3)]; % Particle center coordinates matrix (Gx;Gy)
QQ=[cos(theta) sin(theta);-sin(theta) cos(theta)]; % Coordinate rotation matrix
PP=[cos(-theta) sin(-theta);-sin(-theta) cos(-theta)]; % Coordinate rotation
matrix QQrev=[cos(theta) -sin(theta);sin(theta) cos(theta)]; % Coordinate rotation
matrix
PPrev=[cos(-theta) -sin(-theta);sin(-theta) cos(-theta)];% Rotation matrix
PQ=[cos(2*theta) sin(2*theta);-sin(2*theta) cos(2*theta)]; % Rotation matrix
xy=QQ*Gxy; % Particle center coordinates matrix (x;y)
Pxy=PP*Gxy; % Particle center coordinates matrix (x';y')
%% Loading
F(7,7)=10;Fe=F(7,7);Q(7,7)=150*pi/180;P(7,7)=210*pi/180;F(8,8)=10;Q(8,8)=150*pi/180;
P(8,8)=210*pi/180;F(9,9)=10;Q(9,9)=150*pi/180; P(9,9)=210*pi/180; F(10,10)=10;
Q(10,10)=150*pi/180; P(10,10)=210*pi/180; % External force (xy,x'y'), Q: vector
angle with y
%% Step 0 (initialization)
Dt=5*10^(-9); % Time step (s)
%% Left half QQ
for u=1:10
    for v=1:10
        Qy(u,v)=cos(Q(u,v)); % Force projection matrix for y axis
        Qx(u,v)=cos(Q(u,v)+pi/2); % Force projection matrix for x axis
        m_inv(u,v)=1/m;
    end
end
ay=(F.*m_inv)*Qy'; % y accerelation
ax=(F.*m_inv)*Qx'; % x accerelation
vy=ay*Dt*0.5; % y velocity at half time increment
vx=ax*Dt*0.5; % x velocity at half time increment
sy=vy*Dt; % y displacement

```

```

sx=vx*Dt; % x displacement
dxy=[0 0 0 0 0 0 0 0 sx(8,8) sx(9,9) 0;0 0 0 0 0 0 0 sy(7,7) sy(8,8) sy(9,9)
sy(10,10)]; % Particle center displacement matrix (dxy)with BC applied (for
left half particles)
%%% Right half PP
for i=1:10
    for j=1:10
        Py(i, j)=cos(P(u, v)); % Force projection matrix for y' axis
        Px(i, j)=cos(P(u, v)+pi/2); % Force projection matrix for x' axis
    end
end
ayP=(F.*m_inv)*Py'; % y' accerelation
axP=(F.*m_inv)*Px'; % x' accerelation
vyP=ayP*Dt*0.5; % y' velocity at half time increment
vxP=axP*Dt*0.5; % x' velocity at half time increment
syP=vyP*Dt; % y' displacement
sxP=vxP*Dt; % x' displacement
d10=[0;syP(10,10)]; % Right particle 3 displacement increment in x'y'with BC
applied
d10xy=PQ*d10; % Rotation
dxy(:,10)=d10xy; % Particle center displacement matrix (xy)with BC applied
%%% Deformation and final coordinates
dGxy=QQrev*dxy; % Particle center displacement increment matrix (Gxy)with BC
applied
Gxy=Gxy+dGxy; % Updated particle center coordinates matrix (Gx;Gy)
xy=QQ*Gxy; % Particle center coordinates matrix (x;y)
Pxy=PP*Gxy; % Particle center coordinates matrix (x';y')
%%% Center approaching
for u=1:10
    for v=u+1:10
        CC(u, v)=((Gxy(1, v)-Gxy(1, u))^2+(Gxy(2, v)-Gxy(2, u))^2)^0.5; %
Particle center distance
    end
end
%%% Neck radius
for i=4

```

```

    for j=9:10
        nr(i, j)=(abs((R^2-(CC(i, j)/2)^2)))^(0.5);           % Neck radius
    end
end
for i=5
    for j=8:9
        nr(i, j)=(abs((R^2-(CC(i, j)/2)^2)))^(0.5);           % Neck radius
    end
end
for i=6
    for j=7:8
        nr(i, j)=(abs((R^2-(CC(i, j)/2)^2)))^(0.5);           % Neck radius
    end
end
for i=1
    for j=2:3
        nr(i, j)=1.0e-007;
    end
end
for i=2
    for j=5:6
        nr(i, j)=1.0e-007;
    end
end
nr(2, 3)=1.0e-007;
for i=3
    for j=4:5
        nr(i, j)=1.0e-007;
    end
end
nr(4, 5)=1.0e-007;
nr(5, 6)=1.0e-007;
nr(7, 8)=1.0e-007;
nr(8, 9)=1.0e-007;
nr(9, 10)=1.0e-007;
RCA120=(2*R-CC(1, 2))/R/2

```

```

RCA230=(2*R-CC(2,3))/R/2
RCA250=(2*R-CC(2,5))/R/2
RCA260=(2*R-CC(2,6))/R/2
RCA580=(2*R-CC(5,8))/R/2
RCA560=(2*R-CC(5,6))/R/2
RCA670=(2*R-CC(6,7))/R/2
RCA680=(2*R-CC(6,8))/R/2
RCA780=(2*R-CC(7,8))/R/2
RCA890=(2*R-CC(8,9))/R/2

%% Iteration
%initialization
F(1,2)=0.074;F(1,3)=0.074;F(2,3)=0.059;F(2,5)=4.056;F(2,6)=0.015;F(3,4)=0.015;F(3,
5)=4.056;F(4,5)=0.012;F(4,9)=7.492;F(4,10)=0.523;F(5,6)=0.012;F(5,8)=4.055;F(5,9)=
4.055;F(6,7)=0.523;F(6,8)=7.492;F(7,8)=0;F(8,9)=1.293;F(9,10)=0;
for i=1:10
    for j=i+1:10
        F(j,i)=F(i,j);
    end
end
Delta_t=10^(-5); % Time step (s)
N=6000000; NN=N; % Iteration cycle
Ts=Delta_t*N; % Processing time (s)
z=0;t=0;
while N>=1
    % Step 1 (approaching velocity)
    for i=1:10
        for j=i+1:10
            Vn(i,j)=abs((8*Db*(-F(i,j)/pi-gamma*(A+nr(i,j)*B))/(nr(i,j)^4));
        end
    end
    for i=1
        for j=4:10
            Vn(i,j)=0;
        end
    end
end
Vn(2,4)=0;

```

```

for i=2
    for j=7:10
        Vn(i, j)=0;
    end
end
for i=3
    for j=6:10
        Vn(i, j)=0;
    end
end
for i=4
    for j=6:8
        Vn(i, j)=0;
    end
end
Vn(5, 7)=0;
Vn(5, 10)=0;
for i=6
    for j=9:10
        Vn(i, j)=0;
    end
end
for i=7
    for j=9:10
        Vn(i, j)=0;
    end
end
Vn(8, 10)=0;
for i=1:10
    for j=i+1:10
        Vn(j, i)=Vn(i, j);
    end
end
for i=1:10
    for j=i+1:10

$$Q(i, j)=\text{acos}(\frac{((xy(1, i)-xy(1, j))*0+(xy(2, i)-xy(2, j))*1)}{(1)/((xy(1, i)-$$


```

```

xy(1, j))^2+(xy(2, i)-xy(2, j))^2)^0.5))-pi;
    if i==4
        if j==5
            Q(i, j)=-Q(i, j);
        end
    end
    if i==5
        if j==6
            Q(i, j)=-Q(i, j);
        end
    end
    end
    QX(i, j)=Q(i, j)+pi/2;    % Approaching velocity (on i caused by j) vector angle
with the x axis
    P(i, j)=Q(i, j)+pi/3;    % Approaching velocity (on i caused by j) vector angle
with the y' axis
    PX(i, j)=P(i, j)+pi/2;    % Approaching velocity (on i caused by j) vector angle
with the x' axis
    Q(j, i)=Q(i, j)+pi;
    QX(j, i)=QX(i, j)+pi;
    P(j, i)=P(i, j)+pi;
    PX(j, i)=PX(i, j)+pi;
    end
end
% Step 2 (Velocity summation)
for u=1:10
    for v=1:10
        Qy(u, v)=cos(Q(u, v));    % Projection matrix
        Qx(u, v)=cos(QX(u, v));    % Projection matrix
        Py(u, v)=cos(P(u, v));    % Projection matrix
        Px(u, v)=cos(PX(u, v));    % Projection matrix
    end
end
end
% Step 3 (velocity)
%% Left half
vy=Vn*Qy';    % y velocity
vx=Vn*Qx';    % x velocity

```



```

%% Right half
vyP=Vn*Py' ; % y' velocity
vxP=Vn*Px' ; % x' velocity
% Step 4 (displacement with forced boundary conditions)
%% Left half
sy=vy*Delta_t; % y displacement
sx=vx*Delta_t; % x displacement
if sx(2,2)<0
    sx(2,2)=0;
end
if sx(6,6)<0
    sx(6,6)=0;
end
if sx(7,7)<0
    sx(7,7)=0;
end
dxy=[sx(1,1) sx(2,2) sx(3,3) sx(4,4) sx(5,5) sx(6,6) sx(7,7) sx(8,8) sx(9,9)
sx(10,10);sy(1,1) sy(2,2) sy(3,3) sy(4,4) sy(5,5) sy(6,6) sy(7,7) sy(8,8) sy(9,9)
sy(10,10)]; % Particle center displacement matrix
(dxy)with BC applied (for left half particles)
%% Right half
syP=vyP*Delta_t; % y' displacement
sxP=vxP*Delta_t; % x' displacement
dxyP=[sxP(1,1) sxP(2,2) sxP(3,3) sxP(4,4) sxP(5,5) sxP(6,6) sxP(7,7) sxP(8,8)
sxP(9,9) sxP(10,10);syP(1,1) syP(2,2) syP(3,3) syP(4,4) syP(5,5) syP(6,6) syP(7,7)
syP(8,8) syP(9,9) syP(10,10)];
%% Deformation and final coordinates
dGxy=Qrev*dxy; % Particle center displacement increment matrix (Gxy)with BC
applied
dGxy(1,3)=-dGxy(1,2);
dGxy(2,3)=dGxy(2,2);
dGxy(1,4)=-dGxy(1,6);
dGxy(2,4)=dGxy(2,6);
dGxy(1,10)=-dGxy(1,7);
dGxy(2,10)=dGxy(2,7);
dGxy(1,9)=-dGxy(1,8);

```

```

dGxy(2,9)=dGxy(2,8);          % Forced symetry, eliminate numric error
Gxy=Gxy+dGxy; % Updated particle center coordinates matrix (Gx;Gy)
xy=QQ*Gxy; % Particle center coordinates matrix (x;y)
Pxy=PP*Gxy; % Particle center coordinates matrix (x';y')
% Step 5 (neck radius)
for i=1
    for j=2:3
        Vr(i,j)=8*R*Db*(abs(F(i,j))/pi+gamma*(A+nr(i,j)*B))/(nr(i,j)^5); %
Neck growth rate ij
        nr(i,j)=nr(i,j)+Vr(i,j)*Delta_t; % Neck radius ij
        nr(j,i)=nr(i,j);
        Vr(j,i)=Vr(i,j);
    end
end
for i=2
    for j=3
        Vr(i,j)=8*R*Db*(abs(F(i,j))/pi+gamma*(A+nr(i,j)*B))/(nr(i,j)^5); %
Neck growth rate ij
        nr(i,j)=nr(i,j)+Vr(i,j)*Delta_t; % Neck radius ij
        nr(j,i)=nr(i,j);
        Vr(j,i)=Vr(i,j);
    end
end
for i=2
    for j=5:6
        Vr(i,j)=8*R*Db*(abs(F(i,j))/pi+gamma*(A+nr(i,j)*B))/(nr(i,j)^5); %
Neck growth rate ij
        nr(i,j)=nr(i,j)+Vr(i,j)*Delta_t; % Neck radius ij
        nr(j,i)=nr(i,j);
        Vr(j,i)=Vr(i,j);
    end
end
for i=3
    for j=4:5
        Vr(i,j)=8*R*Db*(abs(F(i,j))/pi+gamma*(A+nr(i,j)*B))/(nr(i,j)^5); %
Neck growth rate ij

```

```

        nr(i, j)=nr(i, j)+Vr(i, j)*Delta_t;           % Neck radius ij
        nr(j, i)=nr(i, j);
        Vr(j, i)=Vr(i, j);
    end
end
for i=4
    for j=5
        Vr(i, j)=8*R*Db*(abs(F(i, j))/pi+gamma*(A+nr(i, j)*B))/(nr(i, j)^5); %
Neck growth rate ij
        nr(i, j)=nr(i, j)+Vr(i, j)*Delta_t;           % Neck radius ij
        nr(j, i)=nr(i, j);
        Vr(j, i)=Vr(i, j);
    end
end
for i=4
    for j=9:10
        Vr(i, j)=8*R*Db*(abs(F(i, j))/pi+gamma*(A+nr(i, j)*B))/(nr(i, j)^5); %
Neck growth rate ij
        nr(i, j)=nr(i, j)+Vr(i, j)*Delta_t;           % Neck radius ij
        nr(j, i)=nr(i, j);
        Vr(j, i)=Vr(i, j);
    end
end
for i=5
    for j=6
        Vr(i, j)=8*R*Db*(abs(F(i, j))/pi+gamma*(A+nr(i, j)*B))/(nr(i, j)^5); %
Neck growth rate ij
        nr(i, j)=nr(i, j)+Vr(i, j)*Delta_t;           % Neck radius ij
        nr(j, i)=nr(i, j);
        Vr(j, i)=Vr(i, j);
    end
end
for i=5
    for j=8:9
        Vr(i, j)=8*R*Db*(abs(F(i, j))/pi+gamma*(A+nr(i, j)*B))/(nr(i, j)^5); %
Neck growth rate ij

```

```

        nr(i, j)=nr(i, j)+Vr(i, j)*Delta_t;           % Neck radius ij
        nr(j, i)=nr(i, j);
        Vr(j, i)=Vr(i, j);
    end
end
for i=6
    for j=7:8
        Vr(i, j)=8*R*Db*(abs(F(i, j))/pi+gamma*(A+nr(i, j)*B))/(nr(i, j)^5); %
Neck growth rate ij
        nr(i, j)=nr(i, j)+Vr(i, j)*Delta_t;           % Neck radius ij
        nr(j, i)=nr(i, j);
        Vr(j, i)=Vr(i, j);
    end
end
for i=7:9
    for j=i+1
        Vr(i, j)=8*R*Db*(abs(F(i, j))/pi+gamma*(A+nr(i, j)*B))/(nr(i, j)^5); %
Neck growth rate ij
        nr(i, j)=nr(i, j)+Vr(i, j)*Delta_t;           % Neck radius ij
        nr(j, i)=nr(i, j);
        Vr(j, i)=Vr(i, j);
    end
end
for i=1:10
    Vr(i, i)=0;
    nr(i, i)=0;
end
% Step 6 (Center approaching)
for u=1:10
    for v=u+1:10
        CC(u, v)=((Gxy(1, v)-Gxy(1, u))^2+(Gxy(2, v)-Gxy(2, u))^2)^0.5;
% Particle center distance
    end
end
% Step 7 (Time control)
N=N-1;

```

```

% Step 8 (Data sampling)
z=z+1;
if z==1000000
    t=1+t;
    rR12(t)=nr(1,2)/R;
    rR23(t)=nr(2,3)/R;
    rR26(t)=nr(2,6)/R;
    rR25(t)=nr(2,5)/R;
    rR67(t)=nr(6,7)/R;
    rR68(t)=nr(6,8)/R;
    rR56(t)=nr(5,6)/R;
    rR58(t)=nr(5,8)/R;
    rR78(t)=nr(7,8)/R;
    rR89(t)=nr(8,9)/R;
    RCA12(t)=(2*R-CC(1,2))/R/2;
    RCA23(t)=(2*R-CC(2,3))/R/2;
    RCA25(t)=(2*R-CC(2,5))/R/2;
    RCA26(t)=(2*R-CC(2,6))/R/2;
    RCA58(t)=(2*R-CC(5,8))/R/2;
    RCA56(t)=(2*R-CC(5,6))/R/2;
    RCA67(t)=(2*R-CC(6,7))/R/2;
    RCA68(t)=(2*R-CC(6,8))/R/2;
    RCA78(t)=(2*R-CC(7,8))/R/2;
    RCA89(t)=(2*R-CC(8,9))/R/2;
    z=0;
end
end
%% Post-processing
% Shape plot
%%% Shape before processing
%%%% Definition of particle 1 (lower one)
X1=-R:0.1*10^(-7):R; % Horizontal coordinate
Y1U=R-(R^2-X1.^2).^0.5; % Upper section
Y1L=R+(R^2-X1.^2).^0.5; % Lower section
%%%% Definition of particle 2 (upper left)
X2=X1-R;

```

```

Y2U=Y1U+1.732*10(-4);
Y2L=Y1L+1.732*10(-4);
%%% Definition of particle 3 (upper right)
X3=X1+R;
Y3U=Y2U;
Y3L=Y2L;
%%% Definition of particle 4 (lower one)
X4=X1+2*R;
Y4U=Y1U+3.464*10(-4);
Y4L=Y1L+3.464*10(-4);
%%% Definition of particle 5 (upper left)
X5=X1;
Y5U=Y4U;
Y5L=Y4L;
%%% Definition of particle 6 (upper right)
X6=X1-2*R;
Y6U=Y4U;
Y6L=Y4L;
%%% Definition of particle 7 (lower one)
X7=X1-3*R;
Y7U=Y1U+5.196*10(-4);
Y7L=Y1L+5.196*10(-4);
%%% Definition of particle 8 (upper left)
X8=X1-R;
Y8U=Y7U;
Y8L=Y7L;
%%% Definition of particle 9 (upper right)
X9=X1+R;
Y9U=Y7U;
Y9L=Y7L;
%%% Definition of particle 10 (lower one)
X10=X1+3*R;
Y10U=Y7U;
Y10L=Y7L;
%%% Definition of die wall
XWR=0:0.1*10(-7):5*R;

```

```

YW=tan(pi/2-theta)*XWR-R;
XWL=-XWR;
%%% Plot
figure(1);
subplot
subplot(1, 2, 1);
plot(X1, Y1U, 'b', X1, Y1L, 'b', X2, Y2U, 'b', X2, Y2L, 'b', X3, Y3U, 'b', X3, Y3L, 'b', X4, Y4L, 'b',
X5, Y5L, 'b', X6, Y6L, 'b', X7, Y7L, 'b', X8, Y8L, 'b', X9, Y9L, 'b', X10, Y10L, 'b', X4, Y4U, 'b', X5,
Y5U, 'b', X6, Y6U, 'b', X7, Y7U, 'b', X8, Y8U, 'b', X9, Y9U, 'b', X10, Y10U, 'b', XWR, YW, 'b',
XWL, YW, 'b', 'linewidth', 2);
title([' Before hot compaction'], 'fontsize', 13);
%%% Shape after processing
%%% Definition of particle 2
HCX2=(Gxy(1, 2)-R):0.1*10^(-7):(Gxy(1, 2)+R);
HCY2U=Gxy(2, 2)-(abs((HCX2-Gxy(1, 2)).^2-R^2)).^0.5;
HCY2L=Gxy(2, 2)+(abs((HCX2-Gxy(1, 2)).^2-R^2)).^0.5;
%%% Definition of particle 3
HCX3=(Gxy(1, 3)-R):0.1*10^(-7):(Gxy(1, 3)+R);
HCY3U=Gxy(2, 3)-(abs((HCX3-Gxy(1, 3)).^2-R^2)).^0.5;
HCY3L=Gxy(2, 3)+(abs((HCX3-Gxy(1, 3)).^2-R^2)).^0.5;
%%% Definition of particle 4
HCX4=(Gxy(1, 4)-R):0.1*10^(-7):(Gxy(1, 4)+R);
HCY4U=Gxy(2, 4)-(abs((HCX4-Gxy(1, 4)).^2-R^2)).^0.5;
HCY4L=Gxy(2, 4)+(abs((HCX4-Gxy(1, 4)).^2-R^2)).^0.5;
%%% Definition of particle 5
HCX5=(Gxy(1, 5)-R):0.1*10^(-7):(Gxy(1, 5)+R);
HCY5U=Gxy(2, 5)-(abs((HCX5-Gxy(1, 5)).^2-R^2)).^0.5;
HCY5L=Gxy(2, 5)+(abs((HCX5-Gxy(1, 5)).^2-R^2)).^0.5;
%%% Definition of particle 6
HCX6=(Gxy(1, 6)-R):0.1*10^(-7):(Gxy(1, 6)+R);
HCY6U=Gxy(2, 6)-(abs((HCX6-Gxy(1, 6)).^2-R^2)).^0.5;
HCY6L=Gxy(2, 6)+(abs((HCX6-Gxy(1, 6)).^2-R^2)).^0.5;
%%% Definition of particle 7
HCX7=(Gxy(1, 7)-R):0.1*10^(-7):(Gxy(1, 7)+R);
HCY7U=Gxy(2, 7)-(abs((HCX7-Gxy(1, 7)).^2-R^2)).^0.5;
HCY7L=Gxy(2, 7)+(abs((HCX7-Gxy(1, 7)).^2-R^2)).^0.5;

```

```

%%%% Definition of particle 8
HCX8=(Gxy(1,8)-R):0.1*10^(-7):(Gxy(1,8)+R);
HCY8U=Gxy(2,8)-(abs((HCX8-Gxy(1,8)).^2-R^2)).^0.5;
HCY8L=Gxy(2,8)+(abs((HCX8-Gxy(1,8)).^2-R^2)).^0.5;
%%%% Definition of particle 9
HCX9=(Gxy(1,9)-R):0.1*10^(-7):(Gxy(1,9)+R);
HCY9U=Gxy(2,9)-(abs((HCX9-Gxy(1,9)).^2-R^2)).^0.5;
HCY9L=Gxy(2,9)+(abs((HCX9-Gxy(1,9)).^2-R^2)).^0.5;
%%%% Definition of particle 10
HCX10=(Gxy(1,10)-R):0.1*10^(-7):(Gxy(1,10)+R);
HCY10U=Gxy(2,10)-(abs((HCX10-Gxy(1,10)).^2-R^2)).^0.5;
HCY10L=Gxy(2,10)+(abs((HCX10-Gxy(1,10)).^2-R^2)).^0.5;
%%%% Plot
subplot
subplot(1,2,2);
plot(X1,Y1U,'b',X1,Y1L,'b',HCX2,HCY2U,'b',HCX2,HCY2L,'b',HCX3,HCY3U,'b',HCX3,HCY3L,
,'b',HCX4,HCY4U,'b',HCX5,HCY5U,'b',HCX6,HCY6U,'b',HCX7,HCY7U,'b',HCX8,HCY8U,'b',HC
X9,HCY9U,'b',HCX10,HCY10U,'b',HCX4,HCY4L,'b',HCX5,HCY5L,'b',HCX6,HCY6L,'b',HCX7,HC
Y7L,'b',HCX8,HCY8L,'b',HCX9,HCY9L,'b',HCX10,HCY10L,'b',XWR,YW,'b',
XWL,YW,'b','linewidth',2);
title([' After hot compaction'],'fontsize',13);
plot(x11,y11,'b',x12,y12,'b',x13,y13,'b',x21,y21,'b',x22,y22,'b',x23,y23,'b','line
width',2);
% hold on;
% plot(x14,y14,'r','linewidth',15);
% hold off;
title(['Shape after processing'],[' [sintered ', @ ', num2str(T-273.15), ' C for
', num2str(Ts), ' (s) ', ' with compression force of ', num2str(Fe), '
N]']'],'fontsize',14);
%%%% Plot
figure(2);
for i=1:48
    tt(i)=i*10
end
plot(tt,rR12,tt,rR23,tt,rR25,tt,rR26,tt,rR67,tt,rR68,tt,rR56,tt,rR58,tt,rR78,tt,rR
89,'linewidth',2);

```



```

title(['Sintered ', ' @ ', num2str(T-273.15), ' C for ', num2str(Ts), ' (s) ', ' with
compression force of ', num2str(Fe), ' [N]'], 'fontsize', 14);
legend('Particle 1-2', 'Particle 2-3', 'Particle 2-5', 'Particle 2-6', 'Particle 6-
7', 'Particle 6-8', 'Particle 5-6', 'Particle 5-8', 'Particle 7-8', 'Particle 8-9');
xlabel(['Time (s)'], 'fontsize', 14);
ylabel(['Neck radius / particle radius (r/R)'], 'fontsize', 14);
figure(3);
plot(tt, RCA12, tt, RCA23, tt, RCA25, tt, RCA26, tt, RCA67, tt, RCA68, tt, RCA56, tt, RCA58, tt, RC
A78, tt, RCA89, 'linewidth', 2);
title(['Sintered ', ' @ ', num2str(T-273.15), ' C for ', num2str(Ts), ' (s) ', ' with
compression force of ', num2str(Fe), ' [N]'], 'fontsize', 14);
legend('Particle 1-2', 'Particle 2-3', 'Particle 2-5', 'Particle 2-6', 'Particle 6-
7', 'Particle 6-8', 'Particle 5-6', 'Particle 5-8', 'Particle 7-8', 'Particle 8-9');
xlabel(['Time (s)'], 'fontsize', 14);
ylabel(['Relative center approach (shrinkage: d/2R)'], 'fontsize', 14);

```

## **BIBLIOGRAPHY**

## BIBLIOGRAPHY

- Afgan, N. H., Jovic, L. A., Kovalev, S. A., and Lenykov, V. A., "Boiling heat transfer from surfaces with porous layers," *International Journal of Heat and Mass Transfer*, vol. 28, no. 2, pp. 415–422, 1985.
- Arakawa, M., and Yasuda, S., "The measurement of interaction force on microparticles," *Journal of the Society of Materials Science*, vol. 26, no. 288, pp. 858-862, 1977 (in Japanese).
- Arzt, E., "The influence of an increasing particle coordination on the densification of spherical powders," *Acta Metallurgica*, vol. 30, no. 10, pp. 1883-1890, 1982.
- Banhart, J., "Manufacture, characterization and application of cellular metals and metal foams," *Progress in Materials Sciences*, vol. 46, pp. 559-632, 2001.
- Banhart, J., "Manufacturing routes for metallic foams," *JOM Journal of the Minerals, Metals and Materials Society*, vol. 52, no. 12, pp. 22-27, 2000.
- Bergles, A. E., and Chyu, M. C., "Characteristics of nucleate pool boiling from porous metallic coatings," *Transactions of the ASME. Journal of Heat Transfer*, vol. 104, no. 2, pp. 279-285, 1982.
- Boomsma, K., Poulidakos, D., and Zwick, F., "Metal foams as compact high performance heat exchangers," *Mechanics of Materials*, vol. 35, pp. 1161-1176, 2003.
- Bose, A., "Review of current and advanced hot densification processes," *Advances in Powder Metallurgy and Particulate Materials*, vol. 2, pp. 5259-5273, 1996.
- Cameron, I. M., and Gethin, D. T., "Exploration of die wall friction for powder compaction using a discrete finite element modeling technique," *Modelling and Simulation in Materials Science and Engineering*, vol. 9, pp. 289-307, 2001.
- Chang, J. Y., and You, S.M., "Enhanced boiling heat transfer from micro-porous surfaces: effects of a coating composition and method," *International Journal of Heat and Mass Transfer*, vol. 40, no. 18, pp. 4449-4460, 1997.

- Chen, P., Koc, M., and Ni, J., "Manufacturing of porous coatings with micro-scale features for improved boiling heat transfer," *Proceedings of MSEC2006, 2006 ASME International Conference on Manufacturing Science and Engineering*, pp. 117-122, 2006.
- Chen, P., Kim, G. Y., and Ni, J., "Fabrication of high aspect ratio porous micro-features using hot compaction technique," *Journal of Manufacturing Science and Engineering*, accepted, 2007.
- Chen, P., and Ni, J., "Discrete element modeling of micro-feature hot compaction process," *Transactions of the North American Manufacturing Research Institution/SME*, vol. 36, accepted, 2008.
- Cocks, A. C. F., "Constitutive modelling of powder compaction and sintering," *Progress in Materials Science*, vol. 46, no. 3-4, pp. 201-229, 2001.
- Coube, O., Cocks, A. C. F., and Wu, C. -Y., "Experimental and numerical study of die filling, powder transfer and die compaction," *Powder Metallurgy*, vol. 48, no. 1, pp. 68-76, 2005.
- Cundall, P. A., and Strack, O. D. L., "A discrete numerical model for granular assemblies," *Géotechnique*, vol. 29, no. 1, pp. 47-65, 1979.
- Dahl, M. M., and Erb, L. D., "Liquid heat exchanger interface and method," *U.S. patent 3,990,862*, November 9, 1976.
- Davies, G. J., and Zhen, S., "Review metallic foams: their production, properties and applications," *Journal of Materials Sciences*, vol. 18, pp. 1899-1911, 1983.
- Delo, D. P., Dutton, R. E., Semiatin, S. L., and Piehler, H. R., "Modeling of hot isostatic pressing and hot triaxial compaction of Ti-6Al-4V powder," *Acta Materialia*, vol. 47, no. 11, pp. 3159-3167, 1999.
- DOE Fundamentals Handbook, *Thermodynamics Heat Transfer and Fluid Flow, Module 2, Heat Transfer*, Washington D. C., 1992.

- Drucker, D. C., Gibson, R. E., and Henkel, D. J., "Soil mechanics and work hardening theories of plasticity," *Transaction of the American Society of Civil Engineers*, vol. 122, pp. 338-346, 1957.
- Exner, H. E., "Principles of single phase sintering," *Reviews on powder metallurgy and physical ceramics*, vol. 1, pp. 11-251, 1979.
- Fitzroy, N. D., *Heat Transfer Data Book*, General Electric Company, 1970.
- Fleck, N. A. , "On the cold compaction of powders," *Journal of the Mechanics and Physics of Solids*, vol. 43, no. 9, pp. 1409-1431, 1995.
- Fujii, M., Nishiyama, E., and Yamanaka, G., "Nucleate pool boiling heat transfer from micro-porous heating surface," *Advances in Enhanced Heat transfer*, pp. 45-51, ASME, New York, 1979.
- Geindreau, C., Bouvard, D., and Doremus, P., "Constitutive behaviour of metal powder during hot forming. Part II: Unified viscoplastic modelling," *European Journal of Mechanics - A/Solids*, vol. 18, no. 4, pp. 597-615, 1999.
- German, R. M., "Computer modeling of sintering processes," *International Journal of Powder Metallurgy (Princeton, New Jersey)*, vol. 38, no. 2, pp. 48-66, 2002.
- German, R. M., and Lathrop, J. F., "Simulation of spherical powder sintering by surface diffusion," *Journal of Materials Science*, vol. 13, pp. 921-929, 1978.
- German, R. M., *Powder Metallurgy Science*, Princeton, New Jersey, 1994.
- German, R. M., *Sintering theory and practice*, Wiley, New York, 1996.
- Gethin, D. T., Ransing, R. S., Lewis, R. W., Dutko, M., and Crook, A. J. L., "Numerical comparison of a deformable discrete element model and an equivalent continuum analysis for the compaction of ductile porous material," *Computers & Structures*, vol. 79, no. 13, pp. 1287-1294, 2001.

- Green, R. J., "Plasticity theory for porous solids," *International Journal of Mechanical Science*, vol. 14, no. 4, pp. 215-224, 1972.
- Gurson, A. L., "Continuum theory of ductile rupture by void nucleation and growth: Part I Yield criteria and flow rules for porous ductile media," *Journal of Engineering Materials and Technology, ASME*, vol. 99, no. 1, pp. 2-15, 1977.
- Haack, D. P., Butcher, K. R., Kim, T., and Lu, T. J., "Novel lightweight metal foam heat exchangers," *Proceedings of International Mechanical Engineering Congress and Exposition*, vol. 6, pp. 141-147, 2001.
- Hassold, G. N., Chen, I., and Srolovitz, D. J., "Computer Simulation of Final-Stage Sintering: I, Model Kinetics, and Microstructure," *Journal of the American Ceramic Society*, vol. 73, no. 10, pp. 2857-2864, 1990.
- Heyes, D. M., *The Liquid State: Applications of Molecular Simulations*, Wiley, England, 1998.
- Heyliger, P. R., and McMeeking, R. M., "Cold plastic compaction of powders by a network model," *Journal of the Mechanics and Physics of Solids*, vol. 49, no. 9, pp. 2031-2054, 2001.
- Hibbitt, D., Karlsson, B., and Sorensen, P., *ABAQUS theory manual*, version 5.4, Pawtucket, Rhode Island, 1994.
- Holman, P., *Heat Transfer*, 8th ed., McGraw-Hill Companies, New York, 1997.
- Hwang, K-S., and German, R. M., "Analysis of initial stage sintering by computer simulation," *Sintering and Heterogeneous Catalysis*, G. C. Kuczynski, A. E. Miller and G. A. Sargent (eds.), Plenum Press, New York, NY, pp. 35-47, 1984.
- Incropera, F. P., and Dewitt, D. P., *Fundamentals of Heat and Mass Transfer*, 4th ed., Wiley, New York 1996.

- Jagota, A., and Dawson, P. R., "Micromechanical modeling of powder compacts-I. unit problems for sintering and traction induced deformation," *Acta Metallurgica*, vol. 36, no. 9, pp. 2551-2561, 1988.
- Jagota, A., and Dawson, P. R., "Micromechanical modeling of powder compacts-II. truss formulation of discrete packings," *Acta Metallurgica*, vol. 36, no. 9, pp. 2563-2573, 1988.
- James, W. B., "Powder forging," *Reviews in particulate materials*, vol. 2, pp. 173-213, 1994.
- Janowski, K. R., Shum, M. S., and Bradley, S. A., "Heat transfer surface," *U.S. patent 4,129,181*, December 12, 1978.
- Jodrey, W. S., and Tory, E. M., "Computer simulation of close random packing of equal spheres," *Physical Review A (General Physics)*, vol. 32, no. 4, pp. 2347-2351, 1985.
- Kartsounes, G. T., "A study of the effect of surface treatment on pool boiling heat transfer in refrigerant 12," *ASHRAE Transactions*, vol. 81, no. 1, pp. 320-326, 1975.
- Kim, G. Y., Koc, M., and Ni, J., "Modeling of the size effects on the behavior of metals in the microscale deformation processes," *Transactions of the ASME, Journal of Manufacturing Science and Engineering*, vol. 129, pp. 470-476, 2007.
- Kim, K. T., Choi, S. W., and Park, H., "Densification behavior of ceramic powder under cold compaction," *Journal of Engineering Materials and Technology*, vol. 122, pp. 238-244, 2000.
- Kovalyo, S. A., and Soloviyov, S. L., "Heat transfer and critical heat fluxes in boiling on a porous surface," *Heat Transfer-Soviet Research*, vol. 22, no. 3, pp. 364-375, 1990.
- Kovar, D., Albert, A. D., Becker, M. M. and Keto, J. W., "Pressure-assisted sintering of nanocrystalline silver lines produced by laser ablation of microparticle aerosols," *Proceedings of the ASME Conference on Manufacturing Science and Engineering (MSEC 2007)*, No. MSEC2007-31170, 2007.

- Kunugi, T., Muko, K., and Shibahara, M., "Ultra-high heat transfer enhancement using nano-porous layer," *Superlattices and Microstructures*, vol. 35, no. 3-6, pp. 531-542, 2004.
- Lewis, R. W., and Schreffler, B. A., *The Finite Element Method in the Deformation and Consolidation of Porous Media*, Wiley, New York, 1987.
- Lian, J., and Shima, S., "Powder assembly simulation by particle dynamics method," *International Journal for Numerical Methods in Engineering*, vol. 37, no. 5, pp. 763 - 775, 1994.
- Liter, S. G., and Kaviany, M., "CHF enhancement by porous-layer coating," Proceedings of ASME 1998 IMECE, HTD vol. 361-1, pp. 165-173, 1998.
- Liter, S. G., and Kaviany, M., "Pool-boiling CHF enhancement by modulated porous-layer coating: theory and experiment," *International Journal of Heat and Mass Transfer*, vol. 44, no. 22, pp. 4287-4311, 2001.
- Liter, S. G., *Pool-boiling enhancement and liquid choking limits within and above a modulated porous-layer coating*, PhD Thesis, The University of Michigan, Ann Arbor, USA, 2000.
- Liu, P. S., and Liang, K. M., "Review Functional materials of porous metals made by P/M, electroplating and some other techniques," *Journal of Materials Sciences*, vol. 36, no. 21, pp. 5059-5072, 2001.
- Lu, G. Q., and Shi, X., "Computer simulation of isostatic powder compaction by random packing of monosized particles," *Journal of Materials Science Letters*, vol. 13, no. 23, pp. 1709-1711, 1994.
- Lu, S. M., and Chang, R. H., "Pool boiling from a surface with a porous layer," *AIChE Journal*, vol. 33, no. 11, pp. 1813-1828, 1987.
- Malyshenko, S. P., "Features of heat transfer with boiling on surfaces with porous coatings," *Thermal Engineering (English translation of Teploenergetika)*, vol. 38, no. 2, pp. 81-88, 1991.



- Martin, C. L., Bouvard, D., and Shima, S., "Study of particle rearrangement during powder compaction by the Discrete Element Method," *Journal of the Mechanics and Physics of Solids*, vol. 51, pp. 667-693, 2002.
- Matheson, A. J., "Computation of a random packing of hard spheres," *Journal of Physics C (Solid State Physics)*, vol. 7, no. 15, pp. 2569-2576, 1974.
- Milton, R. M., "Heat exchange system," *U.S. patent 3,384,154*, May 21, 1968.
- Munjiza, A., Owen, D. R. J., and Bicanic, N., "A combined finite-discrete element method in transient dynamics of fracturing solids," *Engineering Computations (Swansea, Wales)*, vol. 12, no. 2, pp. 145-174, 1995.
- Newell, K. J., Bampton, C. C., Morris, W. L., Sanders, B. P. and McMeeking, R. M., "Recent advances in consolidation process modeling of titanium matrix composites from powder-fiber monotapes," *Proceedings of the Symposium on Recent Advances in Titanium Metal Matrix Composites*, pp. 87-98, 1995.
- Nishikawa, K., Ito, T., and Tanaka, K., "Enhanced heat transfer by nucleate boiling on a sintered metal layer," *Heat Transfer Japanese Research*, vol. 8, no. 2, pp. 65-81, 1979.
- Nolan, T., and Kavanagh, P. E., "Computer simulation of random packing of hard spheres," *Powder Technology*, vol. 72, no. 2, pp. 149-155, 1992.
- O'Neill, P. S., Gottzmann, C. F., and Terbot, J. W., "Novel heat exchanger increases cascade cycle efficiency for natural gas liquefaction," *Advances in Cryogenic Engineering*, vol. 17, pp. 420-437, 1971.
- Olevsky, E. A., "Theory of sintering: from discrete to continuum," *Materials Science & Engineering R (Switzerland)*, vol. R23, no. 2, pp. 41-100, 1998.
- Parhami F., and McMeeking, R. M., "Computer simulation of solid state sintering of powders through discrete element method," *American Society of Mechanical Engineers, Applied Mechanics Division, v 194, Mechanics in Materials Processing and Manufacturing*, pp. 203-207, 1994.

- Parhami, F., and McMeeking, R. M., "A network model for initial stage sintering," *Mechanics of Materials*, vol. 27, pp. 111-124, 1998.
- Park, S. J., Han, H. N., Oh, K. H., and Lee, D. N., "Model for compaction of metal powders," *International Journal of Mechanical Science*, vol. 41, pp. 121-141, 1999.
- PM Modnet Computer Modelling Group, "Comparison of computer models representing powder compaction process," *Powder Metallurgy*, vol. 42, no. 4, pp. 301-311, 1999.
- Ransing, R. S., Gethin, D. T., Khoei, A. R., Mosbah, P., and Lewis, R. W., "Powder compaction modelling via the discrete and finite element method," *Materials & Design*, vol. 21, no. 4, pp. 263-269, 2000.
- Ransing, R. S., Lewis, R. W., and Gethin, D. T., "Using a deformable discrete-element technique to model the compaction behaviour of mixed ductile and brittle particulate systems," *Philosophical Transactions: Mathematical, Physical and Engineering Sciences*, vol. 362, no. 1882, pp. 1867 - 1884, 2004.
- Raut, J. S., Bhagat, R. B., and Fichthorn, K. A., "Sintering of aluminum nanoparticles: A molecular dynamics study," *Nanostructured Materials*, vol. 10, no. 5, pp. 837-851, 1998.
- Reay, D. A., "Compact heat exchangers, enhancement and heat pumps," *International Journal of Refrigeration*, vol. 25, no. 4, pp. 460-470, 2002.
- Roscoe, K. H., and Burland, J. B., "On the generalized stress-strain behaviour of 'wet' clay," *Engineering Plasticity*, pp. 535-609, 1968.
- Sanchez, L., Ouedraogo, E., Federzoni, L., and Stutz, P., "New viscoplastic model to simulate hot isostatic pressing," *Powder Metallurgy*, vol. 45, no. 4, pp. 329-334, 2002.
- Sanchez-Castillo, F. X., and Anwar, J., "Molecular dynamics simulations of granular compaction: The single granule case," *The Journal of Chemical Physics*, vol. 118, no. 10, pp. 4636-4648, 2003.

- Shima, S., and Oyane, M., "Plasticity theory for porous metals," *International Journal of Mechanical Science*, vol. 18, no. 6, pp. 285-291, 1976.
- Shima, S., Kotera, H., and Ujie, Y., "A study of constitutive behavior of powder assembly by particulate modeling," *Material Science Research International*, vol. 1, no. 3, pp. 163-168, 1995.
- Soloviyov, S. L., "Liquid evaporation heat transfer on a porous surface," *Heat Transfer - Soviet Research*, vol. 18, no. 3, pp. 58-64, 1986.
- Storåkers, B., Biwa, S., and Larsson, P. L., "Similarity analysis of inelastic contact," *International Journal of Solids and Structures*, vol. 34, pp. 3061-3083, 1997.
- Swinkels, F. B., and Ashby, M. F., "A second report on sintering diagrams," *Acta Metallurgica*, vol. 29, pp. 259-281, 1981.
- Thome, J. R., *Enhanced Boiling Heat Transfer*, Hemisphere, New York, 1990.
- Tomandl, G., and Varkoly, P., "Three-dimensional computer modeling of grain growth and pore shrinkage during sintering," *Materials Chemistry and Physics*, vol. 37, no. 1-3, pp. 12-16, 2001.
- Vyal, E. Y., and Laptev, A. M., "Strength of unsintered powder compacts with axial and radial loading," *Powder Metallurgy and Metal Ceramics*, vol. 41, pp. 249-252, 2002.
- Walter, A. J., and Trowell, A. R., "The thermal conductivity of porous copper," *Journal of Materials Science*, vol. 6, no. 7, pp. 1044-1046, 1971.
- Webb, R. L., "Nucleate boiling on porous coated surfaces," *Heat Transfer Engineering*, vol. 4, no. 3-4, pp. 71-82, 1983.
- Webb, R., *Principles of Enhanced Heat Transfer*, Wiley, New York, 1993.
- Yuncu, H., "Thermal contact conductance of nominally flat surfaces," *Heat Mass Transfer*, vol. 43, no. 1, pp. 1-5, 2006.

Zavaliangos, A., "Constitutive models for the simulation of P/M processes," *International Journal of Powder Metallurgy*, vol. 38, no. 2, pp. 27-39, 2002.

Zeng, P., Zajac, S., Clapp, P. C., and Rifkin, J. A., "Nanoparticle sintering simulations," *Materials Science and Engineering A*, vol. 252, no. 2, pp. 301-306, 1998.